New Horizon: Volume I

Multidisciplinary Approaches to Current Science Issues

Edited by

Dr. Sukla Nandi
&
Dr. Partha Roy Chowdhury

New Horizon

Volume I

Multidisciplinary Approaches to Current Science Issues

Dr. Sukla Nandi
Assistant Professor, Department of Chemistry
Chandrakona Vidyasagar Mahavidyalaya
Paschim Medinipur, West Bengal

&

Dr. Partha Roy Chowdhury
Assistant Professor, Department of Physics
Chandrakona Vidyasagar Mahavidyalaya
Paschim Medinipur, West Bengal

Price: Rs. 400.00

Preface

This book "**New Horizon: Multidisciplinary Approaches to Current Science Issues**" is a collection of various topics from the different disciplines in science. The book is an outcome of our efforts to bring together under one cover the contemporary topics of natural science including some environmental issues to cater the need of young researchers. Today our biggest challenge is to sustain our earth and to rescue the people of the earth who get fear for plenty of sustainability due to COVID-19 pandemic, malnutrition, population growth; finite resources, continuous climate change and we all want to survive by using scientific and technological progress. As nature is dynamic and refreshes herself every time, the natural science also advances and renews itself with new inventions. This book has made tiny effort to make correlation between the recent trends in multi disciplines of science research and the present scenario.

The contributors have tried their level best to highlight the current trends in research in the multi disciplines in science. In this content Dr. Aparajeo Chattopadhyay and Dr. Partha Biswas have discussed about the air pollution which is one of the major societal challenges for mankind and the article highlights that how the knowledge of chemistry could be utilized to mitigate this environmental challenge. Dr. Dibyendu K. Sasmal and his group explain the role of calcium ion on conformational change and activation of T-cell receptor. Microwave has proved to be a convenient tool in the hands of chemists for organic synthetic processes in the recent past. Keeping this point in view, Dr. Manju Kumari has undertaken a comparative study of the oxidation products of succinic acid in conventional and microwave heating conditions. Impedance spectroscopy genetic programming has been demonstrated on electrochemical systems such as SOFC cathode half cells and anode half cells, SOFC-SOEC full cells, supercapacitors and pseudo-supercapacitors. Dr. Nimai Bar continue these efforts and expand it to analyze the ion-conduction of the PEO-PU/PEGDME: $LiClO_4$ solid semi-IPN matrix. Dr. Partha Roy Chowdhury has described neutron stars as ideal astrophysical laboratories for testing theories of dense matter physics and shown connections among nuclear physics, particle physics and astrophysics. Dr. Mukesh Kumar Pradhan explores the Superheavy Island which is a long standing issue in nuclear science. Discovery of new superheavy elements extends the periodic table step by step beyond Uranium. Dr. Sukla Nandi has written a review article about the various methods for the synthesis pyrrole derivatives using copper catalysts. Role of palladium catalyst for the synthesis of fused pyran ring has discussed by Dr. Rathin Jana. Dr. Aloke Kumar Ghosh has discussed on

About the Authors

Dr. Sukla Nandi is currently working as Assistant Professor of Chemistry at Chandrakona Vidyasagar Mahavidyalaya, Chandrakona Town, Paschim Medinipur, West Bengal. She has over 7 years of teaching experience at the undergraduate level. She passed B.Sc. (Hons. in Chemistry) in 2005 from Midnapore College, Vidyasagar University, West Bengal and M.Sc. (Chemistry) in 2007 from Vidyasagar University, West Bengal. She got PhD degree in Chemistry from Indian Institute of Technology Kharagpur in the year 2012. Her research interest includes synthesis of heterocyclic compounds by palladium and copper catalysed reactions. Dr. Nandi has received UGC-D. S. Kothari postdoctoral fellowship and she is a life member of Chirantan Rasayan Sanstha (CRS).

Dr. Partha Roy Chowdhury has been associated with the teaching faculty of Physics at Chandrakona Vidyasagar Mahavidyalaya, Paschim Medinipur, West Bengal since 2015. He has more than 11 years of teaching experience at the undergraduate level. He completed his M.Sc. in Physics from the University of Calcutta in 2001. He carried out research works in Nuclear Reaction & Astrophysics at Saha Instititute of Nuclear Physics, Kolkata and obtained Ph.D. degree from Jadavpur University in 2009. Dr. Roy Chowdhury has been the recipient of UGC-D. S. Kothari Postdoctoral award in 2009 and he has so far published 27 research papers in different reputed international journals.

Advisory Board Members

Contributor's Profile

Dr. Aparajeo Chattopadhyay, **Research Scientist,** Cooperative Institute for Research in Environmental Sciences (CIRES), University of Colorado, Boulder, CO, USA 80309

Dr. Dibyendu Kumar Sasmal, Assistant Professor, Department of Chemistry, Indian Institute of Technology Jodhpur, Rajasthan, India

Dr. Partha Biswas, Assistant Professor, Department of Chemistry, Dhruba Chand Halder College, Dakshin Barasat, West Bengal, India

Dr. Manju Kumari, Assistant Professor, Department of Chemistry, Maharaja College, Ara, Bihar, India

Dr. Nimai Bar, Assistant Professor, Department of Chemistry, Raja N. L. K. Women's College (Autonomous), Midnapore, Paschim Medinipur, West Bengal, India

Dr. Partha Roy Chowdhury, Assistant Professor (H.O.D), Department of Physics, Chandrakona Vidyasagar Mahavidyalaya, Chandrakona Town, Paschim Medinipur, West Bengal, India

Dr. Mukesh Kumar Pradhan, Assistant Professor, Department of Physics, Belda College, Paschim Medinipur, West Bengal, India

Dr. Sukla Nandi, Assistant Professor (H.O.D), Department of Chemistry, Chandrakona Vidyasagar Mahavidyalaya, Chandrakona Town, Paschim Medinipur, West Bengal, India

Dr. Rathin Jana, Assistant Professor, Department of Chemistry, Shahid Matangini Hazra Govt. General Degree College for Women, Chakshrikrishnapur, Kulberia, Purba Medinipur, West Bengal, India.

Dr. Aloke Kumar Ghosh, Assistant Professor, Department of Chemistry, Prabhat Kumar College, Contai, Purba Medinipur, West Bengal, India

Dr. Moumita Gangopadhyay, Assistant Professor, Department of Chemistry, Ghatal Rabindra Satabarsiki Mahavidyalaya, Ghatal, Paschim Medinipur, West Bengal, India

Dr. Suman Samai, Assistant Professor, Department of Chemistry, Prabhat Kumar College, Contai, Purba Medinipur, West Bengal, India

Dr. Arpita Biswas, Assistant Professor, Department of Chemistry, Shibpur Dinobundhoo Institution (College), Howrah, West Bengal, India

Semanti Das, Assistant Professor, Department of Geography, Chandrakona Vidyasagar Mahavidyalaya, Paschim Medinipur, West Bengal, India

Dr. Mitali Dewan, Assistant Professor, Department of Chemistry, Shahid Matangini Hazra Govt. General Degree College for Women, Chakshrikrishnapur, Kulberia, Purba Medinipur, West Bengal, India.

Anindya Mondal, Assistant Professor, Department of Computer Science, Chandrakona Vidyasagar Mahavidyalaya, Paschim Medinipur, West Bengal, India

Indadul Khan, Assistant Professor, Department of Computer Science, Chandrakona Vidyasagar Mahavidyalaya, Paschim Medinipur, West Bengal, India

= Contents =

CHAPTER 1

Air Pollution: What is the Role of Chemistry?

✍ Dr. *Aparajeo Chattopadhyay[a]*, and Dr. Partha Biswas[b]*

[a]Cooperative Institute for Research in Environmental Sciences (CIRES), University of Colorado, Boulder, CO, USA 80309,

[b]Department of Chemistry, Dhruba Chand Halder College, Dakshin Barasat, West Bengal-743372, India.

*Corresponding author, E-mail: c.aparajeo@gmail.com

Introduction:

Air pollution is one of the major societal challenges for mankind not only in the present time but also a matter of great concern in the upcoming decades. A relevant and recent example that received a great deal of national and international attention is the extremely poor air quality in Delhi, India, particularly during winter times. According to World Health Organization (WHO)[1], air pollution is among the top three global risk factors for disease and premature death. It has been estimated that more than six million deaths occur annually due to the combined effect of household and ambient air pollution.[1,2] Emission, chemistry, and meteorological conditions are the three prime factors that influence air pollution. This short review aims to explore the role of chemistry in air pollution. Tropospheric ozone (O_3), and particulate matter (PM) are the two most important chemical entities that cause poor air quality globally.[2,3] Other chemicals that contribute to air pollution include carbon monoxide (CO), nitrogen dioxide (NO_2), sulfur dioxide (SO_2), and ammonia (NH_3) to name but a few. In this review, the chemistry behind the formation of tropospheric ozone (O_3) and secondary organic aerosol (SOA), a major constituent of the atmospheric particulate matter (PM) is thoroughly discussed. Atmospheric chemistry is the branch of science that conducts regular research on this topic. A glimpse of the current research activities on air quality is presented in this article. How the

knowledge of chemistry could be utilized to mitigate this environmental challenge is also highlighted.

1. Atmospheric Chemistry of Air Pollution: Earth's atmosphere can be considered a complex chemical system that is oxidizing in nature. Although the chemical composition of the atmosphere is dominated by nitrogen (~ 78% by volume) which is an inert gas, and oxygen (~ 21% by volume), it is the trace gases i.e. the atmospheric constituents with less than 1% abundance combined that cause major atmospheric events such as air pollution, climate change, and stratospheric ozone layer depletion. The most important trace gases from the perspective of atmospheric chemistry include water (H_2O) vapor, ozone (O_3), carbon dioxide (CO_2), nitrogen oxides, ammonia (NH_3), sulfur compounds, halogenated compounds, volatile organic compounds (VOCs), etc. VOCs are key chemical compounds that are emitted into the atmosphere by biogenic as well as anthropogenic i.e. man-made sources. The chemical processing of VOCs in the atmosphere results in the formation of tropospheric ozone (O_3), and secondary organic aerosol (SOA) which are the major atmospheric pollutants. Most often, sunlight plays a major role in this chemistry. The ultraviolet radiation of sunlight has sufficient energy to dissociate many chemicals in the atmosphere including VOCs. The following subsections will review how the oxidation chemistry of VOCs forms major atmospheric pollutants.

1.1 Tropospheric Ozone: Ozone (O_3) is a chemical compound containing three oxygen atoms present in the atmosphere as a trace gas. The atmospheric budget of ozone (O_3) is distributed among the troposphere, the lowermost layer of the atmosphere, and the stratosphere which extends ~ 15-50 km from the surface.[4,5] There are distinct differences between the ozone molecules present in these two atmospheric layers in terms of their origin, abundance, and effectivity. The stratosphere contains ~90% of the total atmospheric ozone forming ozone layer. The ozone layer absorbs a significant portion of the ultraviolet-B and ultraviolet-C radiation (~ 200-300 nm) of the sunlight and prevents this radiation to reach the surface. Thus, stratospheric ozone protects us from the harmful effect of ultraviolet radiation and therefore it is also called 'good ozone'. Stratospheric ozone

molecules are formed by a sequence of chemical reactions known as the Chapman mechanism (reactions R1 to R4).[4,5]

$O_2 + h\nu = O + O$ ($\lambda < 240$ nm) (R1)
$O + O_2 + M = O_3 + M$ (R2)
$O_3 + h\nu = O_2 + O$ ($\lambda < 320$ nm) (R3)
$O + O_3 = O_2 + O_2$ (R4)
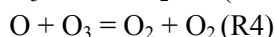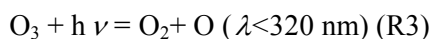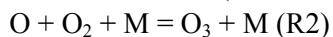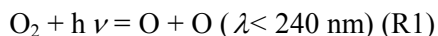
The ultraviolet radiation from sunlight available in the upper atmosphere has sufficient energy to break oxygen molecules (O_2) and form oxygen atoms (O) in reaction R1. The oxygen atom (O) combines with an oxygen molecule in presence of a third body M (e.g. N_2) forming ozone (O_3) in reaction R2. It should be noted that there are degradation channels for ozone (O_3) by photolysis (reaction R3) and reaction with an oxygen atom (O) (reaction R4). There remains a balance between the formation and degradation channels and a steady-state concentration for stratospheric ozone (O_3) is maintained.

The troposphere contains the rest ~10% of ozone and the formation mechanism is completely different which involves VOC oxidation in presence of nitrogen oxides. The ozone in the troposphere is a pollutant and therefore tropospheric ozone (O_3) is known as 'bad ozone'. High levels of ozone in the troposphere severely affect people with various lung diseases and sensitive populations such as children and older adults. The formation mechanism of tropospheric ozone is shown in Figure-1 using methane (CH_4) as a representative VOC. Methane (CH_4), a dominant greenhouse gas and the most abundant VOC in the atmosphere, is emitted mainly from anthropogenic activities viz. production and transport of oil, natural gas, coal, agricultural practices, and solid waste landfills.
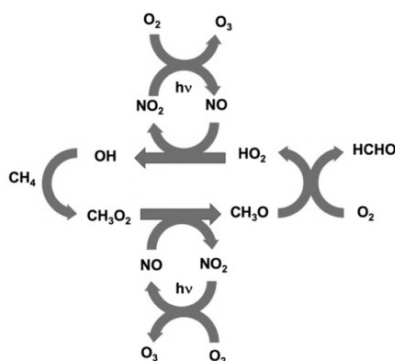
Figure-1: Formation of tropospheric ozone (O_3) by methane (CH_4) oxidation.

$CH_4 + OH = CH_3 + H_2O$ (R5)
$CH_3 + O_2 + M = CH_3O_2 + M$ (R6)
$CH_3O_2 + NO = CH_3O + NO_2$ (R7)
$CH_3O + O_2 = HCHO + HO_2$ (R8)
$HO_2 + NO = OH + NO_2$ (R9)
$NO_2 + h\nu = NO + O$ (R10)
$O + O_2 + M = O_3 + M$ (R11)
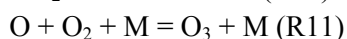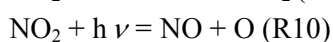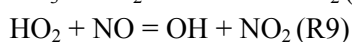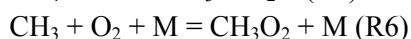
In the atmosphere, methane is predominantly removed by hydroxyl (OH) radicals involving H-atom abstraction reaction forming methyl (CH_3) radical and water vapor (reaction R5). Hydroxyl (OH) radical, also known as the atmospheric detergent, removes most of the VOCs from the atmosphere by chemical reaction. Methyl radical (CH_3) formed by reaction R5 further reacts with molecular oxygen (O_2) present in the atmosphere in excess forming methyl peroxy (CH_3O_2) radical (reaction R6). In a pristine environment, the primary fate of the peroxy radicals is the self-reaction or reaction with hydroperoxide (HO_2) radical forming products such as alcohol and aldehyde. However, in a polluted urban environment where the abundance of NO_x ($NO+NO_2$) species is significantly high, the fate of peroxy radical is the reaction with nitric oxide (NO) forming nitrogen dioxide (NO_2) and methoxy (CH_3O) radical (reaction R7). Nitrogen dioxide (NO_2) undergoes photo dissociation in presence of the ultraviolet radiation from sunlight forming oxygen atom (O) (reaction R10) which further reacts with molecular oxygen

to form tropospheric ozone (O_3) (reaction R11). The fate of methoxy (CH_3O) radical is the further reaction with molecular oxygen (O_2) forming formaldehyde (HCHO) and hydroperoxyl radical (HO_2) (reaction R8). Hydroperoxyl (HO_2) radical reacts with nitric oxide (NO) forming ozone (O_3) and regenerating OH radical (Figure-1). Although hydroxyl (OH) radical is the predominant oxidant for the degradation of methane (CH_4) and most of the VOCs, there are other oxidants as well e.g., chlorine atom (Cl), and nitrate (NO_3) radical. Reaction with chlorine (Cl) atom is relevant in the marine environment due to its higher abundance whereas reaction with nitrate radical (NO_3) plays a key role in night-time oxidation of VOCs. It should be noted that the reaction rate and mechanism for oxidant + VOC reaction are dependent on the molecular structure of a particular VOC and the energetics of available chemical channels. As seen in the case of methane (CH_4), the reaction with OH radical is an H-atom abstraction reaction, whereas the reaction with many olefins (Figure-2) is predominantly an addition reaction. There are many VOCs such as carbonyls that absorb strongly in the actinic region of solar ultraviolet radiation and therefore, direct photolysis involving absorption of ultraviolet (UV) radiation from sunlight is a major degradation channel for them. An example of this is the photo dissociation of acetaldehyde (CH_3CHO) (reaction R12a and R12b). The free radicals formed by the photo dissociation further react with molecular oxygen (O_2) to form peroxy radicals which produce ozone (O_3) by the mechanism previously discussed for methane.
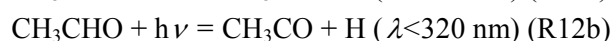
$CH_3CHO + h\nu = CH_3 + HCO$ (λ<337 nm) (R12a)
$CH_3CHO + h\nu = CH_3CO + H$ (λ<320 nm) (R12b)
The yield of ozone (O_3) depends on VOC abundance and the rate of these chemical reactions.

1.2 Particulate Matter (PM): Particulate matter or PM is another dominant substance that causes air pollution. In atmospheric chemistry, the terms 'particles' or 'particulate matter' and 'aerosols' are often used in close conjunction and therefore clarification is required. Aerosols are defined as solid or liquid particles in a gas (air in the case of the atmosphere). Thus from the definition, aerosol includes both the particles and the gas in which they are suspended.[4,5] Particles scatter light efficiently making the atmosphere hazy with reduced visibility which is the feature of many urban

air pollutions such as Delhi air pollution. The same light scattering property is responsible for its major role in climate. The physical and chemical properties of aerosols determine the health effects they cause. The atmospheric particles are often classified based on their sizes and the particle diameters typically vary between ~0.002 to ~100 μm.[5] PM_{10} and $PM_{2.5}$ are inhalable particles with diameters less than 10 and 2.5 micrometers respectively. The most important properties of the atmospheric particles are size, mass, chemical composition, and aerodynamic and optical properties. However, in this article, the discussion is limited to aerosol chemical composition and the chemical reactions responsible for their formation.

A significant portion (~50%) of the tropospheric aerosol mass contains organic matter while the other constituents include sulfate, nitrate, elementary carbon, etc.[6] A smaller part (~20%) of the organic aerosol (OA) is directly emitted which is known as primary organic aerosol (POA) while the major portion of OA is formed involving chemical reactions in the atmosphere and this is known as secondary organic aerosol (SOA). The reactions responsible for SOA formation involve VOC oxidation in the presence or absence of NO_x. The gas-phase oxidation of VOCs forms highly oxidized organic compounds with increased polarity and decreased vapor pressure. As a result, these semi-volatile or non-volatile products partition to the condensed phase of the pre-existing OA mass and initiate aerosol growth. An example is shown here for isoprene oxidation (Figure-2).[7]
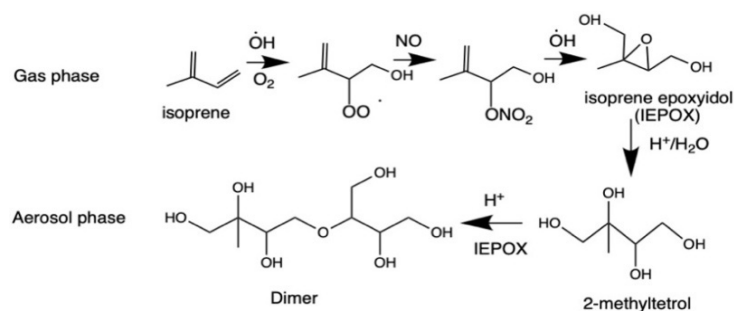
Figure-2: Selected reactions of isoprene oxidation leading to SOA formation.

Isoprene is the most abundant non-methane VOC whose origin is mostly biogenic. Upon oxidation by OH radicals in presence of oxygen (O_2), and nitric oxide (NO), it forms isoprene epoxyidol which due to its lower

vapor pressure partition to condense phase or pre-existing aerosol phase and undergoes further oxidation resulting in aerosol growth. It should be noted that only some selected pathways of isoprene oxidation are shown in Figure-2. Multiple other pathways result in the production of several oxidized species that help in SOA formation. There are other mechanisms of SOA formation such as reactions within the aqueous phase in the cloud, and in aerosol particles or reactions of gases on the surface of pre-existing particles but the central to most of these processes is the oxidation chemistry.[5]

2. Air Quality Research: Air quality is a major research area in atmospheric chemistry, a multidisciplinary research field. Three essential components of atmospheric chemistry research are field measurements, laboratory studies, and atmospheric modeling studies.[7] Like most other atmospheric chemistry problems, air quality research is also carried out by a collaboration of these three interrelated sub-fields. A brief description of these research areas is presented below.

2.1 Field Measurements: Field measurement is an important segment of air quality research. Major sources of air pollution include natural sources such as biomass burning, vegetation, volcanos, emission from oil and natural gas production, and anthropogenic sources such as vehicular emission, industrial emission, use of volatile consumer products, and agricultural emission to name but a few. Field measurements play a key role in measuring concentrations of chemicals that contribute to air pollution. Moreover, it is instrumental in capturing the dynamics of an atmospheric chemical event. An example of this is a recent aircraft field campaign known as FIREX-AQ 2019, in which the scientists from NOAA (National Oceanic and Atmospheric Administration, USA), NASA (National Aeronautics and Space Administration, USA) in collaboration with several US universities measured several primary and secondary pollutants during actual biomass burning events in the Western United States.[8] In another such campaign the scientists from IISER, Mohali, India were involved in ground-based measurements of pollutants originating from agricultural sites in North-West India.[9] The measurements in these field campaigns include O_3, PM, SO_2, NO_x, VOCs, total OH reactivity, etc. Several high-precision analytical

instruments are being used for this purpose. Scientific instruments that are used regularly for measuring key chemical species from an air quality perspective are listed below in Table-1. Apart from the ground-based and aircraft campaigns, several key chemicals are being measured from satellite data as well.

Table-1: Some common analytical methods being used in field measurements of atmospheric chemical species.

Species	Measurement techniques
O_3	Chemiluminescence.
NO_x	Chemiluminescence, Cavity-enhanced spectroscopy.
VOCs	Proton-transfer-reaction mass spectrometry (PTR-MS), Chemical-ionization mass spectrometry (CIMS), Gas-chromatography mass spectrometry (GC-MS).
CO, CO_2	Laser absorption spectroscopy.
SO_2	Laser-induced fluorescence.
Aerosol	Aerosol mass spectrometry, particle counters, cavity ring down extinction spectrometer.

2.2 Laboratory Studies: Laboratory studies provide the fundamental chemical knowledge of the chemistry of the pollutants in the atmosphere and form a bridge between field measurements and modeling.[7] The dataset provided by laboratory studies not only supplies necessary inputs being used in modeling to explain observations in fields but also forms the basis of environmental policy making. Fundamental laboratory studies include kinetics of oxidation reactions, photochemistry, product studies, aerosol

property measurements, etc. A brief description of these measurements is presented in this section. As mentioned, VOCs are removed from the atmosphere by gas-phase reactions with oxidants such as OH radicals, Cl atom, NO_3 radical as well as by photo dissociation. An important parameter that is being used in atmospheric chemistry is the atmospheric lifetime (τ) of a VOC which is expressed as:

$$\frac{1}{\tau} = \frac{1}{\tau_{OH}} + \frac{1}{\tau_{Cl}} + \frac{1}{\tau_{NO_3}} + \frac{1}{\tau_{photo}} \tag{i}$$

where, $\tau_{OH} = \frac{1}{[OH]k_{OH}}$, $\tau_{Cl} = \frac{1}{[Cl]k_{Cl}}$, $\tau_{NO_3} = \frac{1}{[NO_3]k_{NO_3}}$, $\tau_{photo} = \frac{1}{J}$, and

k_{OH}, k_{Cl}, k_{NO_3} are the bi-molecular rate coefficients for the reaction with OH,

Cl, and NO_3 respectively, while J is the first order photolysis rate coefficient. [OH], [Cl], [NO_3] are the atmospheric concentrations of OH, Cl, and NO_3 respectively. Sometimes, physical processes such as dry and wet depositions also take part in the removal of a VOC.

2.2.1 Kinetics: Gas-phase kinetics measurements are performed either by absolute methods or by relative methods. In absolute kinetics methods, the measurements are typically performed in a flow reactor where the oxidants i.e. OH, Cl, NO_3 radicals are being produced by methods such as laser photolysis, radiolysis, and microwave discharge of a suitable precursor. For example, OH radicals are regularly produced by pulsed UV laser (248 nm output of a KrF excimer laser or 351 output of a XeF excimer laser) photolysis of hydrogen peroxide (H_2O_2) or nitrous acid (HONO).[10] Spectroscopic methods are regularly used for detecting the short-lived radicals and monitoring their temporal evolution. OH radical is probed by laser-induced fluorescence or resonance fluorescence, and Cl atom is probed by resonance fluorescence, while NO_3 radical is monitored by cavity ring down spectroscopy (CRDS) methods. In most cases, VOC + oxidant reaction kinetics is studied under pseudo-first-order reaction condition i.e., [VOC]>>[oxidant]. The VOC concentration, which remains essentially constant during the course of a measurement is measured either by spectroscopic methods such as FTIR (Fourier Transform Infrared Spectroscopy), UV absorption spectroscopy or is determined from flow measurements. The pseudo-first-order rate coefficient (k') is determined by

fitting the time trace of the short-lived radical using a single-exponential function. The bimolecular rate coefficient (k) is determined from the pseudo-first-order rate coefficient (k') and VOC concentration using equation (ii).[10]

$$k' = k \, [\text{VOC}] \tag{ii}$$

Measuring the kinetics of a radical-radical reaction is more challenging because it requires monitoring the temporal profiles for both the short-lived radicals simultaneously. In the relative rate method, the rate coefficient of a VOC reaction is measured relative to another compound for which the rate coefficient is known.[11] An example of this is provided here for measuring a VOC+OH reaction. The VOC for which the rate coefficient is to be determined is mixed with a reference compound and OH radical precursor, e.g. HONO in a static reactor. Then the reaction mixture is subjected to UV radiation (UV lamp or LASER) for the generation of OH radicals by photo dissociation of HONO. The generated OH radicals react with VOC and the reference compound at a different rate. As the reactions proceed the concentrations of the selected VOC and reference compounds are measured via spectroscopic methods such as FTIR or GC-MS. The rate coefficient is determined from the following equation.

$$\ln \left(\frac{[\text{VOC}]_0}{[\text{VOC}]_t} \right) = \frac{k_{\text{VOC}}}{k_{\text{reference}}} \ln \left(\frac{[\text{reference}]_0}{[\text{reference}]_t} \right) \tag{iii}$$

where, $[\text{VOC}]_0$ and $[\text{VOC}]_t$ are the concentrations of the VOC at time 0 and time t respectively, whereas $[\text{reference}]_0$ and $[\text{reference}]_t$ are the concentrations of the reference compounds at time 0 and time t respectively. k_{VOC} and $k_{\text{reference}}$ are the rate coefficients for the reaction of OH with VOC and the reference compound respectively. Since $k_{\text{reference}}$ is known, from the slope of a plot between $\ln \left(\frac{[\text{VOC}]_0}{[\text{VOC}]_t} \right)$ and $\ln \left(\frac{[\text{reference}]_0}{[\text{reference}]_t} \right)$, k_{VOC} is determined.

2.2.2 Photochemistry: Photochemistry measurements include measuring UV absorption spectra and photolysis quantum yields. The atmospheric first-order photolysis rate coefficient (J) is expressed as:

$$J = \int \Psi(\lambda, z, \chi) \, \Phi(\lambda, T, P) \, \sigma(\lambda, T) \, d\lambda \tag{iv}$$

where, $\Psi(\lambda, z, \chi)$ is the solar actinic flux (photon cm^{-2} s^{-1} nm^{-1}) and is a function of wavelength λ, altitude z, and solar zenith angle χ. $\Phi(\lambda, T, P)$ is the dissociation quantum yield (molecule $photon^{-1}$) at pressure P, wavelength λ and temperature T. $\sigma(\lambda, T)$ is the absorption cross-section (cm^2 $molecule^{-1}$) at wavelength λ and temperature T. σ or the UV absorption cross-section is measured using regular absorption spectroscopy method employing D_2 or Hg lamps as the UV light source and detectors such as a charge-coupled detector (CCD) or diode array. Quantum yield is typically measured relative to a reference compound of known quantum yield i.e., by actinometry.

2.2.3 Product Studies: Product studies are performed similarly to a relative rate experiment but without the reference compound being present. Often, smog chambers are used for this purpose. Smog chambers are large volume atmospheric chambers that have the advantage of minimum wall loss. Smog chambers are also useful in measuring SOA yield from an oxidation reaction under various experimental conditions such as with or without NO_x, seed chemicals, etc. The physical parameters of aerosols such as size, and chemical composition as well as their evolution with time are measured in a chamber or in a single droplet that is being trapped optically or electrodynamically. The product studies, sometimes in conjunction with the electronic structure calculations and modeling help in understanding the reaction mechanism of a VOC oxidation reaction.

2.3 Modeling: Atmospheric modeling is a useful tool in air quality research that plays a key role in rationalizing the observation from field studies. It is also extremely beneficial for its predictive capability of a near-future atmospheric event or when field data is not available. As mentioned previously, VOCs are primarily emitted into the atmosphere by natural and anthropogenic activities, and sometimes they are being formed in the atmosphere by chemical reactions. The atmospheric fate of VOCs in the atmosphere is chemical loss or deposition. The concentration of a VOC in a geographical region also depends on meteorological conditions such as wind speed and direction as it can be carried from one region to the other by atmospheric transport. Atmospheric modeling takes into account all these factors and run a mathematical model to predict concentrations of the VOCs regionally or globally. Two kinds of models i.e. box model and puff model

are being used regularly. A schematic of a one-box model for a VOC is shown in Figure-3.[4]
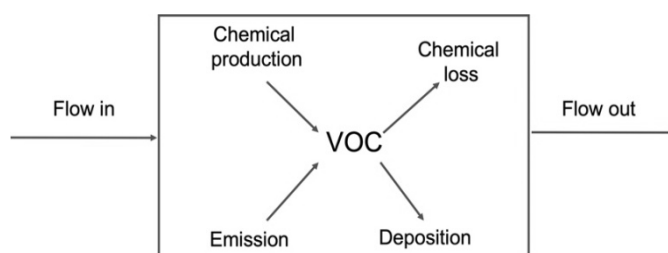
Figure-3: One-box atmospheric model for VOC.[4]

The models use various emission inventories, and laboratory data for the chemical parameters, whereas meteorological parameters along with transport models are considered to tackle the transport part. Air quality forecast models focus on predicting the concentration of ozone, PM, and other pollutants.

3. Mitigation Strategies: The knowledge received from the study of the chemistry of air pollutants are critical in making proper policymaking to mitigate air pollution. As previously seen in this article the chemistry of VOCs and NO_x are critical in making atmospheric pollutants, reduction in their emissions is the straightforward solution. A major source of these chemicals is anthropogenic such as vehicular emissions and industrial emissions which need to be regulated for this purpose. Concentrations of the pollutant chemicals are regularly reported in Air Quality Index (AQI) data by environmental agencies such as Central Pollution Control Board, India, and US Environmental Protection Agency (US EPA). Air quality forecast modeling is important in predicting local and regional air quality. Like a weather forecast, an air quality forecast could warn people of a bad air quality condition in advance so that the sensitive population groups could take proper measures on time. As discussed in the previous sections, the knowledge of emission and data on chemical parameters such as reaction rate coefficients, photochemical lifetime, and meteorological conditions are essential for a successful forecast modeling.

References:

1. World Health Organization, Seventy-first World Health Assembly, A71/10 Add.1, 20 April 2018.
2. Brauer et al. Environ. Sci. Technol.; 2016, 50, 79-88.
3. Schneidemesser et al. Chem. Rev.; 2015,115, 3856−389.
4. D. J. Jacob, Introduction to Atmospheric Chemistry; Princeton University Press, 1999, (ISBN 0-691-00185-5)
5. Barbara Finlayson-Pitts, James Pitts, Jr., Chemistry of the Upper and Lower Atmosphere: Theory, Experiments, and Applications; Academic Press, 2000. 1st edition. (ISBN 9780122570605)
6. De Gouw et al. Environ. Sci. Technol.; 2009, 43, 7614–7618.
7. Burkholder et al. Environ. Sci. Technol.; 2017, 51, 2519-2528.
8. https://csl.noaa.gov/projects/firex-aq/about/ (accessed: 23rd April 2022).
9. Chandra et al. Environ. Intl.; 2016, 88, 187-197.
10. Chattopadhyay et al. Int. J. Chem. Kinet.; 2020, 52, 623-631.
11. Chattopadhyay et al. Phys. Chem. Chem. Phys.; 2021, 23, 4901-4911.

CHAPTER

2

Role of Ca^{2+} Ion on Conformational Change   and Activation of T-Cell Receptor

✎ *Pratibha Agarwala, Debasish Rout and Dibyendu K. Sasmal**

Department of Chemistry, Indian Institute of Technology Jodhpur, Jodhpur-342037, India.

*Corresponding author, E-mail: sasmal@iitj.ac.in

Introduction:

The non-covalent weak interaction between TCR and pMHC with a short half-life time (t$_{1/2}$in ms) on the surface of antigen-presenting cell help differentiate between foreign vs self-antigen, which is a fundamental molecular interaction for immune response.[1] The interaction causes a extracellular conformational changes of TCR as well as downstream signalling cascade inside T-cell.[1] It is previously reported that even a single molecule TCR-pMHC interaction for some time can trigger a full-scale T-cell activation and following reactions.[2] The major unanswered question is, what force or mechanism is responsible for T-cell triggering? The architecture of the T-cell receptor is complex, as it is an extracellular protein domain of two heterodimer TCR$\alpha\beta$ associated with signal transduction subunit pair CD3εγ, CD3εδ and intracellular CD3ζζ.[3] Several hypotheses for TCR-ligand binding events have been proposed, mainly involving conformational change between TCR-pMHC interfaces and serial engagement.[4] In the cytoplasmic domain of the TCR-CD3 complex, two subunits chain of immune receptor tyrosine-based activation motifs (ITAMs) remain bound to lipid membrane at resting state.[4] TCRαβ complex binds to pMHC present on APC, leading to conformational changes in the CD3 complex.[5] The conformational changes of ITAM motif is essential for the TCR signalling so that tyrosine phosphorylation can proceed by the Src family tyrosine kinases Lck.[4]

In the adaptive immune system, Ca^{2+} ion is a versatile secondary messenger that controls lymphocytes' activation, including T-cell triggering based immune response. The store-operated calcium entry (SOCE) is the main pathway for increasing intracellular Ca^{2+} concentration across the plasma membrane stimulated through Ca^{2+} release-activated calcium (CRAC) channels.[6] T-cell engagement with peptide conjugated major histocompatibility complex (pMHC) on the antigen-presenting cell (APC) evolved rapid cytoskeletal rearrangements and release of Ca^{2+} from the endoplasmic reticulum. T-cells with impaired Ca^{2+} intake lacked the TCR mediated Ca^{2+} signalling causing IL-2 production and impaired proliferation of T-cells and immune response.[6] Following are example on understanding the role of Ca^{2+}ion for activation and conformational change of TCR.

Ca^{2+} Signalling in T-Cell:

For the Ca^{2+} signal to act as the on/off switch of a signalling molecule, the level of the Ca^{2+} in the cellular organelles must fluctuate with time.[6] T-cells has different types of channels for Ca^{2+} transport across the plasma membrane e.g., store operated Ca^{2+} entry channel (SOCE) and Ca^{2+} release activated Ca^{2+} channel (CRAC). Passage of Ca^{2+} across the channel is regulated by the gradient of concentration of Ca^{2+} between either side of the membrane by membrane potential.[6] T-cells have a resting cytoplasmic concentration of Ca^{2+} of 50-100nM compared with the outside concentration of Ca^{2+}, 1-2mM. T-cell plasma membrane has a resting membrane potential of -60mV to -50mV, supporting Ca^{2+} intake.[6] Other ion channels of sodium, chloride, and potassium ions maintain the membrane potential, indirectly controlling Ca^{2+} transport. Ca^{2+} transport across the membrane is controlled by receptor-activated Ca^{2+} channels on the T-cells, which operate at the membrane potential. Voltage-activated Ca^{2+} channels are generally present on the neurons, connected with T-cell functioning. Endoplasmic reticular (ER) is responsible for increasing the Ca^{2+} concentration inside the cytoplasm as ER has a Ca^{2+} concentration of 300μM to 1mM.[7] ER has Ca^{2+} channels for the release of Ca^{2+}, such as RYRs and $InsP_3R$.[6] To understand the function of the Ca^{2+} signal at the intracellular level, short term and long term roles are discussed below.[7]

Short-term and Long-term Roles of Ca^{2+} Signal:

The Ca^{2+}-dependent processes regulate the lymphocyte's motility and synapse formation.[8] Various studies have shown that a rise in the concentration of Ca^{2+} inside the T-cells causes a reduction in mobility while blocking the Ca^{2+} increase has reversed this process.[8] In the mature T-cells, it has been observed that an increase in Ca^{2+} is essential and appropriate to send a halt signal to the T-cells.[9] This signal appears to sustain the communication between APC and T-cells. Synapse is formed when the concentration of intracellular Ca^{2+} rises in cytotoxic T-lymphocytes (CTLs), necessary for the granule's exocytosis and killing the target cells.[8] An increase in Ca^{2+} for several hours causes a rise in gene expression alteration, cytotoxicity mediated by CTL and causes the release of lytic enzymes, which is the initial symbol of cell death in the target cell.[9]

Ca^{2+} also has a role in transcriptional regulation of the T-cell activation by affecting the gene expression pattern like cytokine expression.[8] It can control the immune response, differentiation of naïve T-cells, and growth of immature T-cells by acting on the expression pattern of genes. It should be noted that all the above-discussed programs need Ca^{2+} signals initially, do not require a rise in Ca^{2+} levels for the long term, but are communicated by changes in the expression pattern of genes and epigenetic modifications in Ca^{2+}-dependent.[7] Ca^{2+}-dependent expression of gene needs sustained rise in Ca^{2+} for several hours. The duration and strength of the Ca^{2+} signal originating from CRAC channels, and TCR regulate gene expression patterns in a Ca^{2+}-dependent manner. The transcription factors (CREB, NFAT, and MEF2) that regulate the gene require appropriate Ca^{2+} levels.[10]

Catch-Bond Triggers Ca^{2+} Signalling in T-Cell:

TCR-pMHC bond kinetics was primarily measured in force-free conditions.[11] TCR-pMHC bond formation occurs in the vicinity of antigen-presenting cell (APC), and the generation of immunological synapse was subjected to forces in the piconewton (pN) range.[12] The behaviour of slip-bond was first defined by Zhurkov and Bell that a force acting on a protein complex usually decreases its lifetime, and the mean length of the complex remains constant before bond rupture.[12] However, many biological systems

exhibit counterintuitive phenomena, so-called catch-bonds, where the bond becomes more substantial and lifetime increases with low force values.[13] The direct evidence of the catch-bond was observed by biomembrane force probe (BFP), atomic force microscopy (AFM), and the optical tweezer experiments.[14] Recent reports suggested that TCR–pMHC interactions are susceptible to mechanical force.[12] Some biophysical techniques have demonstrated that the mechanical force instigates agonist-specific TCR-pMHC interaction across the T-cell-APC interface and also plays a vital role in triggering proximal intracellular Ca^{2+} signalling in T-cell.[12]

Liu *et al.* investigated on how the force mechanically regulates antigen discrimination by TCR, which triggers Ca^{2+} influx and determines the force's magnitude and duration necessary for T-cell triggering (Figure-1).[11] Using the BFP technique, they showed that the magnitude and duration of force are essential, and force prolongs the lifetime of TCR-pMHC (agonist) bond that behave as a catch-bond. At the same time, it shortens the lifetime of the antagonist, i.e. acts as a slip-bond.
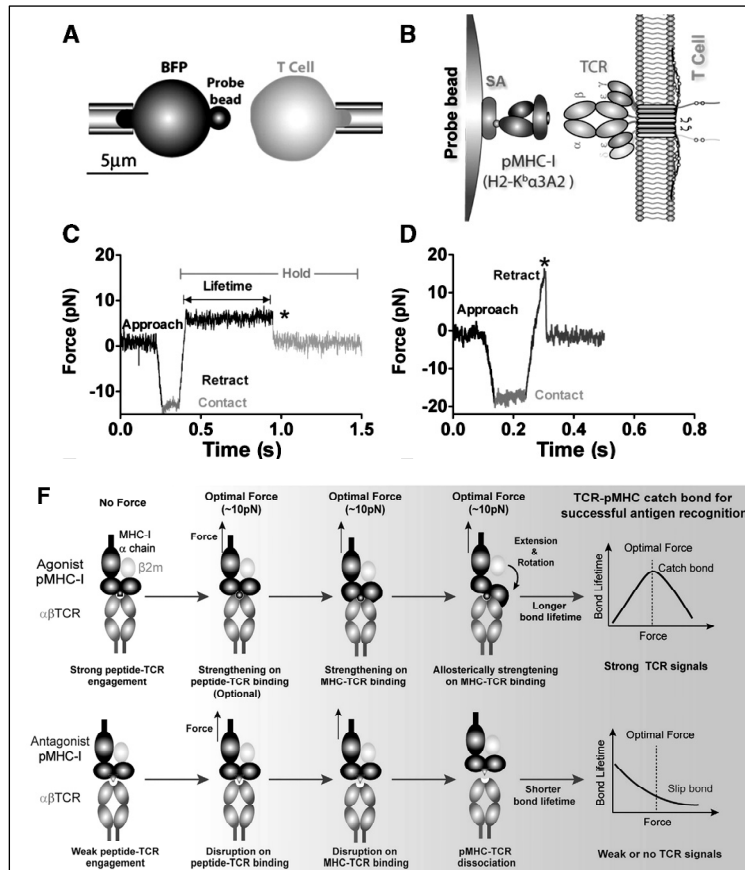
Figure-1: Catch-bond triggering the TCR antigen recognition. (A) A schematic representation of bio-membrane force probe (BFP) experiment. A red blood cell (RBC) with a bead was attached to a micropipette (left), and T-cell was connected (right) with micropipette applying negative pressure on cell membrane. (B) The probe bead was covalently attached with a streptavidin linker to capture the pMHC-I to interact with TCR. (C) The representative diagram of T-cell-pMHC adhesion interaction for the bond lifetime measurement. First, the two cells come in contact for some time. Upon retraction, they have shown a ramping and sustained preset level of force until the dissociation takes place (marked by a red star). (D) The adhesion of T-cell and pMHC is ruptured by a ramp force (indicated by a magenta star) and then undergoes force-ramp assay. Figures are reprinted with permission from Elsevier Publishers Ltd: Cell, Baoyu Liu, Wei Chen,

Brian D. Evavold, Cheng Zhu, 2014, 157, 357–368. (F) Conformation change study of TCR-pMHC interaction in the presence of agonist and antagonist to distinguish the role of catch-bond and slip-bond. Figures are reproduced with permission from Elsevier Publishers Ltd: Molecular Cell, Cheng Zhu et al., 2019, 73, 1015–1027.

      In Figure-1(A-D), Liu *et al.* demonstrated a 2D single bond lifetime study on a naive T-cell (OT1 transgenic mouse) under a range of constant force applied via pMHC.[11] This technique used a red blood cell (RBC) attached to the top of the micropipette with a glass bead as a force inducer (Figure-1A, left), and this probe is coated by pMHC (Figure-1B, left), acts as a surrogate APC. In each experiment cycle, the T-cell attached to the top of the micropipette was driven to contact the bead to induce bond formation (Figure-1A).[11] To prevent the multi bond formation, the contact time of the T-cell and pMHC was kept at about 100 ms, and the pMHC was mutated to avoid the CD8+ binding in the T-cell. During the T-cell retraction process, a tensile force will be developed. The TCR-pMHC interaction was jumped and held to a preset level (Figure-1C) until and unless bond dissociation occurs, and in this condition, force lifetime was measured. In Figure-1D, it was shown that some bonds might fail to reach the clamp phase, which is unable to produce a lifetime. To confirm that most of the binding event was driven by single bond formation, the pMHC concentration was kept lower on the probe, which reduces the adhesion frequency (no. of adhesion divided by no. of contact). They also demonstrated with null pMHC to confirm the binding, and the T-cell adhesion was not detected, which confirmed that TCR does not have any binding affinity towards null peptide. They also suggested[11] that a greater force is required for a more activating peptide to display more lifetime than the less activated peptide. The authors then used the fluorescence optical path to this device to observe cytoplasmic Ca^{2+} flux signalling by using sensitive Ca^{2+} sensing dye. A dramatic biphasic curve of calcium vs force reveals that pMHC-Ca^{2+} responses induced lifetime peaks at 10 pN force via catch-bond, and antibody interaction behaves as slip bonds with a lifetime 0 pN.

      Figure-1F (top) represents a schematic of dynamic structural model for mechano chemical coupling of force regulated TCR-pMHC bond on antigen inspired by Wu *et al.*[15] This diagram consists of three steps: (1)

TCR-antigen recognition initiated by the complementary determining region (CDR) loops of the TCR to engage the hotspot residue in the agonist peptide, (2) the MHC$\alpha_1\alpha_2$ residue pull towards the CDR loops because of the engagement of hotspot residue with CDR, and (3) such strengthening in the force of the TCR-pMHC bond tolerates the separation of the β2m motif from an pMHC chain, and the MHC$\alpha_1\alpha_2$ domain rotates towards the TCR.[15] These three forces induced steps lead to the conformational change in pMHC and produce a catch-bond. But the antagonist pMHC could not instigate any changes due to the weak interaction (Figure-1F, bottom) and produced a slip-bond. This agonist and antagonist specific TCR-pMHC interaction confirms the hypersensitivity of TCR to discriminate cognate from the ocean of non-stimulatory antigen, which is unable to trigger T cells. In the T-cell activation pathway, the TCR-pMHC interaction is the only antigen-specific interaction, and the catch-bond is a characteristic property of the interaction. But the major unanswered question is whether the catch-bond formation is an intrinsic feature or an outcome of a complex cellular system. Limozin *et al.*[16] explored 2D TCR-pMHC interaction under force in a cell-free system in a force range (6 to 15 pN) to answer whether the behaviour of TCR–pMHC bond is intrinsic or not. The laminar flow experiment claimed that the catch-bond formation is an extrinsic feature because it was not dissociated for agonist TCR-pMHC ligand pairs under cell-free conditions. Using the same experiment, they propose an association model where the binding occurs after a nominal encounter duration, indicating that membrane and dynamics fluidity firmly control the bond formation.[16]

Role of Ca^{2+} for Dynamic and Conformation Change of TCR:

T-cells consist of TCR$\alpha\beta$ heterodimer and three signalling subunits in CD3 complex-εδ and εγ heterodimer, and ζζ homodimer, which are associated through hydrophobic interaction and play a critical role in the adaptive immune system.[5] A very low abundance of agonist pMHC can trigger an antigen-specific immune response.[2] The exchange of TCR$\alpha\beta$ and CD3 subunit is the central player for translating TCR-pMHC binding kinetic to phosphorylation of CD3 immuno receptor tyrosine-based activation motifs (ITAM), which Lck primarily mediates.[17] It has been suggested that the acidic phospholipid can interact with CD3ε and CD3ζ units to initiate ITAM phosphorylation within the plasma membrane and initiate the T-cell

activation.[17] In the resting state of T cell, spontaneous phosphorylation of ITAM is prevented because it is inserted in the hydrophobic lipid membrane of the CD3ε and CD3ζ chain. ITAM needs to be dislodged from the plasma membrane hydrophobic core and be available for Lck protein to continue the phosphorylation process.[18] Shi *et al.* [18] investigated how CD3 dissociate from the membrane and the effect of Ca^{2+} on facilitating the ITAM phosphorylation by the NMR spectroscopy and live-cell fluorescence resonance energy transfer method. The equilibrium based microdialysis assay and fluorescence polarization experiment reveal that Ca^{2+} directly impaired the interaction of CD3ε and CD3ζ with anionic phospholipid POPG even when the concentration of Ca^{2+} is ten times lesser than lipids. The FRET data measured in live Jurkat T-cells supports that Ca^{2+} could directly change the local electrostatic environment by interfering with CD3 membrane interaction. The phosphorylation of CD3 is only dependent on the charge of Ca^{2+}; no other Ca^{2+} dependent signalling pathway is also confirmed when the non-physiological cation (Sr^{2+}) interferes with the CD3-membrane.[18]

One dimensional ^{31}P NMR spectroscopy discloses an attractive mechanism for how Ca^{2+} impacts the chemical environment of CD3–membrane interaction and facilitates CD3 phosphorylation to enhance the sensitivity of T-cells towards foreign antigens.[18] By the NMR studies, it was confirmed how Ca^{2+} binding changes the chemical shift of phosphorus lipid signal of anionic lipid 1-palmitoyl-2-oleoyl-sn-glycero-3-phospho-(1'-rac- glycerol) (POPG) but not the zwitterion lipid 1-palmitoyl-2-oleoyl-sn-glycero-3-phosphor-choline (POPC). A similar chemical shift is observed for the phosphorus ligand-induced by CD3ε$_{CD}$ bind region, which indicates that the Ca^{2+} ion and CD3ε$_{CD}$ bind to the same region of anionic lipid phosphate. They have also shown an unambiguous perturbation effect at the low micromolar level of Ca^{2+} confirms the impact of Ca^{2+} at physiological concentration is relevant to activating the T-cell. This study reveals the role of Ca^{2+} for initializing and amplifying antigen-stimulated TCR signaling with a schematic representation of Ca^{2+} induced TCR signalling.[18] There is a safety control mechanism in the resting state of triggering where CD3εζ cytoplasmic domains (positively charged) interact with the phospholipid (negatively charged), situated in the inner part of the plasma membrane.

After a few seconds of TCR triggering, Ca^{2+} influx started, and it persisted in synapsed of T-cell for several hours. Then the positively charged Ca^{2+} ions in the vicinity membrane can bind the negatively charged phosphate group of phospholipids and instigate the dissociation mechanism of the CD3εζ chain from the membrane by neutralizing the charge and increasing the availability of ITAM for the Lck. In this way, Ca^{2+} can facilitate the phosphorylation process of the TCR-CD3 complex inside the membrane, even in low-affinity self-antigens. Hence, the hypersensitive feature of T-cell, even for a single antigen explained from the Ca^{2+} regulation mechanism, intensifies the initial antigen-stimulated signal to such a greater extent. In addition, the persistence of high Ca^{2+} concentration help to prolong the TCR signaling at the synapse and is needed to maintain the sustainability of the full potential of the T-cell.
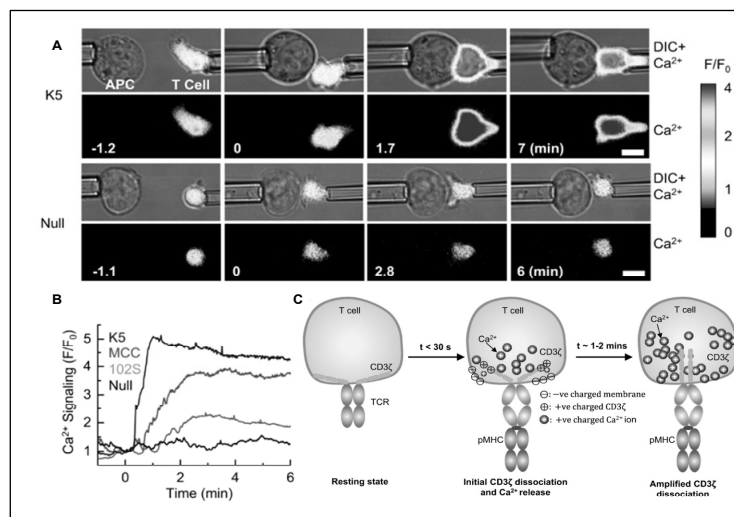
Figure-2: (A) Micropipette adhesion frequency analysis of real time-lapse microscopy to study calcium signalling in T cell. On the very top, there is a super agonist peptide MHC (pMHC) coated on red-blood cell (RBC), and another pipette loaded T-cell with Fluo-4 calcium indicator was driven by a piezoelectric translator. The observed fluorescence signal was recorded at 37 ^{0}C, and the increased Ca^{2+} signal (F/F$_0$) is shown in the colour baron right-hand side. (B) Representative plot of Ca^{2+} flux (F/F$_0$) signal for the super agonist (K5), agonist (MCC), weak agonist (102S) and null peptide. (C)

Schematic diagram of change in conformation of TCR-CD3ζ was observed when Ca^{2+} influx was observed in the plasma membrane. The Ca^{2+} neutralize the negative charge of anionic phospholipids, and the ITAM buried in the hydrophobic core on lipid membrane is released and becomes accessible for phosphorylation by Lck. The figure is reproduced from Springer Nature Publication: D. K. Sasmal et al., Cellular & Molecular Immunology **2020**, 17, 203-217 with permission.[5]

One question arises: how TCR can discriminate the foreign and self-peptides on the antigen-presenting cell surface. Sasmal *et al.*[5] investigated an experimental phenomenon of dramatic conformational change of ITAM associated with Ca^{2+} fluxwhen TCR$\alpha\beta$ interacts with pMHC, and CD3ζ changes conformation inside the cell membrane, which induces TCR triggering. They designed a new method - fluorescence micropipette assay to measure real-time Ca^{2+} signallingin T-cell when it interacts with APC. They also developed a micropipette adhesion assay to measure two-dimensional TCR-pMHC binding kinetics to predict the TCR conformational change upon binding, signalling and activation. Their data unveils that the binding affinity is correlated with the pMHC potency. The shorter bond length of TCR-pMHC increased the TCR-pMHC binding affinity. Intracellular Ca^{2+} influx was observed (2-5 times) upon the contact of the T-cell on the surface of the antigen-presenting cell, and the amplitude and speed of calcium signaling depend on the potency of the peptide (Figure-2B). For the super agonist K5, the Ca^{2+} is the highest, and for a weak agonist 102S, the calcium signalling is near the null peptide range (Figure-2B). To connect the TCR conformational change with TCR signalling, they plotted the conformational change of TCR–CD3ζ chain with the Ca^{2+} concentration against the stimulation time. They found similar behavior depending upon the potency of pMHC on the CD3ζ conformational change where calcium ion in flux initiates the dissociation of positively charged CD3ζ chain from the plasma membrane of phospholipids ITAM for phosphorylation (Figure-2C).

The catalytic part of TCR is controlled by the Lck, a membrane-anchored kinase from the Src family and phosphatase (CD45);[19] it does not contain any intrinsic catalytic feature. Upon the TCR ligation with pMHC, the Lck kinase phosphorylated the tyrosine residue distributed in ITAM,

later accessible for zeta chain associate protein kinase (ZAP70) and it became phosphorylate, the linker for activated T cell (LAT).[19] NMR study already confirmed that the ITAMs are inserted in the hydrophobic core of phospholipids, and the Ca^{2+} signalling effectively regulates the disrupt the interaction.[18] The probable cause of CD3 dissociation is the Ca^{2+} encapsulation, directly associated with the negatively charged phospholipids and lowers the electrostatic interaction between lipid membrane and ITAM.[20] Not only is the dissociation of the CD3 tail but Ca^{2+} is also caused by TCR clustering, which further enhances the T cell activation by the FRET experiment.[5] A recent study also suggests that the CD3-ITAM association is likely to be accessible for a long time, a dynamic process existing in multiple membrane-bound conformational states.[20] In this approach, TCR activation can be characterized in a reversible module. ITAM acts as a substrate for Lck and CD45 and is activated only when the Ca^{2+} interacts with the lipid membrane. Dushek et al.[19] well explained the critical step for the TCR triggering. They stated that phosphorylated TCR concentration could be determined from the relative concentration of active Lck and CD45.[19]
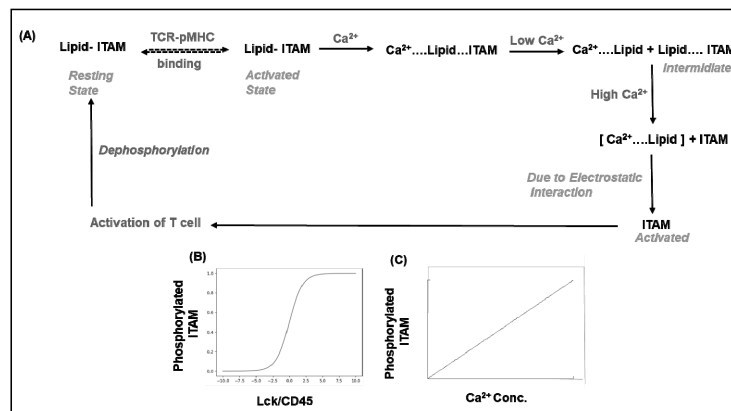
Figure-3: (A) Proposed schematic presentation of binding and unbinding kinetics of ITAM, Lipid and role of Ca^{2+} ion. (B) The relative number of phosphorylated ITAM is expected to vary by the concentration ratio of ([Lck]/[CD45]). With increasing the phosphatase, more ITAM is activated. (C) The number of phosphorylated ITAM is also related to the Ca^{2+}ion concentration in the plasma membrane. The ionic interaction between the

phospholipids and Ca^{2+} helps to release the ITAM from the hydrophobic core.

Readers, please note that all the schematic representations proposed here are not the result of experiments; they are only hypothetical approaches.

Proposed Kinetics of Interaction of ITAM with Lipid and Ca^{2+} Ion:

We have proposed a scheme in Figure-3A to understand the kinetics of interaction of lipid and ITAM and the role of Ca^{2+} for T-cell activation. T-cell is activated by the interaction of extracellular TCR and pMHC, and the change of TCR conformation is dramatically dependent on the potency of peptide represented by MHC complex. However, this extracellular conformational change and signalling effect inside the cell by increasing intracellular cation concentration released by ER. Ion concentration is increased by 2-10 times, and speed of this flux depends on the potency of peptide. When low concentration of Ca^{2+} interacts with the lipid membrane, ITAM goes through an intermediate state, and it is not phosphorylated. If the Ca^{2+} concentration is very low in the system, enough ITAM is not released from the membrane. It is expected that the concentration of Ca^{2+} will determine the activated CD3ζ chain of ITAM. However, high concentration of Ca^{2+} helps to detach the ITAM chain from the lipid membrane. Electrostatic interaction between Ca^{2+} and negative charge of ITAM may also play crucial role in the dissociation of chain from lipid membrane. Hypothetical amplitude of phosphorylation of ITAM with the ratio of Lck/CD45 is given in Figure 3B. In addition, the amplitude of calcium concentration and phosphorylated ITAM (Figure 3C) can also be hypothetically plotted as a linear curve, which means Ca^{2+} and ITAM phosphorylation are directly correlated. It is also speculated that there is a possibility of non-linear growth of phosphorylation because of reported flux of Ca^{2+} in cells.

Conclusion:

Ca^{2+} ion concentration is directly correlated with the activation of T-cell, which is initiated by the extracellular interaction between TCR and pMHCs. The kinetics of Ca^{2+} ion flux is generally non-linear in nature, which takes – (1) 10-15 seconds at the initial state with no change of ion, (2) 2-5 seconds to increase calcium flux by 5-10 times and reach at maximum, and (3) next

2-30 mins where Ca^{2+} concentration will remain either at constant concentration or slowly decrease as long as T-cell remains activated. The speed of Ca^{2+} flux is again directly correlated to the potency of antigen, where strong agonist induces the flux much faster than weak agonists. Although conformational change of TCR is extremely difficult to know in cellular and tissue level conditions, it was reported that the binding of pMHCon TCR induces triggering of Ca^{2+}, which significantly changes the conformation of cytoplasmic ζ-chain. We have proposed a hypothetical schematic kinetics model on how ITAM, Ca^{2+} ion and lipid membrane interact with each other, which may give a mathematical perspective on the time-scale of interaction and following conformational change of ITAM. Although Ca^{2+} signalling in T-cell is studied extensively in cellular level with few boundary conditions, a tissue level understanding without any boundary conditions will give much better understanding on the role Ca^{2+} ion on human adaptive immune system.

Acknowledgement:

Reference:

1. La Gruta, N. L.; Gras, S.; Daley, S. R.; Thomas, P. G.; Rossjohn, J.; Nature Reviews Immunology 2018, 18, 467-478.
2. Huang, J.; Brameshuber, M.; Zeng, X.; Xie, J.; Li, Q.-j.; Chien, Y.-h.; Valitutti, S.; Davis, M. M.; Immunity 2013, 39, 846-857.
3. Wilson, I. A.; Garcia, K. C.; Current opinion in structural biology 1997, 7, 839-848.
4. Van Der Merwe, P. A.; Dushek, O.; Nature Reviews Immunology2011, 11, 47-55.
5. Sasmal, D. K.; Feng, W.; Roy, S.; Leung, P.; He, Y.; Cai, C.; Cao, G.; Lian, H.; Qin, J.; Hui, E.; Cellular & Molecular Immunology 2020, 17, 203-217.

6. Trebak, M.; Kinet, J.-P.; Nature Reviews Immunology 2019, 19, 154-169.
7. Feske, S.; Nature Reviews Immunology 2007, 7, 690-702.
8. Vaeth, M.; Kahlfuss, S.; Feske, S.; Trends in immunology 2020, 41, 878-901.
9. Bhakta, N. R.; Oh, D. Y.; Lewis, R. S.; Nature immunology 2005, 6, 143-151.
10. Feske, S.; Okamura, H.; Hogan, P. G.; Rao, A.; Biochemical and biophysical research communications 2003, 311, 1117-1132.
11. Liu, B.; Chen, W.; Evavold, B. D.; Zhu, C.; Cell 2014, 157, 357-368.
12. Chen, L.; Flies, D. B.; Nature reviews immunology 2013, 13, 227-242.
13. Dembo, M.; Torney, D.; Saxman, K.; Hammer, D.; Proceedings of the Royal Society of London. Series B. Biological Sciences 1988, 234, 55-83.
14. Kim, S. T.; Takeuchi, K.; Sun, Z.-Y. J.; Touma, M.; Castro, C. E.; Fahmy, A.; Lang, M. J.; Wagner, G.; Reinherz, E. L.; Journal of Biological Chemistry 2009, 284, 31028-31037.
15. Wu, P.; Zhang, T.; Liu, B.; Fei, P.; Cui, L.; Qin, R.; Zhu, H.; Yao, D.; Martinez, R. J.; Hu, W.; Molecular cell 2019, 73, 1015-1027. e1017.
16. Limozin, L.; Bridge, M.; Bongrand, P.; Dushek, O.; van der Merwe, P. A.; Robert, P.; Proceedings of the National Academy of Sciences 2019, 116, 16943-16948.
17. Kuhns, M. S.; Davis, M. M. Cell 2008, 135, 594-596.
18. Shi, X.; Bi, Y.; Yang, W.; Guo, X.; Jiang, Y.; Wan, C.; Li, L.; Bai, Y.; Guo, J.; Wang, Y. Nature 2013, 493, 111-115.
19. Dushek, O.; Frontiers in immunology 2012, 2, 91.
20. Ma, Y.; Poole, K.; Goyette, J.; Gaus, K. Frontiers in immunology 2017, 8, 1513.

Comparative Study of the Oxidation Products of Succinic acid in Conventional and Microwave Heating Conditions

✎ *Dr. Manju Kumari*

Department of Chemistry, Maharaja College, Ara, Bihar-802301, India.

E-mail: manjupandeya@gmail.com

Introduction:

Succinic acid or butandioic acid is a dicarboxylic acid and historically it is known as *spirit of amber*. Its carboxylate anion is an important member of the TCA cycle.[1] The expected oxidation products of succinic acid are HOOC-CO-CH$_2$COOH, CH$_3$CH$_2$COOH, OHCCOOH, OHC-CH$_2$-COOH, HOOC-CH$_2$-COOH, HOOC-COOH, HCOOH, OHC-CHO, CH$_3$-CO-COOH etc. A large number of chromium (VI) based oxidants as complexes of organic ligands like Collin's reagent,[2] Pyridinium chlorochromate (PCC),[3] Pyridinium dichromate (PDC),[4] 2,2'-bipyridinium chlorochromate (BIPCC),[5] Pyridinium fluorochromate (PFC),[6] Tetramethyl ammonium fluorochromate (TMAFC),[7] N-methyl benzyl ammonium fluorochromate (MBAFC),[8] Quinolinium chlorochromate[9] etc. have been developed for the organic synthetic work. Ditertiary butyl chromate (TBC)[10] & Ditertiary amyl chromate (TAC) are the two important variants which have been found to be highly efficient and easy to handle oxidants for organic substrates. The oxidation of chromium from III to VI is an important environmental process because Cr (VI) is easily taken up by cells & is subsequently reduced to the trivalent III form. The formation of Cr (III) or other intermediate oxidation states such as V or IV is believed to play a role in the adverse biological effects of Cr (VI) compounds.[11] Cr(VI) as health hazard has been studied.[12] The study of redox processes involving Cr(VI) and organic substrates e.g. succinic acid, thus becomes more important in view of the toxicity of Cr(VI), the role of Cr(III) in activation of insulin in sugar patient[13] and involvement of succinic acid or its anion in many biological processes. G.

D. Mishra and Mary Lily Kujur[14] have reported the oxidation of succinic acid by TAC in dioxane as solvent for the substrate. Very recently, H. O. Pandey and R. Singh[15] have studied and reported the oxidation of succinic acid by Ditertiary amyl chromate (TAC) in different molar ratios by conventional heating method.

Keeping in view the increasing application of microwave irradiation as a source of clean energy, the authors undertook the oxidation of succinic acid by TBC and TAC in different molar ratios by such non-conventional method. The medium has been kept non-aqueous throughout the experiments. The solvents used for the substrate were dioxane and tetrahydrofuran (THF). Important inferences have been drawn on the basis of study of the six products formed under microwave irradiation conditions and their comparison with the results obtained by conventional heating as reported by earlier authors.[15]

Results and Discussion:

The chemicals used were of A. R. grade. Freshly prepared solutions were used. The solubility of the products was also tested in water. The experimental methods used in the present work consist of mainly:

a) **Preparation of TBC & TAC:** The oxidants i. e. TBC & TAC, have been prepared by dissolving accurately weighed amount of dry & powdered chromium trioxide in calculated volumes of tertiary butyl alcohol and tertiary amyl alcohol respectively at room temperature. Care was taken to avoid bigger pieces of CrO_3 as this may lead to catching fire.

b) **Preparation of the solutions of succinic acid in different solvents**: Weighed amount of succinic acid was dissolved in 10 ml of the solvents i.e 1,4-dioxane and THF in a clean & dry beaker with constant stirring.

c) Oxidation of succinic acid with TBC & TAC: The solution of oxidant and that of substrate, prepared as above were mixed with constant stirring before subjecting to microwave irradiation. The substrate:oxidant ratios (S:O ratios) used were 2:1, 1:1 and 1:2. Precautions were taken to avoid any violent reaction at the time of mixing. The solid products obtained were washed several times with acetone to remove the soluble impurities, unreacted CrO_3 or the substrate, if any, before collecting in clean, airtight glass bottles. The microwave heating was done in an LG-microwave oven, MG-3937C (microwave frequency 2450 MHz). Table-2 shows the reactants and reaction conditions in brief.

d)   Estimation and Characterization: The estimation of chromium in the products was done volumetrically using potassium persulphate (in excess), 0.1 N potassium dichromate solution and 0.1 N Mohr's salt solution. Percentage composition of carbon & hydrogen were estimated using "Elemental Analyser – Heraeus Vario EL III Carlo Erba 1108". The oxygen content was found out by subtraction of sum of total of percentage composition of C, H & Cr from 100. The IR spectrum of the products was recorded on a "Fourier Transform Infrared Spectrophotometer – Shimadzu 8201 PC". The Thermogravimetric and differential thermal analysis (TG-DTA) of the compounds were carried out on "Thermal Analysis System – Perkin Elmer Diamond TG/DTA." The samples were heated at a rate of 10^0C/min. in the temperature range of room temperature to 700^0C. Table-1 and 2 contains the reaction conditions under ordinary heating condition as reported by earlier workers[15] and the same carried out by the authors of the present paper under microwave irradiation respectively. Table-3 and 4 contains the corresponding results.

Table-1:

Products code	Solvent	Oxidation	S:O ratio	Heating duration
SH-01	THF	TAC	2:1	45 min
SH-02	THF	TAC	1:1	30 min
SH-03	THF	TAC	1:2	20 min

Table-2:

Product code	Solvent	oxidant	S:O ratio	Heating condition	Time (min)
SA-01	THF	TBC	2:1	MW (160 W)	8.16
SA-02	THF	TBC	1:1	MW (160 W)	2.50
SA-03	THF	TBC	1:2	MW (160 W)	1.66
SA-04	Dioxane	TAC	2:1	MW (160 W)	8.00
SA-05	Dioxane	TAC	1:1	MW (160 W)	1.83
SA-06	Dioxane	TAC	1:2	MW (160 W)	3.66

Table-3:

Product code	Colour	Solubility in water	Empirical formula	Proposed molecular formulation
SH-01	Greenish brown	Insoluble	$C_7H_{11}O_8Cr_2$	$CrO.HOOC(CH_2)_2COOH$ CH_3CH_2COOH
SH-02	Greenish brown	Insoluble	$C_4H_6O_4Cr$	$Cr_2O.2CH_3COOH$
SH-03	Greenish brown	Insoluble	$C_5H_9O_7Cr_2$	$Cr_2O.HCOOH.HOOC$ $.(CH_2)_2COOH$

Table-4:

Product code	Colour	Solubility in water	Empirical formula	Proposed molecular formulation
SA-01	Light brown	Insoluble	$Cr_2C_5H_{14}O_8$	$Cr_2O.CH_3COOH.CH_3\text{-}CO\text{-}COOH.2H_2O$
SA-02	Dark grey	Insoluble	$Cr_2C_5H_{11}O_6$	$Cr_2O.CH_3CHO.OHC–CH_2–COOH. H_2O$
SA-03	Dirty brown	sparingly soluble	$Cr_2C_5H_{15}O_{10}$	$Cr_2O_3.CH_3CHO.CH_3\text{-}CO\text{-}COOH. 3H_2O$
SA-04	Light brown	sparingly soluble	$Cr_2C_5H_{12}O_8$	$Cr_2O.CH_3COOH.CH_3\text{-}CO\text{-}COOH.2H_2O$
SA-05	Dark maroon	Insoluble	$Cr_2C_4H_{10}O_7$	$2CrO.2CH_3COOH.H_2O$
SA-06	Dark maroon	Insoluble	$Cr_2C_5H_{14}O_{11}$	$Cr_2O_3. HCOOH. (CH_2COOH)_2. 2H_2O$

Conclusion:

The observations, as reported in the four tables clearly indicate that the organic synthetic processes may be carried out more efficiently and more rapidly and of course at the cost of less energy in the form of microwave irradiation. We can, thus, make the following generalizations on that basis:

The oxidation of succinic acid can be carried out in much less time by the application of microwave irradiation as compared to the classical method of heating. The time required for the purpose in different molar ratios as in table-1 are 45 min, 30 min and 20 min whereas the same molar ratios of substrate and oxidant require times less than 10 minutes in all the cases as in table-2

TBC and TAC are equally efficient as oxidants. Time required in the two cases is almost same.

The colour of the products changes from light brown to dirty brown or dark maroon on increasing the ratio of oxidant which may be due to different oxidation states of chromium in different products.

The extent of oxidation of the substrate increases as the ratio of the oxidant increases. This is substantiated by the presence of CH_3CH_2COOH, CH_3COOH and $HCOOH$ in SH-01, SH-02 and SH-03 respectively. Almost same observation is made when we go from SA-04 to SA-06. The fragments are CH_3-CO-COOH, CH_3COOH and HCOOH along with other ligands. The trend is not so clear in SA-01 to SA-03.

In case of SA-03 and SA-06 when the ratio of oxidant is maximum, the most stable oxidation state i.e. III is observed in the form oxide Cr_2O_3. In other cases oxidation states of chromium are less than III.

Interestingly, water molecules are absent in products SH-01, SH-02 and SH-03 obtained by oxidation by ordinary heating of the substrate whereas they are invariably present in the products obtained by microwave heating. This clearly indicates that the escape of water as well as other comparatively volatile products is more probable in heating process than in microwave irradiation.

The oxidation is more efficient in dioxane than in THF as supported by the presence of less oxidized aldehydes in SA-02 and SA-03. There are no such products in SA-04, SA-05 and SA-06 where the solvent is dioxane.

References:

1. a) Lane, Nick; W. W.; Norton and Co, ISBN 0-393-06596-0, 2009; b) Collins, J. C.; Hess, W. W.; Frank, F. J.; Tetrahedron Lett. 3363,1968.
2. Corey, E. J.; Suggs, J. W.; Tetrahedron Lett., 2647,1975.
3. Corey, E. J.; Schmidt, G.; Tetrahedron Lett., 399,1979.
4. Guziec, F. S.; Luzzio, F. A.; Synthesis, 691, 1980.

5. a) Bhattacharjee, M. N.; Choudhary, M. K.; Dasgupta, H. S.; Roy, N.; Synthesis, 588, 1982; b) Bhattacharjee, M. N.; Choudhary, M. K.; Purkayastha, S.; Tetrahedron Lett. 1987, 43, 5389.

6. Kassaee, M. K.; Mahjoub, A. R.; Ghammami, S.; Tetrahedron Lett. 44, 4555-4557, 2003.

7. Kassaee, M. K.; Sajjadi-Ghotbabadi, H.; Sayyed- Alangi, S. Z.; Pittcon 2003, March 9-14, 2003 Orlando, Florida, Abstracts 1200-7p.

8. Srinivasan, R.; Ramesh, C. V.; Madhulatha, W.; Balasubramanian, K.; Indian J. Chem. Sec. B. 1996, 35B, 480.

9. Oppenauer, R. V. and Oberrauch, H. (Univ. Innsbruck, Austria), Anaus Assoc. Guin- Argentina 37, 246-62, 1949.

10. Barnhard, M.; J. Soil Contam., 1997, pp: 6p,561.

11. Das A. P., Mishra. S; Journal of Environmental Research and Development, Vol-2, No- 3, Jan-March, 2008.

12. Thorn, M. B., Biochem. J., Vol.49 (5), pg. 602-609, 1951, PMC1197563.

13. Mishra, G. D.; Mary Lily Kujur, Thesis, Ranchi University, Ranchi, 1993.

14. Pandey, H. O.; Rasika Singh, Thesis, Ranchi University, Ranchi, 2010

15. Malik, M. A.; Ai-Nowaiser, F. M.; Ahmad, N.; Khan, Z.; Int. J. Chemical Kinetics, DOI 10.1002/kin.20519,2010, wiley onlinelibrary.com

CHAPTER
4

Impedance Spectroscopy Genetic Programming Analysis Ion Conduction Mechanism in Semi-Interpenetrating Polymer Networks

✍ *Dr. Nimai Bar*

Department of Chemistry, Raja N. L. Khan Women's College, Paschim Medinipur, West Bengal-721102, India.

E-mail: nimaibar635@gmail.com

Introduction:

The first solvent-free polymer electrolyte complex with alkali metal salts was labelled by Peter. V Wright.[1] Unfortunately, this solid polymer electrolyte (SPE) shows poor performance at ambient temperature, which is a barrier to its utility compared to the existing conventional liquid/gel electrolytes.[2] Numerous research works have been carried out to enhance its electrochemical properties and ambient temperature ionic conductivity through blending of polymers,[3] crosslinking,[4] insertion of nano structured oxide materials,[5] plasticization and doping with ionic salts. Utilization of doping salts which form low-temperature eutectics with polymers was found to be a useful approach for obtaining good flexibility of the polymer chains that are responsible for the ion transport process. Solid polyether-based electrolytes, in particular modified polyethylene oxide (PEO), have shown favorable properties, in terms of ideal solid polymer electrolytes: good ionic conductivity combined with thermal, electrochemical, dimensional and mechanical stability. Several studies have been carried out to investigate the mechanism of ionic transport in SPEs, using neutron scattering, nuclear magnetic resonance (NMR), X-ray diffraction (XRD), and computer simulation.

Most of the good ionic conducting polymers have a sort of dual guest-host structure of network frame; a soft part for ionic conduction and a hard part backbone. In this perspective, we have successfully developed new semi-interpenetrating network polymer-salt complexes as SPEs. The

structural modifications on these semi-IPN systems have been done to achieve good ionic conductivity, dimensional stability, and thermal stability at ambient temperature without using external plasticizers. The SPE shows promising ionic conductivity of 10^{-4} -10^{-3} S/cm at ambient temperature without using supplementary plasticizers. The ion transport mechanism has been studied in detail by electrochemical impedance spectroscopy (EIS).

The experimental EIS data is analyzed here by ISGP, finding the distribution function of relaxation times (DFRT) according to

$$Z(\omega) = Z(\infty) + R_{pol} \int_{-\infty}^{\infty} \frac{\gamma(\log(\tau))}{1 + i\omega\tau} d(\log(\tau)) \qquad (1)$$

where $Z(\omega)$ is the impedance, ω the frequency, R_{pol} the total resistance, the DFRT, and τ the relaxation time. ISGP finds an *analytical form* of the DFRT that has the form of a peak or a sum of several peaks, while ensuring that the chosen function would have minimal number of peaks or free parameters, using discrepancy-complexity approach. The convolution of the DFRT with the Debye kernel (see eq. 1), should fit the measured data. Finding analytical form of the DFRT (rather than a point-by-point function as, e.g., with Fourier transform) can aid in developing a physical model and examining its behavior.[6] ISGP has been demonstrated on electrochemical systems such as SOFC cathode half cells and anode half cells, SOFC-SOEC full cells, supercapacitors and pseudo-supercapacitors. Here we continue these efforts and expand it to analyze the ion-conduction of the PEO-PU/ PEGDME:Li-ClO$_4$ solid semi-IPN matrix.

Experimental:

Synthesis of PEO-PU/PEGDME: Semi-IPN PEO-PU/PEGDME served as the polymer host matrix and Li-X (X=ClO$_4^-$, I$^-$/I$_3^-$, N(CF$_3$SO$_2$)$_2^-$ and CF$_3$SO$_3^-$) salts used for complexations. The semi-IPN polymers were synthesized using two consecutive steps. The first step is synthesis of polyurethane (PEO-PU) network polymer; the second step consists of incorporation of oligomer (PEGDME) and lithium salt into the network polymer. Typically, in a 25 ml round bottom flask, castor oil (CO) and diphenylmethane diisocyanate (MDI) were mixed in tetrahydrofuran solvent, degassed and

stirred under passive atmosphere for about 30 minutes for polymerization. In another flask, homogenous mixtures of oligomer (PEGDME), catalyst (DMA), PEG and lithium salt, were merged in equal volume (1:1) of tetrahydrofuran and acetonitrile. The clear solution was charged into the reaction mixture in the first flask. The reaction mixture was degassed and stirred for another half an hour under inert atmosphere to get homogenous solution. The reaction mixture was poured into a glass petri-dish, kept at room temperature for 24 hours and then at 80 C in an oven for about 48 hours for curing. The obtained semi-IPN solid polymer electrolytes were designated as PEO-PU/PEGDME. The constituent composition for primary and secondary weight ratios used are 60/40, 50/50, 40/60 and 30/70. The salt concentrations (EO/Li mole ratio) used for the current study are 100, 80, 60, 40, 30, 20 and 10. During the synthesis the ~OH/NCO (hydroxyl/isocyanate) ratio is maintained 1:1.2.

Characterization: Impedance spectroscopy of the solid polymer electrolytes film was measured by Zahner@Zennium electrochemical impedance analyzer. The samples were placed in a cell configuration of SS/SPE/SS in Swagelok cell, where SS stands for stainless steel blocking electrode. The AC signal amplitude was10 mV. The temperature was varied between 23 C to 90 C at intervals of ~7 C. The frequency range was 1Hz-4MHz; 10 measuring points per decade.

Impedance spectroscopy:

Numerous research articles exist in the literature for impedance analyses of solid polymer electrolytes. In most of the reports the analysis is based on equivalent circuits or universal power law fittings. Here we apply an alternative analysis technique, ISGP, based on evolutionary programming. It finds an analytic form of the underlying distribution function of relaxation times (DFRT) as briefly explained in the introduction above.
The DFRTs of the solid polymer electrolyte cells consist of two peaks at different frequencies/ relaxation times, where the peak positions and are as depend on the constituent polymers, salt concentrations and temperatures. In our previous study we have estimated relaxation time from Debye plots (log$f$ vs –Z''). The Debye plots were fitted with Lorentzian function and at peak

maximum τω=1 satisfied. Here the relaxation times resulted directly from the peak central position in the DFRT. In some cases, where Debye plots fail to provide relaxation times, ISGP do find; yet an additional benefit.
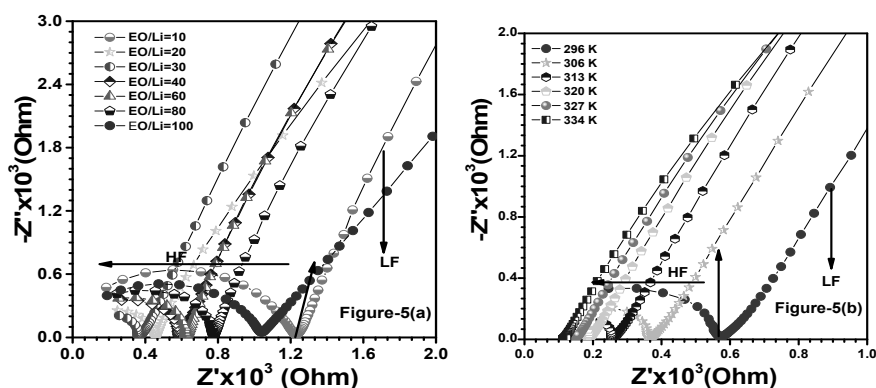
Figure-1: (a) Nyquist plots (Z'*vs*–Z", not in scale) for the solid polymer electrolytes containing different salt concentrations. **(b)** Nyquist plots (not in scale) at different temperatures of PEO-PU/PEGDME:LiClO$_4$ at EO/Li ratio 30. The inclined lines are assigned as low frequency (LF) and depressed semi-circular arc is assigned as high frequency (HF).

The complex impedance plots show a depressed semicircle at high frequency and a saturation region at mid frequency. The high frequency response is due to the ionic conduction process in the bulk of the soft phase, which is of main interest here. This can be clearly seen in figure-2 (a) at the high frequency (HF) response, where the resistance decreases as the soft phase weight is enhanced. The low frequency dispersive region is due to accumulation of charge at the electrode-electrolyte interface. That kind of data does not comply with Kramers-Krönig relations. The latter stem from four conditions: *(i)* causality; *(ii)* linearity; *(iii)* stability; and *(iv)* finality at ω→0 and ω→∞. There is a very low frequency process that is not captured well enough in the measurement range; we have cut these data points and selected the combination of medium plus high frequency arcs for our study.

The full experimental Nyquist plots for the solid polymer electrolytes and cutting point of data are provided in the figure-1. Figure-2 is a typical Nyquist plot for the polymer electrolytes at various temperatures after cutting the low frequency region. The corresponding DFRTs are presented in figure-3. The deformation in semicircular arc is a function of composition (figure-2), temperature, salt concentrations and type of anions. ISGP found relaxation time and resistance decrease with increasing salt concentrations, with increasing amount of secondary component (soft phase), and obviously with increasing temperature. The central relaxation time and the resistance depend also on the type of salts.
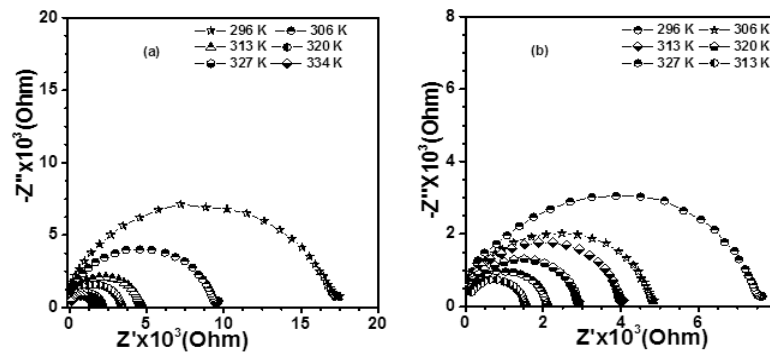
Figure-2: Typical Nyquist plots ($-Z''$ *vs* Z') for the solid polymer electrolytes as function of temperatures. **(a)** PEO-PU/PEGDME: $LiClO_4$ (60/40); and **(b)** PEO-PU/PEGD-ME: $LiClO_4$ (50/50).

The small low-frequency (high relaxation time) peak identified by ISGP after removal of the very low frequency data points, typically appears close to the edge of the new bandwidth, around $log\tau = -4$.[7] This suggests that it is a property of the analysis rather than a property of the system, and hence not much information could be extracted from it. It is, however, important to let the program find it, to improve the accuracy in finding the HF peak. The resistance values for the polymer compositions and different anions extracted from the HF peak are enlisted in table-

1. The resistance values for the polymeric compositions, salt concentrations and lithium salts of different anions are provided in figure-3.
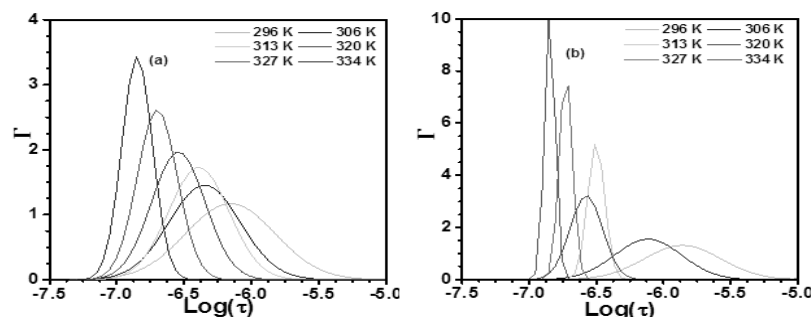
Figure-3: Normalized distribution function of relaxation times plots (Γ vs logτ) for

the polymer electrolyte compositions at different temperatures; **(a)** PEO-PU/PEGDMDE: LiClO$_4$ (60/40); and **(b)** PEO-PU/PEGDM-DE: LiClO$_4$ (50/50). Increasing temperature results with a more distributed peak that its central position moves toward a higher frequency.

The fact that the relaxation time and resistance both decrease with increasing salt concentration means that the effective capacitance (which should be proportional to the dielectric constant) does not change much with the salt concentration. The resistance changes could be due to an increase in the number of charge carrier inside the solid polymer electrolytes matrix, as well as coupling of ionic motion with polymeric Brownian motion.[8] At EO/Li>30 mole ratio, relaxation time increases due to Li$^+$ mediated transient cross linking increases inside the polymer matrix, which restrict both ionic and polymer Brownian motion. Thus from impedance spectroscopy results, the EO/Li mole ratio of 30 is found to provide best environment for ion transport towards electrode. We have further selected four polymer electrolytes compositions 60/40, 50/50, 40/60 and 30/70. From figure-4 and table-1 it is observed that increasing the amount of oligomer (secondary component) into the polyurethane matrix the relaxation times decrease. Increasing temperature results in resistance decrease and a shift to lower relaxation times. Li$^+$ cation motion, coordinating polymeric segment relative to the chain center of mass and the inter chain
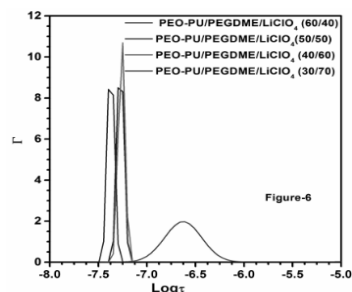
hopping rate, are all influencing Li^+ mobility inside the solid polymer electrolytes. The fact that the mean relaxation time and the resistance decrease roughly together suggests here also that the effective capacitances at the frequencies that correspond to the central position of the peak have only low dependence on temperature.

Figure-4: Normalized DFRT plots for the PEO-PU/PEGDME: $LiClO_4$ polymer electrolytes composition between primary and secondary components 60/40, 50/50, 40/60 and 30/70. At EO/Li mole ratio= 30, both the resistance, and relaxation time (τ) are at minimum.

Anions play an important role for salt solubility and polymer-salt complexation inside the polymer electrolyte matrix. The Li-cation has low polarizability due to its He-like electronic structure. The question is how the anion size affects relaxation times and resistances.[9] We have chosen four anions, presented here in decreasing size order: $-N(CF_3SO_2)_2^-$, $-ClO_4^-$, $-CF_3SO_3^-$ and $-I^-/I_3^-$. From figure-4 and table-1 it is evident that the relaxation times and resistances at fixed mole ratio (e.g., EO/Li=10) depend on anion sizes.

Table-1: EIS analyzed by ISGP – the HF peak position, normalized area and resistance for the PEO-PU/PEGDME semi-IPN solid polymer electrolyte matrix loaded with different salt concentrations, different Li-salts and polymeric compositions.

Sample name	EO/Li	Logτ	A	$R_p(\Omega)$	$R_b=A*R_p(\Omega)$
PEO-PU/PEGDME(60/40): $LiClO_4$	30	-5.8584	0.9371	17529	16426
PEO-PU/PEGDME(50/50): $LiClO_4$	30	-5.956	0.9772	7639	7464
PEO-PU/PEGDME(40/60): $LiClO_4$	30	-6.4173	0.9599	6355	6100
PEO-PU/PEGDME(30/70): $LiClO_4$	30	-7.3727	0.9330	583	543

|					
PEO-PU/PEGDME(30/70): LiI:I_2	10	-6.4854	0.9445	3534	3337
PEO-PU/PEGDME(30/70): LiN($CF_3$$SO_2)_2$	10	-6.7378	0.9792	2346	2297
PEO-PU/PEGDME(30/70): Li($CF_3$$SO_3$)	10	-6.5847	0.9363	2680	2623
PEO-PU/PEGDME(30/70): $LiClO_4$	10	-6.6274	0.9749	2880	2819
PEO-PU/PEGDME(30/70): $LiClO_4$	20	-7.2726	0.9276	771	715
PEO-PU/PEGDME(30/70): $LiClO_4$	30	-7.3727	0.9630	583	561
PEO-PU/PEGDME(30/70): $LiClO_4$	40	-7.2605	0.9592	893	856
PEO-PU/PEGDME(30/70): $LiClO_4$	60	-7.2014	0.9905	976	966
PEO-PU/PEGDME(30/70): $LiClO_4$	80	-7.0822	0.9475	1224	1159
PEO-PU/PEGDME(30/70): $LiClO_4$	100	-6.9234	1.0302	1746	1798
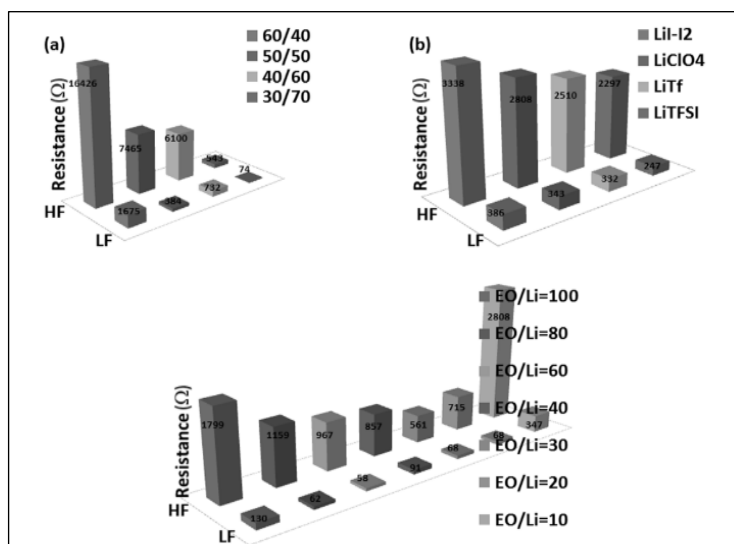
Figure-5: Resistance plot for the PEO-PU/PEG-DME: $LiClO_4$ solid polymer electrolytes as functions of **(a)** polymer compositions; **(b)** lithium salts of different anions; and **(c)** lithium perchlorate concentrations. The resistance values were calculated by the peak area multiplied by the normalization factor (ideally, the polarization resistance).

Solid polymer electrolytes that contain large size anions show low relaxation times compared to small size anions. The lattice energy of large size anion and small size cation are comparatively low, according to Fajans' rule. Low lattice energy salts are solvated easier into the semi-IPN solid polymer electrolytes. Large size anions act as hard acids and have a greater tendency to interact with hard base (ether oxygen). Watanabe and Johansson have proved that the electron withdrawing power order is $-N(CF_3SO_2)_2^- >-ClO_4^- >-CF_3SO_3^- >-I^-/I_3^-$.[10] Thus, the trend in relaxation time and resistance observed here are in accord with the anion size and ion dissociation.

Conclusions:

The effect of polymer compositions, salt concentrations, nature of anions and temperature were studied by EIS and analyzed using ISGP. The high frequency (HF) i.e. low $\log\tau$, is related to the ionic motion inside the solid

polymer electrolyte matrix. Impedance spectroscopy genetic programming show that the polymer composition PEO-PU/PEG-DME: LiClO$_4$ (30/70) provides the lowest relaxation times (logτ) and minimum resistance values. The effect of anion size on the resistance and relaxation times of solid polymer electrolyte matrix follows similar order as lattice energy of lithium salts. The relaxation times and resistance order is LiN(CF$_3$SO$_2$)$_2$>LiClO$_4$>LiCF$_3$SO$_3$>LiI/I$_3$. The results of ISGP are in good agreement with observed ionic conductivities.

References:

1. Fenton, D. E.; Parker, J. M.; Wright, P. V.; Polymer,1973, 14, 589-589.
2. Wright, P. V.; Br. Polym. J, 1975, 7, 319-327.
3. Mahendran, O.; Rajendran, S.; Ionics, 2003, 9, 282-288.
4. Barbosa, P. C.; Rodrigues, L. C.; M. M. Silva.; M. J. Smith.; A. J. Parola.; F. Pina.; C, Pinheiro.; Electrochimica Acta, 2010, 55, 1495-1502.
5. Zhu, Y., et al.; Energy Environ. Sci. 2013, 6, 618–624.
6. Ganapatibhotla L. V. N. R.; Maranas J. K.; Macromolecules, 2014, 47, 3625–3634
7. Boukamp, B. A.; Application and Limitations Electrochimica Acta 2015,154, 35-46.
8. Hershkovitz, S.; Tsur Y.; Baltianski, S.; Solid State Ionics, 2011, 188, 104-109.
9. A. B. Tesler.; D. R. Lewin.; S. Baltianski.; Y. Tsur.; J. Electroceram, 2010, 24, 245.
10. Ratner, M. A.; Shriver, D. F. Ion Transport in Solvent-free Polymers. Chem. Rev, 1988, 88, 109-124.

CHAPTER 5

Neutron Star: An Astrophysical Laboratory for the Study of Extreme Matter Physics

✎ *Dr. Partha Roy Chowdhury*

Department of Physics, Chandrakona Vidyasagar Mahavidyalaya, Paschim Medinipur, West Bengal -721201, India.

E-mail: royc.partha@gmail.com

1. Introduction:

Neutron stars (NSs) are the densest objects observed in the Universe and they contain compressed baryonic matter permanently in their centers. As such, NSs are valuable laboratories for the study of dense matter. They are so compact that general relativity is essential to their structures; indeed, the existence of a maximum neutron star mass[1-5] is a manifestation of general relativity. The vast majority of neutron stars are observed as pulsars and nearly 2000 have been detected.

(for pulsar databases see the website
http://www.atnf.csiro.au/research/pulsar/psrcat).

Currently, however, only a few aspects of neutron stars can be inferred from pulsar observations, such as masses, spin rates, rough ages, and magnetic field strengths etc. Experimentally, the properties of compressed baryonic matter are being probed with the Relativistic Heavy Ion Collider (RHIC at Brookhaven) and the Large Hadron Collider (LHC at CERN). Great advances in our understanding of such matter are expected from the next generation of heavy-ion collision experiments at Facility for Antiproton and Ion Research (FAIR at GSI) and Nuclotron bases Ion Collider fAcility (NICA) at JINR.[6]

Neutron stars are remnants of massive stars that blew apart in core-collapse supernova explosions. They are typically about 20 km across and

spin rapidly, often making many hundred rotations per second. Many neutron stars form radio pulsars, emitting radio waves that appear from the Earth to pulse on and off like a lighthouse beacon as the star rotates at very high speeds. Neutron stars in X-ray binaries accrete material from a companion star and flare to life with tremendous bursts of X-rays.

Depending on mass and rotational frequency, gravity compresses the matter in the cores of neutron stars to densities that are several times higher than the density of ordinary atomic nuclei. At such huge densities atoms themselves collapse and atomic nuclei are squeezed so tightly together that new fundamental particles may be produced and novel states of matter are created. The most spectacular phenomena stretch from the generation of hyperons and delta particles, to the formation of meson condensates, to the

formation of plasma of deconfined quarks (Figure 1).
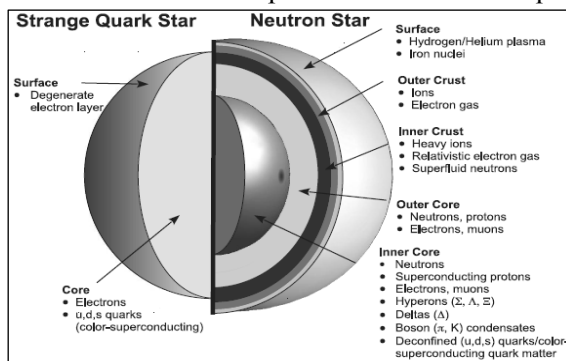
Figure: 1 Comparison of structures between quark stars (left) and neutron stars (right)[6,7]

I present here a brief review on the physics of neutron stars and its properties with special attention to nuclear equation of state (EoS) and neutron star masses. The pressure p and total energy density (including mass) are related by the EoS of neutron star matter in either form: $p = p(\ )$ or $\ = \ (p)$. The recent works on this topic by the leading researchers will also be discussed in next sections. Finally, my research works over last ten years on the prediction of the maximum possible NS mass will be briefly described for the students interested to work in this field in near future.

2. Creation of Neutron Star

A year following Chadwick's 1932 discovery of the neutron, Baade and Zwicky *conceived the notion of neutron stars*[7] in the course of their

investigation of supernovae. A supernova (SN) is a large explosion that takes place at the end of a massive supergiant star's life cycle. It may shine with the brightness of a ten billion suns! The total energy output may be 10^{44} joules, as such as the total output of the sun during its 10 billion years lifetime. The most recent directly observed supernova in the Milky Way Galaxy was Kepler's Star of 1604 (*SN 1604*). Supernovae create, fuse and eject the bulk of the chemical elements produced by nucleosynthesis. They play a significant role in enriching the interstellar medium with higher mass elements. The expanding shock waves from SN explosions can trigger the formation of new stars. SN can be triggered either by sudden re-ignition of nuclear fusion in a degenerate star or by the sudden gravitational collapse of the massive star's core. Neutron stars are created in the aftermath of the gravitational collapse of the core of a massive star ($M_{star} > 8M_\odot$ where $M_\odot$ is one solar mass) at the end of its life, which triggers a Type II supernova explosion. If supernova's spectrum contains lines of hydrogen known as the Balmer series in the visual portion of the spectrum, it is classified Type II SN, otherwise Type I.

Newly-born neutron stars or proto-neutron stars are rich in leptons, mostly e^- and ν_e (Figure 2). The detailed explosion mechanism of Type II supernovae is not understood,[8] but it is probable that neutrinos play a crucial role. Toward the end of the 20th century astronomers increasingly turned to computer controlled telescope and CCDs for hunting supernovae.

The gravitational binding energy released in the collapse of the progenitor star's white dwarf-like core to a neutron star is about $3GM^2/5R \simeq 3 \times 10^{53}$ erg (G is the gravitational constant), which is about 10% of its total mass energy Mc^2. Nearly all the energy is carried off by neutrinos and antineutrinos of all flavors in roughly equal proportions. The gravitational energy per nucleon in the star can be estimated (~157 MeV/A) and compared to the nuclear binding energy per nucleon in nuclear matter (~16MeV/A) and in a finite nucleus (~8MeV/A). Thus, the weakest force i.e. *gravitational force* binds nucleons in a neutron star 10 times more strongly than the strong force e.g. *nuclear interaction* binds them in nuclei.

Core collapse halts when the star's interior density reaches n_0, which triggers the formation of a shock wave at the core's outer edge. The shock

wave propagates only about 100 to 200 km before it stalls, having lost energy to neutrinos and from nuclear dissociation of the material it has plowed through [stage (I) in Figure 2].

The proto-neutron star left behind rapidly shrinks because of pressure losses from neutrino emission in its periphery (stage II). The escape of neutrinos from the interior occurs on a diffusion time $\simeq 3R^2/$ c ≈ 10 s. The neutrinos observed from Supernova (SN) 1987A in the Large Magellanic Cloud confirmed this time scale and the overall energy release of $\simeq 3 \times 10^{53}$ ergs.[8,9] The loss of neutrinos (which forces electrons and protons to combine, making the matter more neutron-rich) initially warms the stellar interior. The core temperature is more than doubles (stage III), reaching ~ 50 MeV (6×10^{11} K and 1MeV$\sim 10^{10}$K). After 10 to 20 s, however, the steady emission of neutrinos begins to cool the interior. The star becomes transparent to neutrinos (stage IV), and its cooling rate accelerates.
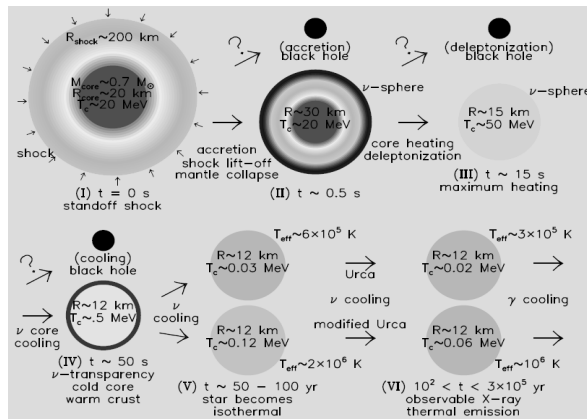
Figure: 2 Six main stages (I-VI) of evolution of a neutron star with t=0s, 0.5s, 15s, 50s, 50-100 yr and more than 100 yrs. In each stage the radius R and central temperatures T_c for the neutron star are indicated.[9]

Neutron stars have both minimum and maximum mass limits. The **maximum mass**, which is of purely general relativistic origin, is unknown, but lies in the range of **1.44 to 3 M⊙**. The upper bound follows from causality, that the speed of sound in dense matter is less than the speed of light, whereas the **lower bound** is the largest

accurately measured pulsar mass, **1.4408 ± 0.0003 M$_\odot$**, in the binary pulsar PSR 1913+16. Astrophysicists set a new limit[3-5] for the maximum mass of NS. The **upper bound of maximum mass** can not exceed **2.16 M$_\odot$** according to a recent work at FIAS Frankfurt, Germany using GW observations and Quasi-Universal relation based on kilonova modelling.[4]

3. Present Work: Search for a Suitable Realistic EoS and Determination of Mass of Neutron Star

A systematic study of the properties of pure hadronic and hybrid compact stars shall be presented in the following. The nuclear EoS for β-equilibrated neutron star (NS) matter obtained using a density-dependent effective nucleon-nucleon DDM3Y interaction satisfies the constraints from the observed flow data from heavy-ion collisions. The incompressibility K for the symmetric nuclear matter (SNM), nuclear symmetry energy $E_{sym}(\rho_0)$ at saturation density ρ_0, the isospin dependent part K_τ of the isobaric incompressibility and the slope L are all in excellent agreement with the experimental and observational data.

Depending on the model, the energy density of quark matter can be lower than that of this nuclear EoS at higher densities, implying the possibility of transition to quark matter inside the core and the transition density depends on the particular quark matter model used. We solve the Einstein field equations for rotating stars using pure nuclear matter and quark core. The β-equilibrated neutron star matter, along with different EoS's for crust, is able to describe highly massive compact stars but finds that the nuclear to quark matter deconfinement transition inside neutron stars causes reduction in their masses.

There is also the theoretical possibility that quark matter made of up, down and strange quarks (so-called strange quark matter) may be more stable than ordinary nuclear matter. This so-called strange matter hypothesis constitutes one of the most startling possibilities regarding the behavior of superdense matter, which, if true, would have implications of fundamental importance for cosmology, the early universe, its evolution to the present day and astrophysical compact objects such as neutron stars and white

dwarfs. The properties of compact stars made of strange quark matter, referred to as strange (quark) stars, are compared with those of neutron stars in Fig. 1. Even after three decades of research, there is no sound scientific basis on which one can either confirm or reject the strange quark matter hypothesis so that it remains a serious possibility of fundamental significance for various astrophysical phenomena.

4. Compact Stars with and without Quark:

If rapidly rotating compact stars were nonaxisymmetric, they would emit gravitational waves in a very short time scale and settle down to axisymmetric configurations. Therefore, we need to solve for rotating and axisymmetric configurations in the framework of general relativity. For the matter and the spacetime the following assumptions are made. The matter distribution and the spacetime are axisymmetric, the matter and the spacetime are in a stationary state, the matter has no meridional motions, the only motion of the matter is a circular one that is represented by the angular velocity, the angular velocity is constant as seen by a distant observer at rest and the matter can be described as a perfect fluid. The energy-momentum tensor of a perfect fluid $T^{\mu\nu}$ is given by

$$T^{\mu\nu} = (\varepsilon + P)\, u^{\mu}u^{\nu} - g^{\mu\nu}\, P \qquad ...(1)$$

where ε, P, u^{μ} and $g^{\mu\nu}$ are the energy density, pressure, four velocity and the metric tensor, respectively. To study the rotating stars the following metric is used

$$ds^2 = -e^{(\gamma+\rho)}\, dt^2 + e^{2\alpha}\, (dr^2 + r^2 d\theta^2) + e^{(\gamma-\rho)}\, r^2 \sin^2\theta\, (d\varphi - \omega dt)^2 \qquad ...(2)$$

where the gravitational potentials γ, ρ, α and ω are functions of polar coordinates r and θ only. The Einstein's field equations for the three potentials γ, ρ and α have been solved using the Green's-function technique and the fourth potential ω has been determined from other potentials. All the physical quantities may then be determined from these potentials. Obviously, at the zero frequency limit corresponding to the static solutions of the Einstein's field equations for spheres of fluid, the present formalism yields

the results for the solution of the Tolman-Oppenheimer-Volkoff (TOV) equation. We use the 'rns' code[10] for calculating the compact star properties which requires EoS in the form of energy density versus pressure (ε vs. P) along with corresponding enthalpy and baryon number density and since we are using various EoS for different regions, these are smoothly joined.

5. Methodology:

The nuclear matter EoS is calculated[11] using the isoscalar and the isovector components of M3Y interaction along with density dependence. The density dependence of the effective interaction, DDM3Y, is completely determined from nuclear matter calculations. The equilibrium density of the nuclear matter is determined by minimizing the energy per nucleon (ϵ =E/A). In a Fermi gas model of interacting neutrons and protons, the ϵ for isospin asymmetric nuclear matter is the sum of the kinetic part and nuclear potential part calculated using the volume integral of the isoscalar and isovector components of M3Y interaction. The details of the present methodology may be obtained in Ref. 11.

We numerically determine the EoS for the   -equilibrated charge neutral neutron star matter in which the   -equilibrated proton fraction is determined from the knowledge of the symmetry energy. Then this nucleonic EoS with thin crust is used to solve the Einstein's field equations by Green's function technique to determine the mass-radius relationship of neutron stars with and without quark cores. The calculations for rotating and static compact stars without quark core are performed using the crustal EoS for thin crust upto number density of $\rho \sim 0.05$ fm^{-3} or, density $\xi \approx 7.7 \times 10^{13}$ g/cm^3 =0.31ξ_0 (nuclear saturation density ξ_0=2.5x10^{14} g/cm^3) and   - equilibrated NS matter for stellar core up to $\rho \approx 1.4$ fm^{-3} or equivalently up to $\xi \approx 3.5 \times 10^{15}$ g/cm^3 =14ξ_0.
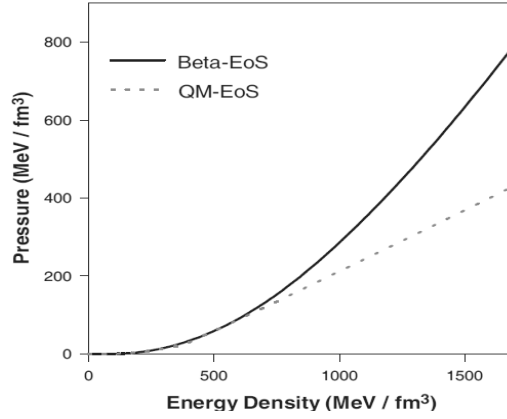
Figure-3: Pressure versus energy density (P vs. ε) plots of β-equilibrated charge neutral neutron star matter and quark matter.

6. Result and Discussion:

The energy density of the quark matter[12] is lower than that of the present EoS for the -equilibrated charge neutral NS matter at densities higher than 0.405 fm^{-3} for bag constant $B^{1/4} = 110MeV$ [13] implying the presence of quark core. So we employ the crust EoS up to $\rho \approx 0.05$ fm^{-3}, the nucleonic EoS up to $\rho \approx 0.4$ fm^{-3} or $\xi \approx 7x10^{14}$ $g/cm^3 = 2.8\xi_0$ and finally quark EoS [12] up to $\rho \approx 1.37$ fm^{-3} or $\xi \approx 3x10^{15}$ $g/cm^3 = 12$ ξ_0 for the calculations of masses and radii for rotating and static neutron star with both nucleons and quark matter inside. The pressures of the present EoS for the -equilibrated charge neutral NS matter and the quark matter EoS for bag constant $B^{1/4} = 110MeV$ are shown in fig.3 as functions of energy densities.
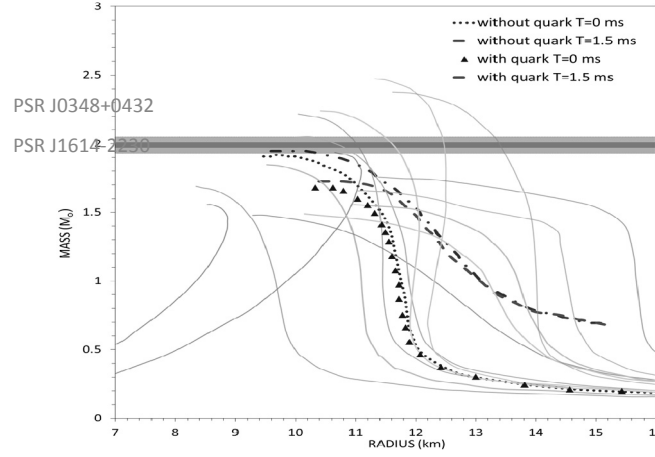
Figure-4: Mass-Radius relationship for static (T=0 ms) and rotating (T=1.5 ms) neutron stars with and without presence of quark matter inside the core.

The results of the calculations for stars with pure nucleonic core [14] without quark and hybrid stars with mixture of quark and nucleons in the stellar core are shown in fig.4. It is clear from fig.4 that NSs with pure nuclear matter inside, the maximum mass for the static case (i.e. time period T~0 ms) is $1.92M_\odot$ with radius ~ 9.7 km and for the star rotating with maximum frequency $\nu\sim 667$ Hz (i.e. time period T~1.5 ms) limited by the r-mode instability, the maximum mass turns out to be $1.95M_\odot$ with radius about 9.9 kilometers. However, the maximum masses for hybrid neutron star with quark core are significantly reduced for both static and rotating stars. The maximum mass of static hybrid star is only $1.68M_\odot$ with radius about 10.4 km. The maximum mass is increased to $1.72M_\odot$ with radius about 10.7 km for the hybrid star rotating with time period T~1.5 ms.

It is obvious from the fig.4 that the presence of quarks as constituents of stellar core significantly affects the mass-radius relationship for massive stars with smaller radii. The stars with relatively lower masses and higher radii are almost unaffected by its constituents. On the contrary, the effect of rotation becomes more prominent in lower mass region of the curves presenting the mass-radius relationship for the neutron stars with and without quark.

7. Summary:

Exploring the properties of compressed baryonic matter, or, more generally, strongly interacting matter at high densities and/or temperatures, has become a forefront area of modern physics. The recent observations of the binary millisecond pulsar J1614-2230 by P.B. Demorest et al.[1] and PSR J0348+0432 by J. Antoniadis et al.[2] suggest that the masses lie within 1.97 ± 0.04 M$_\odot$ and 2.01 ± 0.04 M$_\odot$, respectively, where M$_\odot$ is the solar mass. Recently Astrophysicists set a new limit 2.16 M$_\odot$ for maximum mass of NS.[4] In conformity with recent observations, a pure nucleonic EoS determines that the maximum mass of NS rotating with frequency $\nu \sim 667$ Hz below r-mode instability is ~ 1.95 M$_\odot$ with radius ~ 10 km. However, the maximum mass of NS with quark cores rotating with the maximum frequency limited by the r-mode instability i.e. $\nu \sim 667$ Hz, reduces to ~ 1.72 M$_\odot$ only. The observational, experimental and theoretical constraints of dense matter altogether will reveal many exotic properties of neutron star with new physics in future.

References:

1. P. B. Demorest, T. Pennucci, S. M. Ransom, M. S. E. Roberts, J. W. T. Hessels, Nature 2010, 467, 1081.
2. J. Antoniadis et al; Science 2013, 340, 1233232; arxiv:1605:01665v1 (Draft Version)
3. Emmanuel Fonseca et al. "The NANOGRAV Nine Year Data Set: Mass and Geometric Measurement of Binary Millisecond Pulsars (MSP)", The Astrophysical Journal 2016, 832, 167.
4. Luciano Rezzolla, E.R.Most, Lukas R.Weih, Astrophysical Journal Letters 2018, 852, L25.
5. Justin Alsing, Hector Silva, Emanuele Berti "Evidence for a max.mass cut-off in neutron star mass distribution…. EoS", Monthly Notices of the Royal Astronomical Society 2018, 478, 1377-1391.
6. T. Klahn, D. Blaschke and F. Weber, Phys. Part. Nucl. Lett. 2012, 9, 484; http://nica.jinr.ru/files/WhitePaper.pdf.
7. (a) M. G. Alford, A. Schmitt, K. Rajagopal and T. Schafer, Rev. Mod. Phys. 2008, 13, 1455; (b) F. Weber, Pulsars as Astrophysical Laboratories for Nuclear and Particle Physics (IOP, 1999).
8. For a review, see A. Burrows, Nature 2000, 403, 727.
9. Lattimer JM, Prakash M. Ap. J. 550:426 (2001); Phys. Rev. Lett.

94:111101 (2005); Phys. Rep. 2007, 442, 109.

10. N. Stergioulas, J.L. Friedman, Astrophys. J. 1995, 444, 306.
11. Partha Roy Chowdhury et al; Phys. Rev. C 81, 2010, 062801(R).
12. A. Kurkela, P. Romatschke, A. Vuorinen, Phys. Rev. D 81, 2010, 105021.
13. A. Chodos, R. L. Jaffe, K. Johnson and C. B. Thorn, Phys. Rev. D 10, 1974, 2599.
14. Partha Roy Chowdhury, "Nuclear matter for compact stars and its properties", PoS (NIC XI) 175 (2010) (Proceedings of International Symposium NIC XI, Heidelberg, Germany, 19-23 July, 2010).

CHAPTER 6

Search for Superheavy Elements in the Magic Island of Stability

✎ *Dr. Mukesh Kumar Pradhan*

Assistant Professor, Department of Physics, Belda College, Belda, Paschim Medinipur, W. B.-721424, India

E-mail: mkpradhan81@gmail.com

Introduction:

Superheavy elements (SHE) are those elements with a large number of protons in their nucleus. Elements with more than 92 protons are unstable; they decay to lighter nuclei with a characteristic half-life. This means superheavy elements do not occur in large quantities naturally on earth, and only exist briefly under highly controlled circumstances. Nuclear reactions[1, 2] play an essential role to produce various new nuclei including exotic nuclei and SHE in laboratory environment which are not found in nature. The experiments on fusion reactions of light to light nuclei, light to heavy nuclei, and heavy to heavy nuclei have been performed in laboratory to explore the structure and various properties of nuclei.

The fusion[1- 5] between the heavy target nuclei and heavy projectile nuclei is of particular interest for last few decades. The heaviest of the transuranic elements known as superheavy elements are produced in nuclear reactions in a few specialized laboratories located in Russia, Germany, U.S.A and Japan. Beyond uranium the periodic table includes no less than 26 elements which have all been manufactured in the laboratory and the best known of which is plutonium of atomic number 94. The superheavy elements (SHE) often refers to the transactinide elements with Z ranging from 103 to 120. In some cases the term is used only for Z > 110. So far the **last of the superheavy elements is Z = 118**, a substance which received official recognition as an element in 2016. Russian physicist Yuri Oganessian of the Joint Institute for

Nuclear Research (JINR) in Dubna has contributed so much to the periodic table by artificially preparing many superheavy nuclei in lab that element 118 is named after him ***Oganesson*** with chemical symbol **Og**. Superheavy Element Factory (SHEF) in Dubna, Russia, aims to create new elements that extend the periodic table by colliding a beam of nuclei with a target (see Fig.1). In late 2015, the International Union of Pure and Applied Chemistry (IUPAC) officially confirmed elements 113, 115, 117, and 118. The new elements also received their final names: Nihonium (Z=113), Moscovium (Z=115), Tennessine (Z=117), and Oganesson (Z=118). Efforts to find the next elements, 119 and 120, are underway.

By bombarding heavy nuclei with ion beams of lighter nuclei, scientists create superheavy nuclei that are so unstable that they split apart, oftentimes only a tiny fraction of a second after they are created. When making new superheavy elements, scientists are engaged in a battle against the fundaments of nature. In elements with low atomic weight, protons and neutrons stick together because the strong nuclear force pulls them together. But when more and more protons are packed into a nucleus, the strong nuclear force starts to lose out to another force, the Coulomb force. This force causes particles of the same charge to push each other apart. Most superheavy nuclei undergo nuclear fission within milliseconds, splintering into lighter elements, or they spit out a few alpha particles ($^4_2$) made of two protons and two neutrons—at first and then split apart.

The formation of superheavy nuclei (SHN) by fusion was intensively explored.[3-5] The investigation of experimental data concerning fusion and fission of the SHN with Z = 108-118 together with data on survival probability of these nuclei in evaporation channels with 3-4 neutrons, revealed the fact that the hindrance due to high fission barriers causes to a relatively higher stability of such heavy nuclear systems. The investigation of α-decay chains of such SHN is the main tool to extract some information regarding their degree of stability and possible existence in nature. In the last decade several theoretical and experimental works[4-8] were devoted to the formation of SHN and their α-decay half-lives. The α decay of superheavy nuclei is possible if the shell effect supplies the extra binding energy and increases the barrier height of fission.

Earlier, it was believed that traditional spherical superheavy nuclei might form a "magical island of stability" centered around $^{298}114_{184}$ separated from the "peninsula" of known nuclei by a region of deep instability. Due to both deformed neutron shell and proton shell effects at Z=108 and N=162 the extension of the peninsula of known nuclei might connect the stability island of spherical superheavy nuclei around doubly magic spherical Z=114 proton shell and spherical N=184 neutron shell. Since fission barrier and shell effect play very important role for the existence of long lived superheavy nuclei it is crucial to determine the fission barrier and half-life of fissioning nucleus with a good accuracy. It is well known that very small barrier height against fission can break the nucleus into two fragments immediately after it is formed. The α decay of superheavy nuclei is possible if the shell effect supplies the extra binding energy and increases the barrier height of fission. β-stable nuclei having relatively longer half life for spontaneous fission than that for α decay indicates that dominant decay mode for such SHN might be α-decay. This work explores the possibility of finding long lived superheavy nuclei (SHN) by comparing the calculated α decay half lives (T_α) with available theoretical spontaneous fission (SF) half lives,[9] calculated β-decay half-lives (T_β)[10] and the experimental data on SF. The α decay half lives of SHN with Z=102-120 are calculated in a quantum tunneling model with DDM3Y effective nuclear interaction using Q_α values from three different mass formulae.[11-13]

FORMALISM

The α decay half lives are calculated in the frame work of quantum mechanical tunneling of an α particle from a parent nucleus. The details of calculation of the α decay half lives of superheavy nuclei can be found in papers published by P. Roy Chowdhury *et.al.*[6-8] The required nuclear interaction potentials are calculated by double folding the density distribution functions of the α particle and the daughter nucleus with density dependent M3Y effective interaction. The half lives of α disintegration processes are calculated using the WKB approximation for barrier penetrability. Spherical charge distributions have been used for calculating the Coulomb interaction potentials. Most of the experimental Q-values of α decay (Q) are obtained from experiments done in GSI, Germany and JINR, Dubna. For theoretical Q-values, mass formulae from KUTY,[11] Myers-Swiatecki (MS)[12] and Muntian et.al.(MMM)[13] are used.

RESULTS AND DISCUSSION

In this short review, our main aim is to check whether the predicted SHN do really survive against the spontaneous fission (SF). Gamow-Teller β-decay half lives (T) obtained from a microscopic quasi-particle random phase approximation with single particle levels by Moller, Nix, Kratz [10] has also been used in this work to check the possibility of β-decay of SHN.

In Fig.1 the theoretical Q-values from different mass formulae prescribed by KUTY,[11] Myers-Swiatecki (MS) [12] and Muntian et.al.(MMM) [13] are employed to calculate α-decay half-lives of sixteen SHN. The measured Q-values are used to calculate α decay half lives ($T_{1/2}^{DDM3Y}$ $[Q_{ex}]$).[14] Half lives calculated in the present work agree reasonably well with experimental data [3-5, 14] for most of the superheavies. In this work, existing SF calculation with a microscopic approach have been used to find the region of long lived fission survived nuclei in the SHN region of the nuclear chart.

From the present calculation of T using Q_{KUTY} it seems that longer T might be observed for more neutron rich side (Z ≥116, N>190) due to possible existence of neutron shell closure. On the contrary, from the trend of SF plots for Z=116, 118, 120 it appears that lowering of T_{SF} might destroy the existence of such neutron rich (N > 190) superheavy isotopes of elements Z=116, 118 and 120. Hence, the presence of long-lived SHN with neutron shell closure beyond N=184 may be ruled out. However, it is an important task to determine the SF and α decay half lives for N > 184 to confirm whether there is any possibility of neutron shell closure beyond N=184 for heaviest elements (Z ≥116).

It may be pointed out that the calculation of T is very sensitive to Q -values, and none of the mass formula used here cover the entire mass range with extreme accuracy. Therefore, a better mass estimate covering the wide range of superheavy masses with a good accuracy is necessary.
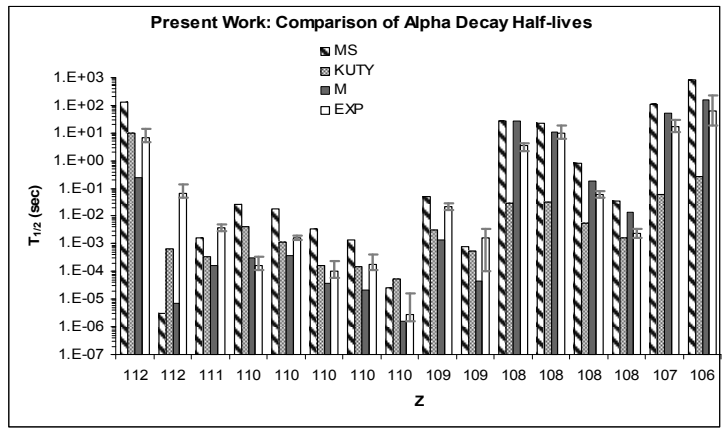
Figure-1: Comparisons between observed [3-5] and theoretical (this work) α-decay half-lives using measured Q_α.[14]
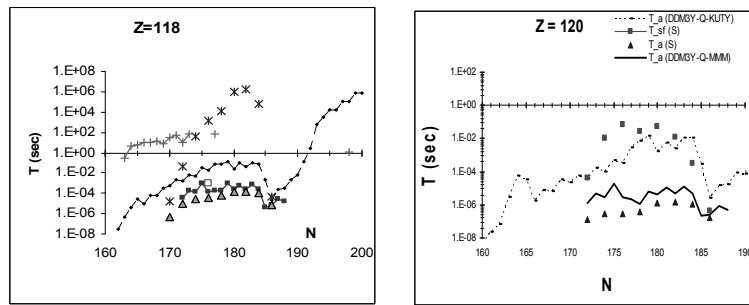

Figure-2: Variation of α decay and fission half-lives with neutron number for elements Z=118 and Z=120

With increase of the charge of a nucleus, relativistic effects may come into play as electrons gain velocity and come closer to the speed of light. The classical theory which was used to construct the periodic table, did not take the relativistic effect into account. There may come a point where relativistic effects are so pronounced that elements no longer follow the trends of their period. If we follow the periodicity, the last superheavy element Z=118 (Og) should occupy one position (Period: 7, Group: 18) in the group of noble or inert gases just below Radon (Z=86)

in the periodic table. So we may expect the superheavy element Oganesson (Z=118) as inert gas. According to Yuri Oganessian, if it is not inert, if it is reactive, then it's already happened: Z=118 is the end of periodicity!
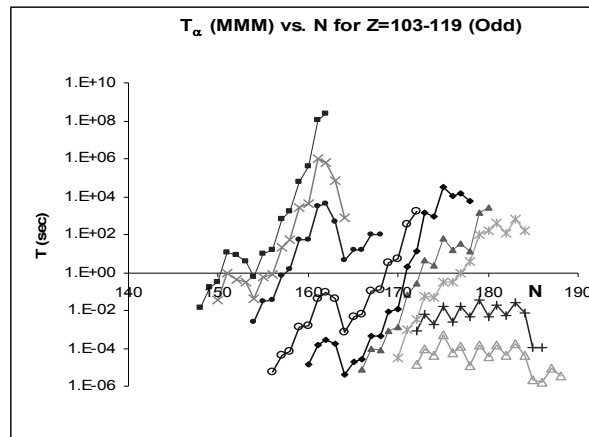

Figure-3: Variation of α decay half-lives (Tα) predicted by present calculation with neutron number for odd-Z elements from Z=103-119.
From our calculation we have the following findings:

- The possibility of existence of SHN above Z=114 with considerable life time is very low.

- Although Z=120, 124, 126 with N=184 might form spherical-doubly-magic nuclei and survive fission, they would undergo α-decay within microseconds.

- A small peninsula might survive fission & undergo α-decay in the region Z=106-108, N~160-164.

- $^{268}Sg_{162}$ has the highest α-decay half life ~3.2hrs (t ~ 1.7 hrs) that is much greater than the recently discovered deformed doubly magic SHN ^{270}Hs (Expt-T ~ 22 sec).

- $^{293}Ds_{183}$ appears to be near the center of a possible "**magic island**" **(Z=104-116, N ~ 176-186)** with alpha decay half life ~352 yrs

which is much greater than that of the doubly magic SHN Z=114, N=184 (T ~17days).

- Lifetime of $^{290}Sg_{184}$(t~few million yrs) is found to be longest but still 3 order of magnitude less than the age of earth (~ 4.5 billion yrs).

- But, for both $^{293}Ds_{183}$ and $^{290}Sg_{184}$ nuclei, b-decay might be another possible decay mode with large T value.

- Both theoretical and experimental works need to be done on beta decay half lives of SHE.

Summary and Conclusion:

In summary, we find that the possibility of existence of SHN above Z= 114 with considerable life time is very low. Although Z=120, 124, 126 with N=184 might form spherical-doubly-magic nuclei and survive fission, they would undergo α decay within microseconds. A small "island/peninsula" might survive fission and βdecay but undergo α decay in the region Z=106-108, N ~ 160-164. Interestingly, in this region the β-stable SHN Z=106, N=162 has the highest α decay half life ~ 3.2hrs that is much greater than the recently discovered deformed-doubly-magic SHN 270Hs (measured T_α ~ 22 s). Thus a search for this long-lived SHN $^{268}Sg_{162}$ can be pursued. Similarly, the nucleus with Z=110, N=183 appears to be near the center of a possible "magic island" (Z=104-116, N ~ 176-186) with α decay half life ~ 352yrs (Fig. 3, using Q KUTY) which is greater than that of the doubly-magic SHN Z=114, N=184 (T_α ~ 17days). Only future experiments can confirm this. Finally, the experimental investigations to detect the α-cascade can be pursued on $^{294}110_{184}$, $^{293}110_{183}$, $^{296}112_{184}$ and $^{298}114_{184}$ nuclei which are expected to decay predominantly through α particle emission.

Acknowledgements

References:

1. M. K. Pradhan et al. Physical Review C 83, 2011, 064606.
2. M. K. Pradhan et al. Physical Review C 88, 2013, 064603.
3. Yu. Ts. Oganessian et al. "Synthesis of the isotopes of elements 118 and 116 in the ^{249}Cf and ^{245}Cm + ^{48}Ca fusion reactions" Physical Review C 74, 2006, 044602.
4. Yu. Ts. Oganessian et al. "Synthesis of a new element with At. No. Z= 117" Physical Review Letter 2010, 104, 142502.
5. Yu. Ts. Oganessian & V.K. Utyonkov, "Superheavy nuclei from ^{48}Ca-induced reactions" Nuclear Physics A 2015, 944, 62-98.
6. P. Roy Chowdhury et al. Physical Review C 2006, 73, 014612.
7. P. Roy Chowdhury et al. Physical Review C 2011, 83, 027601.
8. P. Roy Chowdhury et al. Atomic Data and Nuclear Data Tables 2008, 94, 781-806.
9. R. Smolanczuk, Phys. Rev. C 1997, 56, 812.
10. P. Moller, J. R. Nix, and K.-L. Kratz, Atomic Data Nuclear Data Tables 1997, 66, 131.
11. H. Koura, M. Uno, T. Tachibana, and M. Yamada (KUTY), Nucl.Phys. A 2000, 674, 47.
12. W. D. Myers and W.J. Swiatecki, Nucl. Phys. A 1996, 601, 141.
13. I. Muntian, S. Hofmann, Z. Patyk and A. Sobiczewski, Acta Phys. Pol. B 2003, 34, 2073.
14. M. Gupta and Thomas W. Burrows, Nuclear Data Sheets 2005, 106, 251.

CHAPTER 7

Copper Catalyzed Synthesis of Pyrrole Derivatives: An Overview

✍ *Dr. Sukla Nandi*

Department of Chemistry, Chandrakona Vidyasagar Mahavidyalaya, Paschim Medinipur, West Bengal-721201, India.

E-mail: suklanandi@chandrakonavm.ac.in

Introduction:

The electron rich, and aromatic heterocycles pyrrole has a wide range of applications in pharmaceuticals, the agrochemical industry and organic synthesis. Extensive studies on the chemical behaviours of pyrrole continued throughout the 20th century and numerous protocols have been established for the efficient synthesis of pyrrole and its derivatives, amongst which reactions using transition metal-based catalyst/mono- or bidentate ligand systems play an important role as they involve milder reaction conditions, affording excellent yields of the products. Among these methods, the main share lies in copper catalysis. In particular, substituted pyrroles are highly biologically active and have proven to display antibacterial,[1] antiviral (also anti-HIV-1),[2] antiinflammatory,[3] and antioxidant[4] activities and inhibit cytokine-mediated diseases.[5] In this review, we focus on the copper-catalyzed C–N cross-coupling reactions of various aryl electrophiles with a range of nucleophilic pyrroles under various reaction conditions. This pyrrole framework is an integral part of the structure of some biologically active compounds as well as occurring in natural products.[6] Some of these are ningalins (**1**), lamellarins (**2**) and storniamides (**3**, Figure-1), these are isolated from various marine organisms, and some of these show considerable potential for the treatment of various cancers and HIV-AIDS.[7] The heterocyclic core of benzo[*f*]isoindole-4,9-diones is found in natural products such as *Reniera* indole (**4**), Bhimamycin C (**5**) and Bhimamycin D (**6**) display bioactivities against human ovarian cancer cell lines, are EP4

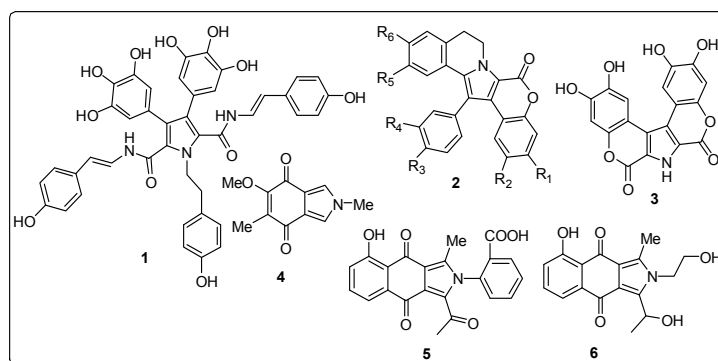receptor agonists in the treatment of pain, and are inhibitors of HIV-1 integrase.[8]

**Figure-1:** Natural products containing pyrrole moieties

Literature survey for the synthesis of pyrrole derivatives using copper catalyst:

Among the various synthetic procedures transition metal-catalyzed methods are both selective and economical for formation of pyrrole structures. In which copper plays an important role. Gevorgyan *et al.* reported (J. Am. Chem. Soc., 2001) copper(I) catalyzed cyclization of alkynyl imines to form pyrrole (Scheme-1).
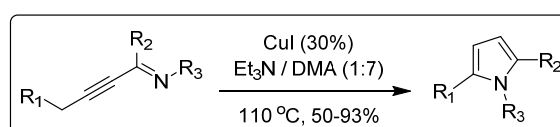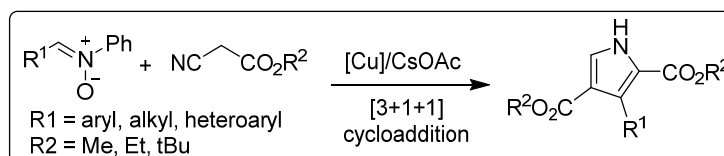

Scheme-1

Sakai et al. describe how copper (II) chloride efficiently catalyzes the [4+1] annulation of propargylamines with either ethyl glyoxylate or phenylglyoxal functioning as a C1 unit, in the presence of piperidine (Scheme-2), which leads to a straightforward and one-pot preparation of pyrrole derivatives (Tetrahedron Letters, 2016).
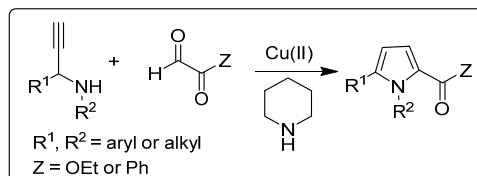
Scheme-2

An expedient synthesis of pharmacologically interesting poly-substituted pyrroles from easily available nitrones and α-acidic isocyanides using copper-catalyzed [3+1+1] cyclo-addition reaction was developed by Tan and Xu et al. in 2018 (Scheme-3).

Scheme-3

Sajiki and Sawama et al. have reported (Green Chemistry, 2018) an effective synthesis of highly-substituted pyrroles from 3,6-dihydro-1,2-oxazines using a heterogeneous copper on carbon (Cu/C) under neat heating conditions (Scheme-4).
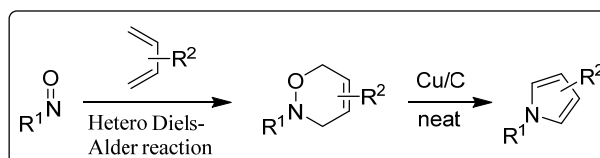
Scheme-4

Highly functionalized synthesis of pyrroles from allenoates using copper catalysts (Scheme-5) was discovered by Snieckus and Allais et al. (Synlett, 2020).

Scheme-5

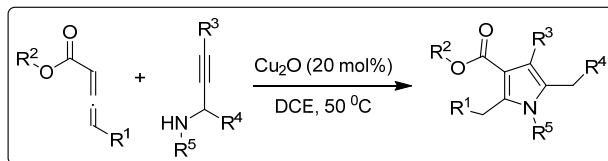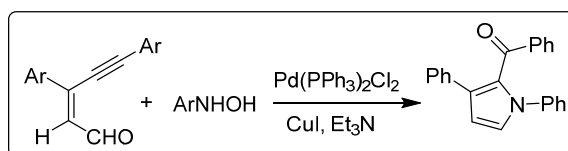We have also developed[9] a new methodology for the synthesis of highly substituted pyrrole rings by reaction of substituted 3-(1-alkynyl)-2-alkene-1-als with arylhydroxyl-amines under Cu(I) catalysis. This reaction is helpful for the synthesis of some quinones bearing annelated N-heterocyclic natural products (Scheme-6).

Scheme-6

Results and Discussion:

The convergent approach involved the preparation of the precursors **8** which were efficiently synthesized from β–bromovinyl aldehydes **7** in good to excellent yield by Sonogashira coupling[10] as per Scheme-7.
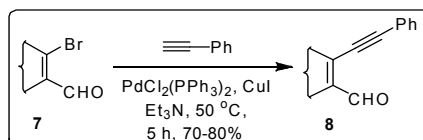
Scheme-7: Sonogashira coupling of β–bromovinyl aldehyde

The Sonogashira coupling of β–bromovinyl aldehydes was done with ethynyl benzene using PdCl$_2$(PPh$_3$)$_2$ (2 mol%) and CuI (1 mol%) as catalyst in Et$_3$N as solvent at 50 °C for 4-5 h which afforded the precursors 3-(1-alkynyl)-2-alkene-1-als **8**. The precursors on treatment with phenyl hydroxylamine (1.2 equiv), H$_2$O (5 equiv), Et$_3$N (1 equiv) and CuCl (10

mol%) in DMF at 85-90 °C under argon atmosphere for 2 h yielded the pyrrole derivatives **9** as the only isolable product (Scheme-8).
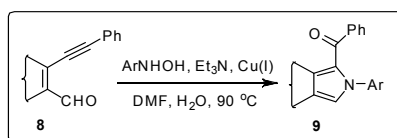
Scheme-8: Cu-catalyzed cyclization of 3-(1-alkynyl)-2-alkene-1-al

Optimization of reaction condition was done with **8a** as the model substrate by changing different types of solvents, bases and catalysts. When the reaction was carried out in an open flask only 10% product was formed with other side products. By lowering the temperature to 60 °C, very low yields were obtained (Table-1, entries 2-3). The reaction was then attempted by changing the catalyst, base and solvent to optimize the reaction conditions. The results are summarized in Table-1.

Table-1: Optimization of the reaction condition by using different types of solvents, bases and catalysts[a]
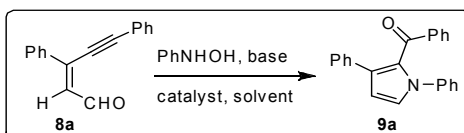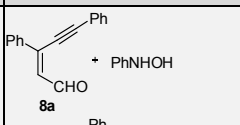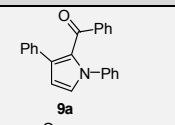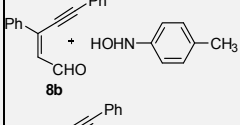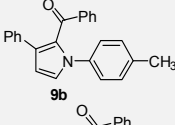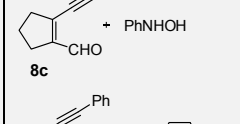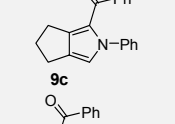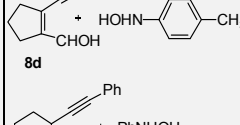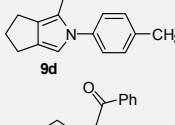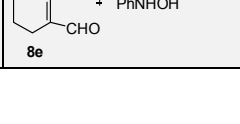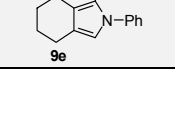
Entry	Catalyst	Base	Solvent	Temp (°C)	Yield (%)[b]
1	CuCl	Et$_3$N	DMF	85-90	78
2	CuCl	Et$_3$N	DMF	65-70	46
3	CuBr	Et$_3$N	DMF	85-90	20
4	CuI	Et$_3$N	DMF	85-90	10
5	CuCl	K$_2$CO$_3$	CH$_3$CN	85	NR
6	CuCl	Et$_3$N	CH$_3$CN	85	10
7	CuBr	Et$_3$N	Toluene	95	Dec

| 8 | CuCl | Na$_2$CO$_3$ | Toluene | 95 | Dec |
| 9 | CuCl | K$_2$CO$_3$ | DMF | 85-90 | NR |

[a]All the reactions were carried out in the presence of 5 equiv. H$_2$O, under argon atm. [b]Yields refer to the isolated yield after purification. NR = no reaction, Dec = Decomposition of starting material.

Finally, we examined the generality and substrate scope of this new cyclization reaction yielding pyrrole and isoindole (Table-2) derivatives with our optimization condition that was CuCl (10 mol%), 5 equiv H$_2$O, 1 equiv Et$_3$N in 4-5 mL DMF, heating at 85-90 °C for 2 h. Compound **8d** on reaction with this optimized condition yielded the pyrrole derivative **9d** as a yellow crystalline solid and the ORTEP structure of **9d** is shown in figure-2.

Table-2: Copper-catalyzed synthesis of pyrrole and isoindole derivatives[a]

Entry	Substrate	Product	Yield(%)[b]
1	**8a**	**9a**	82
2	**8b**	**9b**	78
5	**8c**	**9c**	81
6	**8d**	**9d**	78
7	**8e**	**9e**	72

[a]Reagents and conditions: **8a-8e** (1 equiv.), ArNHOH (1.2 equiv.), CuCl (10 mol%), Et$_3$N (1 equiv.), H$_2$O (5 equiv.), DMF (5 mL), 85-90 °C. [b]Yields refer to the isolated yield after purification.
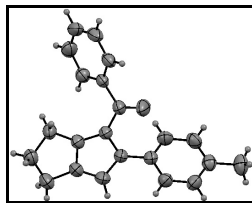
Figure-2: Crystal structure of compound **9d**

A plausible rationale for the formation of the products (**9a-9e**) is shown in scheme-4. At first aryl hydroxylamine react with the aldehyde group to form complex **A** (enol tautomer of an amide) which coordinate with the triple bond to form the complex **B** in which copper is replaced by hydrogen to form complex **C.** 1, 6-addition of water to the complex **C** followed by 1,5-H shift afforded the intermediate **E** which on H_2O elimination yielded our desired product.[11] The intermediates of this reaction were not isolated and the reaction may go through the nitrone intermediate.
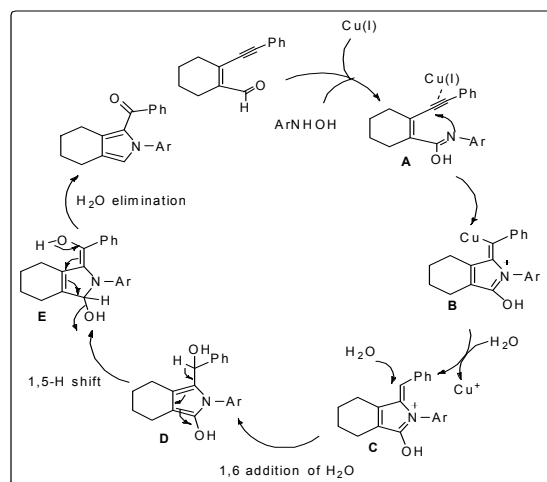
Scheme-9: plausible rationale for the Cu-catalyzed cyclization

Conclusion:

In this article we have discussed various methods for the synthesis of pyrrole derivatives using copper catalyst. All these methods are helpful for the synthesis of various natural products containing pyrrole moiety. The

products in our methodology can also be effectively used as a Diels-Alder precursor.

Acknowledgments:

References:

1. Daidone, G.; Maggio, B.; Schillaci, D.; Pharmazie 1990, 45, 441.
2. Almerico, A. M.; Diana, P.; Barraja, P.; Dattolo, G.; Mingoia, F.; Loi, A. G.; Scintu, F.; Milia, C.; Puddu, I.; La Colla, P.; Farmaco 1998, 53, 33.
3. (a) Kimura, T.; Kawara, A.; Nakao, A.; Ushiyama, S.; Shimozato, T.; Suzuki, K.; PCT Int. Appl. WO 0001688 A1 20000113, 2000; (b) Kaiser, D. G.; Glenn, E. M.; J. Pharm. Sci. 1972, 61, 1908.
4. Lehuede, J.; Fauconneau, B.; Barrier, L.; Ourakow, M.; Piriou, A.; Vierfond, J.-M.; Eur. J. Med. Chem. 1999, 34, 991.
5. Kawai, A.; Kawai, M.; Murata, Y.; Takada, J.; Sakakibara, M.; PCT Int. Appl. WO 9802430 A1 19980122, 1998.
6. Mal, D.; Shome, B.; Dinda, B. K.; Majumdar, K. C.; Chattopadhyay, S. K.; Heterocycles in Natural Product Synthesis. 2011, 187.
7. Furstner, A.; Angew. Chem. Int. Ed. 2003, 42, 3582.
8. (a) Frincke, J. M.; Faulkner, D. J.; J. Am. Chem. Soc. 1982, 104, 265; (b) Parker, K. A.; Cohen, I. D.; Padwa, A.; Dent, W.; Tetrahedron Lett. 1984, 25, 4917.
9. Nandi, S.; Ray, J. K.; Tetrahedron Lett. 2011, 52, 6203.
10. (a) Liang, Y.; Xie, Y.-X.; Li, J.-H.; J. Org. Chem. 2006, 71, 379; (b) Li, P.; Wang, L.; Li, H.; Tetrahedron 2005, 61, 8633;
11. Jana, R.; Paul, S.; Biswas, A.; Ray, J. K.; Tetrahedron Lett. 2010, 51, 273.

CHAPTER 8

A short note on Intramolecular palladium-catalyzed synthesis of fused pyran rings

✎ *Dr. Rathin Jana*

Department of Chemistry, Shahid Matangini Hazra Govt. General Degree College for Women, Kulberia, Purba Medinipur, West Bengal -721649, India.

E-mail: rathinj83@gmail.com

Introduction:

Palladium(II) complexes are extremely important in organo- palladium chemistry. They are typically electrophilic, soluble in most common organic solvents, and stable to air. Thus, they are easily stored and handled. The most common organic substrates for Pd(II) are electron-rich species, such as olefins, alkynes, and arenes.

Cyclization by palladium-catalyzed oxidative addition/ reductive elimination is a powerful method for the construction of heterocycles. This process generally involves the addition of a covalent molecule to a Pd(0) complex, with cleavage of the covalent bond and oxidation of Pd(0) to Pd(II), to afford a organopalladium(II) halide or triflate complex. The σ-bonded species, once formed, generally undergoes rapid insertion of an unsaturated species. Subsequent reductive elimination affords the desired heterocycle and Pd(0), which reenters the catalytic cycle directly, in contrast to Pd(II)-catalyzed reactions, which usually require an additional reoxidation step. The mechanistic details of these processes have been reviewed.[1-7] The palladium-catalyzed cyclization of vinylic/aryl halides or triflates containing neighboring alkenes, dienes, alkynes and arenes via oxidative addition/reductive elimination reactions provides a very valuable approach to a wide range of heterocycles.

Different methods:

Intramolecular Heck reactions have become a versatile tool in heterocyclic synthesis. Larock have reported the use of *o*-iodoaryl allyl ethers **1** as starting material in the preparation of benzofurans **2** via intramolecular Heck cyclization (Scheme 1).
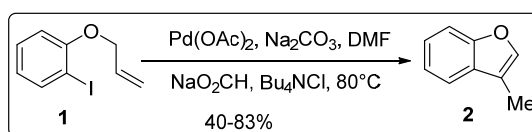
Scheme-1

This cyclization proceeds under mild conditions and in reasonably good isolated yields when catalytic amounts of Pd(OAc)$_2$, Na$_2$CO$_3$, HCO$_2$Na, and Bu$_4$NCl in DMF are employed at 80 ^{o}C. Mechanistically, these reactions appear to proceedas indicated in Scheme 2. The addition of HCO$_2$Na improves the overall yields of benzofurans.
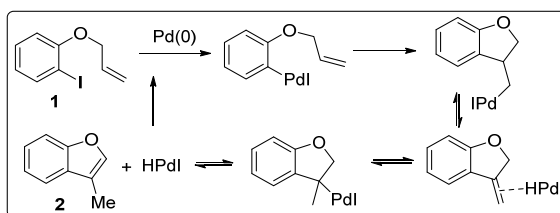
Scheme-2

Yum and co-workers also used sodium formate in their preparation of 3-alkylfuropyridines **4** from iodopyridinylallyl ethers **3** (Scheme 3). Allylic ethers **3** with longer side chains and 2-cyanopyridyl allyl ether provided lower yields of the desired products
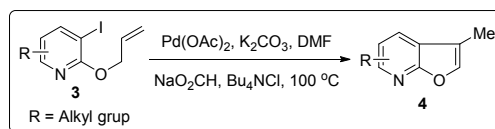
Scheme-3

Guillou and co-workers utilized an intramolecular Heck cyclization to prepare a benzopyran ring in their synthesis of the alkaloid lycoramine (Scheme 4). The tricyclicbenzopyran **6** was obtained from iodide **5** in 50% yield using catalytic Pd(OAc)$_2$/dppe in the presence of 1,2,2,6,6-pentamethyl-piperidine (PMP), tetrabutylammonium acetate and toluene as the solvent. In the absence of Bu$_4$NOAc or when Pd(OAc)$_2$ and MeCN were used at reflux, the product **6** was isolated in lower yields.
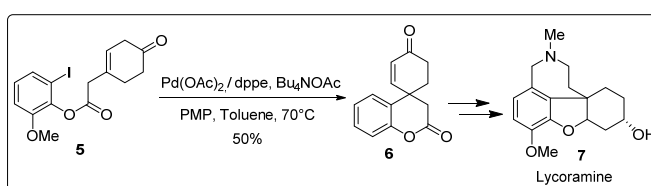
Scheme-4

The use of a catalytic couple composed of Rh(I) and Pd(II) to prepare enol ether **9** and allylic ether **10** has been described by Bankston and co-workers (Scheme 5). They found that a catalyst consisting of Rh(I) and Pd(II) gives the desired product in better yields than the use of Pd(II) alone. In the presence of Rh(I) *endo* cyclization was preferred. Other parameters, such as dilution, temperature and the palladium ligand can also effect the rate and selectivity.
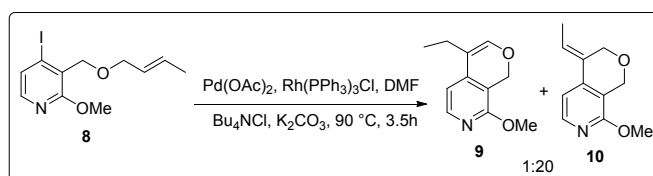
Scheme-5

Larock utilized the intramolecular Heck cyclization of 2,5-cyclohexadienyl-substituted aryl iodides to prepare functionalized heterocycles (Scheme 6). The reaction of a variety of carbon, nitrogen, oxygen, and sulfur nucleophiles with aryl iodides, such as **11**, in the presence of catalytic Pd(dba)$_2$ in DMSO at 100 ^{0}C afforded the heterocyclic compounds **12** in good yields and high diastereoselectivity. The reaction is believed to proceed via (1) Oxidative addition of the aryl halide to Pd(0), (2) Organopalladium

addition to one of the carbon-carbon double bonds, (3) Palladium migration along the carbon chain on the same face of the ring to form a σ-allylpalladium intermediate, and (4) Nucleophilic displacement of the resulting σ-allylpalladium species (Scheme 7).
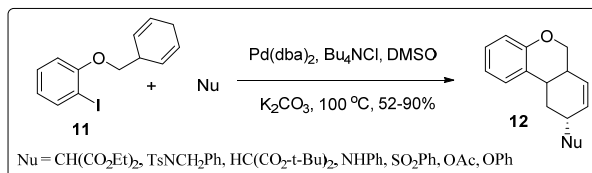
Scheme-6
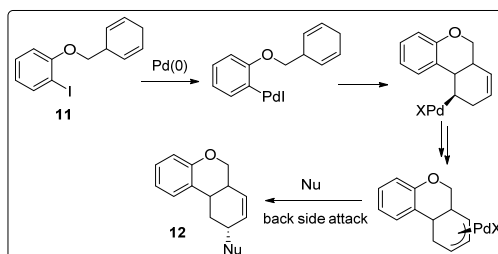
Scheme-7

Iodoarene **13** was found by Denmark and Schnute to undergo Pd-catalyzed intramolecular Heck cyclization in the presence of stoichiometric amounts of Pd(OAc)$_2$ and PPh$_3$ at room temperature to afford *exo* cyclic pyran derivative **14** (Scheme 8). The use of Ag$_2$CO$_3$ as a base and the nonpolar solvent benzene are crucial for the success of the reaction. The product was obtained as a single geometrical isomer along with the corresponding saturated nitroalkane **15**.
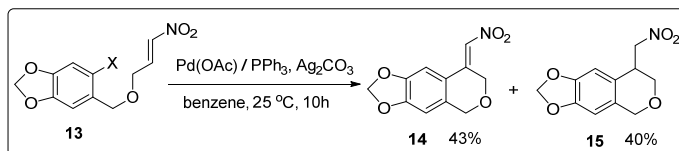
Scheme-8

The intramolecular Heck reaction of vinylic sulfones by catalytic Pd(0) in the presence of AgNO$_3$ generates polycyclic sulfones (Scheme 9). The vinylicsulfone **16** bearing an iodide provides a much higher yield of the cyclization product than the corresponding bromide. The absence of AgNO$_3$ afforded the cyclic product **17** accompanied by the allylic isomer **18**.
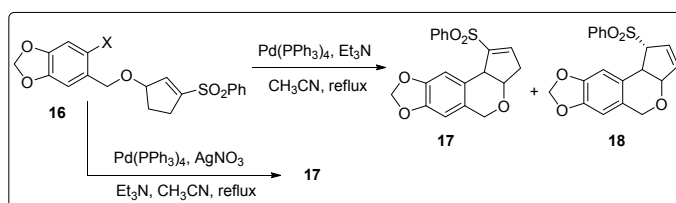
Scheme-9

The intramolecular Heck cyclization of the dienyne **19** with a methyl substituent provided the tetracyclic product **21** in good yield via 5-*exo-trig* cyclization of intermediate **20** and eventual *β*-hydride elimination (Scheme 10). On the other hand, when the hydrogen-substituted dienyne **19** was cyclized, it afforded tricyclic diene **23** in 52% yield via *endo* cyclization of **22** and subsequent *β*-hydride elimination.
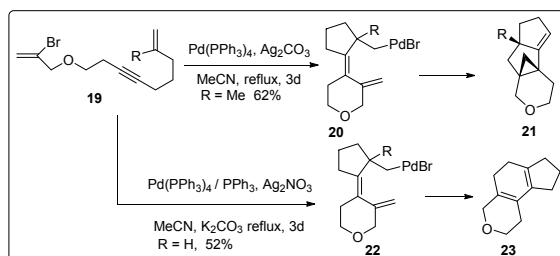
Scheme-10

We also developed a general method for the synthesis of pyran ring and tetracyclic pyran ring by palladium catalyzed *β*-H elimination or by C-H activation. The intramolecular Heck reaction was then performed with *O*-allylated **24** in the presence of Pd(OAc)$_2$, PPh$_3$, Cs$_2$CO$_3$ and TBAC (tetrabutyl-ammoniumchloride) in DMF at 80-85 °C to afford pyran derivatives **25** (Scheme 11).
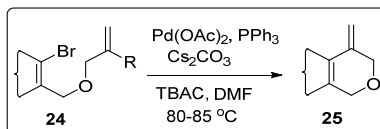
Scheme-11

The mechanism of this reaction is very simple. Initially an alkenyl palladium(II) intermediate was generated by oxidative addition of Pd(0) to the sp^2C–Br bond which undergoes addition to the unactivated double bond to produce an alkylpalladium which underwent β-H elimination reaction to afford pyran ring which is shown below (Scheme 12).
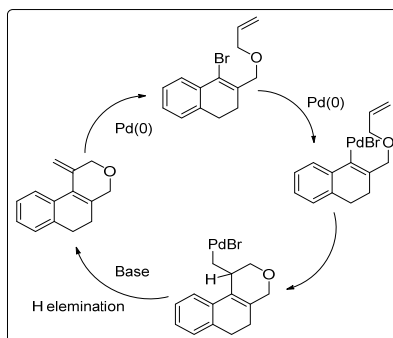
Scheme-12

During our studies, an interesting result was observed (Scheme 13). *O*-Methallylated compounds **26** were subjected to intramolecular Heck reaction under the same conditions to afford tetracyclic pyrans **27**.
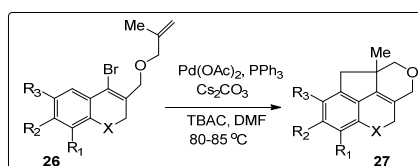
Scheme-13

A plausible mechanism for the above reaction is shown in Scheme 14. Initially an alkenylpalladium (II) intermediate was generated by oxidative addition of Pd(0) to the sp^2C–Br bond which undergoes addition to the unactivated double bond to produce an alkyl palladium which underwent

cyclization with the aromatic ring through C–H activation. Since no elimination is possible due to the absence of a *β*-H in the alkyl palladium intermediates, C–H activation is facilitated.
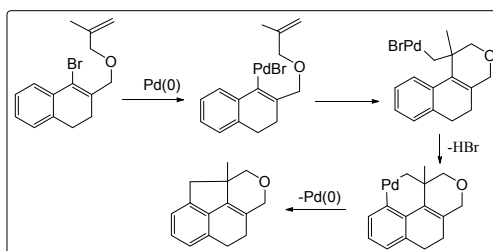
Scheme-14

Conclusion:

In conclusion, we have developed a method for the synthesis of fused pyran rings by intramolecular Heck reaction and tetracyclic pyran formation by intramolecular Heck reaction and regioselective C–H activation. It is possible to utilize this method for the synthesis of benzopyran systems and in this review we have discussed some different strategies for the synthesis of some pyran based natural product.

References:

1. Maitlis, P. M. The Organic Chemistry of Palladium; Academic Press: New York, 1971; Vols. 1 and 2.
2. Tsuji, J. Organic Synthesiswith Palladium Compounds; Springer-Verlag: New York, 1980.
3. Heck, R. F. Palladium Reagents in Organic Synthesis; Academic Press: New York, 1985.
4. Larock, R. C. In Advances in Metal-Organic Chemistry; Liebeskind, L. S., Ed.; JAI Press: London, 1994; Vol. V, Chapter 3.
5. Tsuji, J. Palladium Reagents and Catalysts: Innovations in Organic Synthesis; Wiley and Sons: New York, 1995.
6. Li, J. J.; Gribble, G. W. Palladium in Heterocyclic Chemistry; Pergamon: New York, 2000.
7. Negishi, E. Handbook of Organopalladium Chemistry for Organic Synthesis; Wiley and Sons: New York, 2002; Vols. 1 and 2.

CHAPTER

9

Self-Assembly of a {Cu$_5$} Complex Resulting from the Trapping of a Cu^{2+} Ion by Two {Cu$_2$} Building Units

✎ *Dr. Aloke Kumar Ghosh*

Department of Chemistry, Prabhat Kumar College, Contai, West Bengal-721404, India.

E-mail: akghosh1982@gmail.com

Introduction:

In recent years, high-nuclearity coordination complexes have attracted a major interest in the areas of both synthetic chemistry and molecular magnetism.[1,2] The synthetic strategy involving the self-assembly processes of dinuclear {Cu$_2$} building blocks around central oxido or metal ion and appropriate bridging/blocking ligands is a fascinating approach as the final outcome can never be totally predicted beforehand.[3] Because of the biological and biochemical importance of multicopper oxidase enzymes as dominant oxidizing agents toward different substrates in laccase,[4] ascorbate oxidase and nitrite reductase,[5] the understanding and synthetic control of the chemical aggregation of multi-copper coordination complexes is one of the major research areas in coordination chemistry.[6] Such coordination compounds are in general prepared *via* metal ion coordination driven self-assembly reactions with the use of suitable bridging and blocking ligands.[7] Among these Cu-based systems, pentanuclear assembly with a 'vertex-shared defective dicubane' core is not commonly encountered.[8] In these {Cu$_5$} systems, the vertices are composed of either a metal ions or oxygen donor atoms from an oxido, hydroxido or acetato group. The existing copper complexes involving all these three ligands as bridges and comprising multiple fused cubanes are extremely scarce.[9] In this perspective, the reactivity of the hexadenate/dinucleating phenolate Schiff base ligands like H$_3$bpmp (Chart 1, 2,6-bis-[(3-hydroxy-propylimino)-methyl]-4-methyl-phenol) with copper(II) in the presence of acetate anions have been explored. The use of this H$_3$bpmp ligand in transition-metal chemistry is relatively

new, the only compound known is a dinuclear hydroxido-bridged copper(II) complex.[10] It is worth noting that use of two closely related ligands, Hbip and Hcip (Figure 1, R = benzyl; Hbip: 2,6-*bis*(benzyl imino methyl)-4-methylpheno and R = cyclohexyl; Hcip: 2,6-*bis*(cyclohexyl imino methylene)-4-methylphenol), led to interesting systems, consisting of {Cu$_4$} complexes showing chemical reactivity and core conversion reactions.[11]
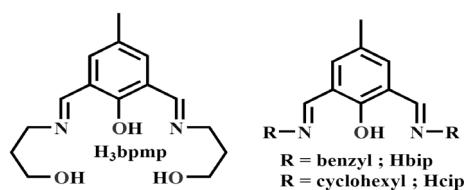
Figure-1

In this work, the coordinating and aggregating abilities of H$_3$bpmp (Scheme-1 and 2) the together with the varying binding properties of acetate ions, has been exploited to the preparation of a novel pentanuclear complex [Cu$_5$(μ_3-OH)$_2$(H$_2$bpmp)$_2$($\mu_{1,1}$-OAc)$_2$($\mu_{1,1,3}$-OAc)$_2$(OAc)$_2$]·2H$_2$O (**1**·2H$_2$O).
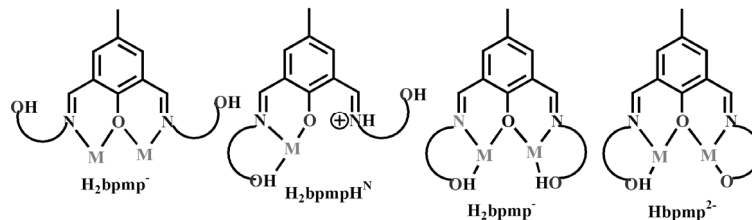
Scheme-1: Different binding modes of H$_3$bpmp
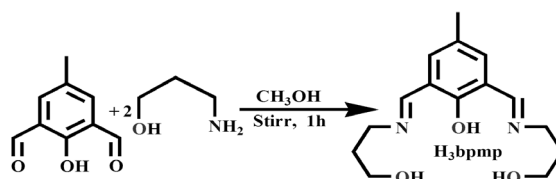
Scheme-2: Synthesis of the H$_3$bpmp ligand

Experimental Section:

The chemicals used were obtained from the following sources: copper(II) acetate monohydrate from S. D. Fine Chemicals, triethylamine from Merck, India and 3-amino-1-propanol from Aldrich Chemical Co. Inc. US. All other chemicals and solvents were reagent-grade materials and were used as received without further purification. 2,6-Diformyl-4-methylphenol (2-hydroxy-5-methyl-benzene-1,3-dicarbaldehy de) was prepared following a literature procedure.[12] The elemental analyses (C, H, N) were performed with a Perkin-Elmer model 240 C elemental analyzer. Fourier transform infrared (FTIR) spectra were recorded on a Perkin-Elmer RX1 spectrometer. Solution electrical conductivity measurements and electronic spectra were carried out using a Unitech type U131C digital conductivity meter with a solute concentration of about 10^{-3} M and a Shimadzu UV 3100 UV-vis-NIR spectrophotometer, respectively. The magnetic susceptibility measurements were obtained with the use of a Quantum Design SQUID magnetometer MPMS-XL. This magnetometer works between 1.8 and 400 K for dc applied fields ranging from -7 to 7 T. Measurements were performed on microcrystalline samples of 22.13 mg for **1**·$2H_2O$. The magnetic data are corrected for the sample holder and the diamagnetic contributions.

Synthesis of Ligand: The H_3bpmp Schiff-base ligand was prepared from the single step condensation of 2,6-diformyl-4-methylphenol (1.0 g, 6.1 mmol) and 3-amino-1-propanol (0.91 g, 12.2 mmol) in methanol (20 mL) in air at room temperature (28 °C) under stirring for 2 h. Complete evaporation of solvent in air for 12 h yielded an orange colored semi-solid product which was used directly for reaction without further characterization. Yield: 1.32g (78%).

Synthesis of [Cu$_5$(μ_3-OH)$_2$(μ-bpmp)$_2$($\mu_{1,1}$-OAc)$_2$($\mu_{1,1,3}$-OAc)$_2$(OAc)$_2$]·2H$_2$O: A methanolic solution (10 mL) of Cu(OAc)$_2$·H$_2$O

(0.599 g, 3.00 mmol) was added to the H$_3$bpmp ligand (0.278 g, 1.00 mmol) in methanol (20 mL) slowly followed by addition of NEt$_3$ (139 mL, 0.101 g, 1.00 mmol). The resulting solution was stirred for 2 h at room temperature. The solvent was evaporated in air to give a green solid that was isolated,

washed with cold methanol and dried under vacuum over P_4O_{10}. Green crystals suitable for X-ray analysis were obtained from a MeOH solution after two weeks. Yield: 0.492 g, 76%. Anal. Calcd. for $C_{42}H_{66}Cu_5N_4O_{22}$ (1296.71 g mol^{-1}): C, 38.90; H, 5.13; N, 4.32. Found: C, 38.82; H, 5.22; N, 4.22. Selected FT-IR bands: (KBr, cm^{-1}; s = strong, vs = very strong, m = medium, br = broad) 3387(br), 2926(s), 1638(s), 1578(s), 1396(vs), 1334(s), 1076(vs), 918(m), 681(m), Molar conductance, Λ_M: (MeOH solution) 6.3 Ω^{-1} cm^2 mol^{-1}. UV-vis spectra [λ_{max}, nm (ε, L mol^{-1} cm^{-1})]: (MeOH solution) 666 (235), 370 (5120), 210 (17700).

Crystal Structure Determination: The diffraction data of the complex **1**·2H_2O was collected on a Bruker APEX-II CCD X-ray diffractometer using single crystals that uses graphite-monochromated Mo-K_α radiation (λ = 0.71073 Å) by ω-scan method at 293 K. Information concerning X-ray data collection and structure refinement of the compound is summarized in Table-1. For complex **1**·2H_2O, a total of 7960 reflections were recorded with Miller indices h_{min} = -16, h_{max} = 16, k_{min} = -19, k_{max} = 20, l_{min} = -23, l_{max} = 22. In the final cycles of full-matrix least squares on F^2, all non-hydrogen atoms were assigned anisotropically. The structures were solved using the SHELX-97 program system.

Table-1: Crystallographic data for **1**·2H_2O

1	compound	1·2H_2O	16	$F(000)$	1334
2	formula	$C_{42}H_{66}Cu_5N_4O_{22}$	17	crystal size/mm	0.36 x 0.25 x 0.15
3	M	1296.71	18	μ(Mo-Kα)/cm^{-1}	20.47
4	space group	$P 2_1/c$	19	measured Refl.ns	39472
5	crystal system	monoclinic	20	unique Ref.ns	7960
6	a/Å	11.4604(7)	21	R_{int}	0.0377
7	b/Å	13.7598(8)	22	obs. refl. ns I≥2σ(I)	5671

8	c/Å	17.3334(10)	23	θ_{min}- θ_{max}/°	1.83 -31.86
9	α/deg	90.0	24	hkl ranges	-16, 16;-19, 20; -23,22
10	β/deg	103.317(2)	25	$R(F^2)$ (obs.refl.ns)	0.0367
11	γ/deg	90.0	26	$wR(F^2)$ (all refl.ns)	0.1009
12	V/Å^3	2659.85(3)	27	no. variables	347
13	T/K	293	28	GOF	1.026
14	Z	3	29	$\Delta\rho_{max}$; $\Delta\rho_{min}$ (e Å^{-3})	0.621; -0.481
15	D_c/g cm^{-3}	1.619			

$R_1 = (\quad F_o \quad F_c \quad)/ \quad F_o$. $wR_2 = [\quad w(\quad F_o \quad F_c \quad)^2/ \quad w(F_o)^2]^{1/2}$. $w = 0.75/(\quad ^2(F_o) +0.0010F_o{}^2)$.

Details of X-ray Analysis: $C_{42}H_{66}Cu_5N_4O_{22}$, $M = 1296.71$, monoclinic, space group $P2_1$/c, crystal size = 0.36 x 0.25 x 0.15 mm^3, $a = 11.4604(7)$ Å, $b = 13.7598(8)$Å, $c = 17.3334(10)$Å, $\beta = 103.317(2)$°, $V = 2659.85(3)$ Å^3, T = 293K, Z =3, $\rho_{calcd} = 1.619$ gcm^{-3}, μ(Mo-Kα) = 20.47 mm^{-1}; θ ranges (°) = 1.83 to 31.86; 39472 reflections measured, 7960 independent reflections (R_{int} = 0.0377), refinement converged to $R = 0.0367$, $wR_2(F^2)[I>2\sigma(I)] = 0.1009$, GOF = 1.026, max./min. residual electron density = +0.621/−0.481. CCDC 832928 contains the supplementary crystallographic data for **1**·2H$_2$O. The data can be obtained free of charge www.ccdc.cam.ac.uk/conts/ retrieving.html [or from the Cambridge Crystallographic Data Centre, 12, Union Road, Cambridge CB2 1EZ, U.K.; fax, +44-1223/336-033; e-mail, deposit@ccdc.cam.ac.uk

Results and Discussion:

Complex **1**·2H$_2$O was obtained as a precipitate in 76% yield from MeOH, as summarized in eq. 1, clearly accounting for the formation the two hydroxido bridges from the water molecule present in the organic solvent medium. The elemental analysis, molar conductivity and single-crystal X-ray diffraction (*vide infra*) data confirm the given formula [Cu$_5$(μ-H$_2$bpmp)$_2$(μ_3-OH)$_2$($\mu_{1,1}$-OAc)$_2$($\mu_{1,1,3}$-OAc)$_2$(OAc)$_2$] for **1**.

2H$_3$bpmp + 5Cu(OAc)$_2$·H$_2$O + 4NEt$_3$ $\longrightarrow$

[Cu$_5$(μ-H$_2$bpmp)$_2$(μ_3-OH)$_2$($\mu_{1,1}$-OAc)$_2$($\mu_{1,1,3}$-OAc)$_2$(OAc)$_2$]·2H$_2$O   +
4(HNEt$_3$)(OAc) + H$_2$O   (1)
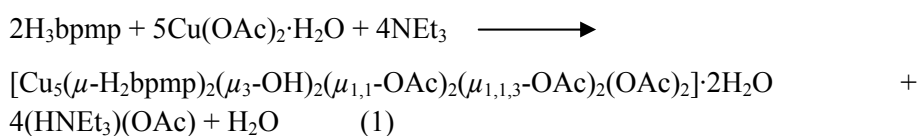
The crystallographic asymmetric unit consists of one-half of the pentanuclear unit and one interstitial solvent H$_2$O molecule. The asymmetric unit grows around a 2_1 axis perpendicular to the crystallographic *c* axis. The second half of the complex is generated by symmetry operations (-x, 1-y, -z). The complex **1** is a centrosymmetric pentanuclear Cu^{II} species formed of two defective cubanes around the central Cu^{II} with a [Cu$_5$O$_{10}$] core (Figures 1, 2, 3 and 4), important bond lengths and angles listed in Table 2, where the bridges between metal ions are ensured by two water derived μ_3-OH anions, four acetato ligands (two each in $\mu_{1,1,3}$, $\mu_{1,1}$ modes) and two μ-phenoxido moieties from deprotonated H$_2$bpmp ligands.

Table-2: Selected inter-atomic distances (Å) and angles (º) for complex **1**·2H$_2$O

Distances			
O(3)-Cu(2)	1.925(1)	Cu(2)-N(1)	1.953(2)
O(4)-Cu(1)	2.253(1)	Cu(2)-O(1)	1.970(1)
Cu(1)-O(2)	1.981(1)	Cu(2)-O(6)*	2.376(1)
Cu(1)-O(2)*	1.981(1)	Cu(2)-Cu(3)	3.058(4)
Cu(1)-O(6)	2.009(1)	Cu(3)-O(2)	1.930(1)
Cu(1)-O(6)*	2.009(1)	Cu(3)-O(8)	1.935(1)
Cu(1)-O(4)*	2.253(1)	Cu(3)-N(2)	1.941(2)
Cu(1)-Cu(2)	2.969(3)	Cu(3)-O(1)	1.984(1)
Cu(1)-Cu(2)*	2.969(3)	O(6)-Cu(2)	2.376(1)
Cu(2)-O(2)	1.9325(1)		

Angles			
O(2)-Cu(1)-O(2)*	180.0	O(2)-Cu(2)-N(1)	170.4(7)
O(2)-Cu(1)-O(6)*	87.1(7)	O(3)-Cu(2)-O(1)	166.3(7)
O(2)*-Cu(1)-O(6)*	92.8(7)	O(2)-Cu(2)-O(1)	77.1(6)
O(2)*-Cu(1)-O(6)	92.8(7)	N(1)-Cu(2)-O(1)	93.3(7)
O(2)*-Cu(1)-O(6)	87.1(7)	O(3)-Cu(2)-O(6)*	102.2(7)
O(6)-Cu(1)-O(6)*	180.0	O(2)-Cu(2)-O(6)*	78.6(6)
O(2)-Cu(1)-O(4)*	88.8(6)	N(1)-Cu(2)-O(6)*	100.3(7)
O(2)-Cu(1)-O(4)	91.1(6)	O(1)-Cu(2)-O(6)*	86.0(6)
O(6)*-Cu(1)-O(4)*	87.3(7)	O(3)-Cu(2)-Cu(1)	84.7(5)
O(6)*-Cu(1)-O(4)	92.6(7)	O(2)-Cu(2)-Cu(1)	41.2(5)
O(2)-Cu(1)-O(4)	91.1(6)	N(1)-Cu(2)-Cu(1)	140.9(6)
O(2)*-Cu(1)-O(4)	88.8(6)	O(1)-Cu(2)-Cu(1)	94.5(4)
O(6)*-Cu(1)-O(4)	92.6(7)	O(6)*-Cu(2)-Cu(1)	42.3(4)
O(6)*-Cu(1)-O(4)*	87.3(7)	O(3)-Cu(2)-Cu(3)	130.5(5)
O(4)*-Cu(1)-O(4)	180.0	O(2)-Cu(2)-Cu(3)	37.6(5)
O(2)-Cu(1)-Cu(2)	40.0(5)	N(1)-Cu(2)-Cu(3)	132.8(6)
O(2)-Cu(1)-Cu(2)*	139.9(5)	O(1)-Cu(2)-Cu(3)	39.5(4)
O(6)*-Cu(1)-Cu(2)	52.8(4)	O(6)*-Cu(2)-Cu(3)	80.2(4)
O(6)*-Cu(1)-Cu(2)*	127.1(4)	Cu(1)-Cu(2)-Cu(3)	63.9(7)
O(4)-Cu(1)-Cu(2)*	105.2(4)	O(2)-Cu(3)-O(8)	94.6(7)
O(4)-Cu(1)-Cu(2)	74.7(4)	O(2)-Cu(3)-N(2)	167.4(8)
O(2)*-Cu(1)-Cu(2)	139.9(5)	O(8)-Cu(3)-N(2)	97.1(8)
O(2)*-Cu(1)-Cu(2)*	40.0(5)	O(2)-Cu(3)-O(1)	76.8(6)
O(6)-Cu(1)-Cu(2)	127.1(4)	O(8)-Cu(3)-O(1)	167.2(7)
O(6)-Cu(1)-Cu(2)*	52.8(4)	N(2)-Cu(3)-O(1)	92.1(7)
O(4)-Cu(1)-Cu(2)	74.7(4)	O(2)-Cu(3)-Cu(2)	37.6(5)
O(4)*-Cu(1)-Cu(2)	105.2(4)	O(8)-Cu(3)-Cu(2)	131.6(5)
Cu(2)-Cu(1)-Cu(2)*	180.0	N(2)-Cu(3)-Cu(2)	131.0(6)
O(3)-Cu(2)-O(2)	93.6(7)	O(1)-Cu(3)-Cu(2)	39.1(4)
O(3)-Cu(2)-N(1)	95.8(7)	Cu(3)-O(2)-Cu(2)	104.6(8)
Cu(3)-O(2)-Cu(1)	109.3(8)	Cu(2)-O(2)-Cu(1)	98.6(7)
*: -x, 1-y,- z			
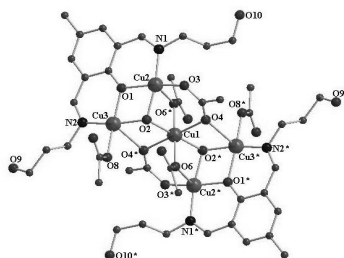
Figure-1: View of the pentanuclear unit of $[Cu_5(\mu\text{-}H_2bpmp)_2(\mu_3\text{-}OH)_2(\mu_{1,1}\text{-}OAc)_2(\mu_{1,1,3}\text{-}OAc)_2(OAc)_2]\cdot 2H_2O$ in **1**·$2H_2O$
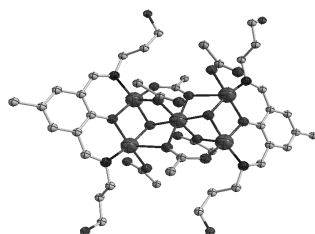
Figure-2: DIAMOND view of **1**·$2H_2O$ showing the ligand with different colors; red, O; blue, N; brown, Cu; pink, H_2bpmp (the thermal ellipsoids are shown at a 40% probability).
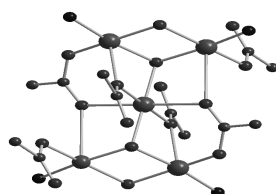
Figure-3: View of the atom connectivity within the $[Cu_5]$ complex with three different types of acetato binding modes in **1**·$2H_2O$. Color code: brown, Cu; blue, N; red, O; black, C.
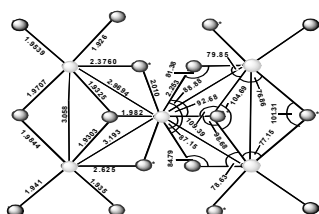
Figure-4: Atom connectivity of the pentanuclear Cu(II) core in **1**·2H$_2$O with the relevant inter-atomic bond distances (Å) and angles (°). Atoms labeled with a '*' are generated from the parent atoms through the symmetry operation (-x, 1-y, - z).

The central Cu(I) adopts an *octahedral* coordination sphere with an O$_6$ donor environment made from the coordination of hydroxido [O(2)] and acetate [O(4) and O(6)] groups having long Cu(I)-O(4) *apical* bonds (2.253 Å) as expected from a Jahn-Teller distortion along the *z* axis. (Figure-5). The remaining coordination sites of the *square pyramidal* Cu^{II} ions (Addison[13] τ values 0.06 and 0.003) are completed by peripheral imine groups from H$_2$bpmp ligands. Interestingly, both the alcohol arms of the ligand H$_2$bpmp remain uncoordinated and one of them is engaged in inter-molecular hydrogen-bonding interactions with water molecules of crystallization (Figure-5).
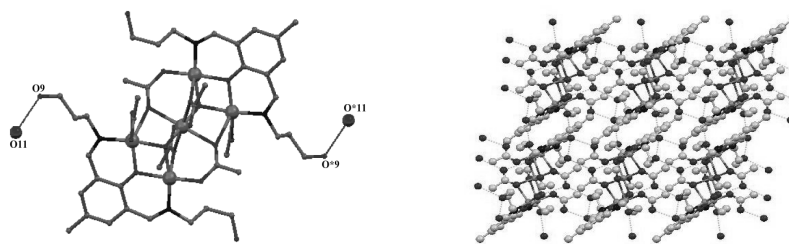
Figure-5: Ball and stick style representations of **1**·2H$_2$O emphasizing the intra- and inter-molecular hydrogen bonds (labeled in pink lines) established around the [Cu$_5$] complex (left) and in the three-dimensional network viewed along *b* axis (labeled in dotted green lines) (right).

The other uncoordinated arms show intra-molecular hydrogen-bonding interactions with free carbonyl oxygen atoms of bridging $\mu_{1,1}$ acetate groups. There are all together three different types of acetate groups present in the compound (Figure-6).
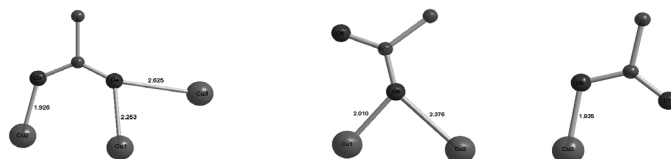
Figure-6: Different coordinating modes of the acetate ligands in 1.

The affinity of the copper(II) ions for long distance binding along the *apical* Jahn-Teller axis is responsible for the binding of six AcO ions in these three different modes. Inspection of Figure 1 suggests indeed that the formation of **1** occurs through trapping of an $[Cu(OAc)_2(H_2O)_2]$ species by two hitherto unknown $\{Cu_2\}$ fragments $[Cu_2(\mu\text{-}H_2bpmp)_2(\mu\text{-}OH)(OAc)_2]$. During this assembly, the double hydroxido bridge of the $\{Cu_2\}$ fragments extends its binding capacity to μ_3-OH and one of the acetato group to $\mu_{1,1}$-OAc. The trapped acetato groups of $[Cu(OAc)_2(H_2O)_2]$ are converted to $\mu_{1,1}$ mode and one acetato group on each metal ion of the $\{Cu_2\}$ fragments is transformed to $\mu_{1,1,3}$ mode. These three different types of AcO binding modes in a single acetate rich complex are rather exceptional. The two hydroxido bridges have the primary control on the formation of the $\{Cu_5\}$ entity like that observed in copper-based minerals shattuckite, $Cu_5(OH)_2(SiO_3)_4$, cornubite, $Cu_5(OH)_2(AsO_4)_2$ and chloride in place of hydroxide in copper selenite chloride compound, $Cu_5Cl_2(SeO_3)_4$. The five Cu^{II} atoms of the complex are at five vertices of a 'vertex shared opened-dicubane' where one vertex of each cubane is missing and the octahedral copper(II) center occupies a mutual vertex of each opened-cubane (Figure-7). The vertex-shared $\{Cu_5\}$complex **1** results from the binding of two μ-H_2bpmp ligands in front of Cu^{II}/AcO system, as opposed to tetranuclear or dinuclear complexes (Scheme-3).
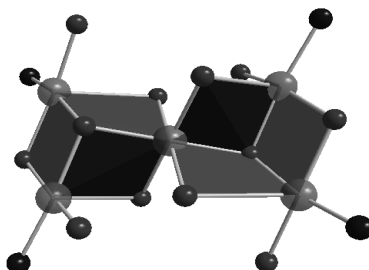
Figure-7: Vertex shared dicubane structure showing three colored (blue, green and pink) tetragonal faces of two partial cubanes.
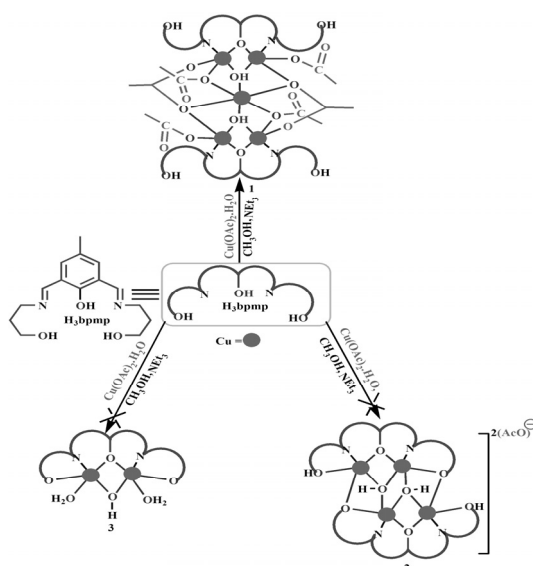
Scheme-3: Schematic representation of the non-formation of {Cu2} and {Cu4}, and formation of {Cu$_5$} assemblies.

Conclusions:

In summary, a new pentanuclear {Cu$_5$} complex, **1** has been synthesized by the combined action of AcO and HO anions, together with the H$_3$bpmp Schiff base ligand. This aggregate possesses a rare geometry that can be described as a double defective cubanes sharing a central Cu(II) vertex that is stabilized by a set of bridging acetates in $\mu_{1,1}$ and $\mu_{1,1,3}$-mode, two hydroxides in μ_3-mode and phenoxido groups in normal two centered

bridging mode. These bridges mediate within the pentanuclear complex **1**, dominating antiferromagnetic interactions inducing an $S_T = \frac{1}{2}$ spin ground state. This work emphasizes the role of acetate ligands for the self-assembly of two H_2bpmp^- ligated $\{Cu_2\}$ fragments responsible for the trapping of the central Cu^{2+} ion.

Acknowledgements:

References:

1. E. C. Yang, D. Ding, Z. Y. Liu, Y. L. Yang, X. J. Zhao, Cryst. Growth Des. 2012, 12, 1185.
2. E. E. Moushi, C. Lampropoulos, W. Wernsdorfer, V. Nastopoulos, G. Christou, A. J. Tasiopoulos, J. Am. Chem. Soc. 2010, 132, 16146.
3. R. E. P. Winpenny, J. Chem. Soc., Dalton Trans. 2002, 1.
4. E. I. Solomon, U. M. Sundaram, T. E. Machonkin, Chem. Rev. 1996, 96, 2563.
5. M. Kumar, N. A. Dixon, A. C. Merkle, M. Zeller, N. Lehnert, E. T. Papish, Inorg. Chem. 2012, 51, 7004.
6. X. M. Zhang, J. Lv, F. Ji, H. S. Wu, H. Jiao, P. v. R. Schleyer, J. Am. Chem. Soc. 2011, 133, 4788.
7. S. Ali, C. A. Muryn, F. Tuna, R. E. P. Winpenny, Dalton Trans. 2010, 39, 124.
8. Y. Ma, Y. Q. Wen, J. Y. Zhang, E. Q. Gao, C. M. Liu, Dalton Trans. 2010, 39, 1846.
9. S. Majumder, S. Sarkar, S. Sasmal, E. C. Sañudo, S. Mohanta, Inorg. Chem. 2010, 50, 67540.
10. S. K. Mandal, K. J Nag, Chem. Soc. Dalton. Trans. 1984, 2141
11. M. Sarkar, R. Clérac, C. Mathonière, N. G. R. Hearns, V. Bertolasi, D. Ray, Inorg. Chem. 2010, 49, 6575.
12. R. R. Gagne, C. L. Spiro, T. J. Smith, C. A. Hamann, W. R. Thies, A. K. Shiemke, J. Am. Chem. Soc. 1981, 103, 4073.
13. G. M. Sheldrick, SHELX-97, Program for Crystal Structure and Refinement, University of Göttingen, Germany, 1997.

CHAPTER

10

Antimicrobial Photodynamic Therapy: A Promising Alternative for COVID-19 Treatment

✍ *Dr. Moumita Gangopadhyay*

Department of Chemistry, Ghatal Rabindra Satabarsiki Mahavidyalaya, Paschim Medinipur, W. B.-721212, India.

E-mail: mgangopadhyay@grsm.ac.in

Introduction:

"Infectious diseases" are defined as the impairment of a person's health, mainly caused by microorganisms. The four main types of agents responsible for infectious diseases are bacteria, viruses, fungi, and parasites.[1a] The late 20th century and early 21st century have witnessed the occurrence of several infectious diseases viz. severe acute respiratory syndrome (SARS), influenza (influenza viruses), Ebola-virus-induced hemorrhagic fever, infectious diarrhea, common cold (like coronaviruses), etc. Scientists have attributed this growing occurrence of infectious diseases to increasing antimicrobial resistance (AMR).[1a] World Health Organization (WHO) has named it the "Silent Tsunami" and has included it in the 2030 sustainable development agenda.[1b]

Photodynamic therapy (PDT) has been proven a promising alternative in overcoming AMR owing to the high spatiotemporal control it provides, the non-invasive nature of treatment using light of a specific wavelength, and the involvement of reactive oxygen species (ROS).[2] PDT involves excitation of an organic chromophore, named photosensitizer (PS), by light, preferably in the region of visible or near-infrared (NIR).[2] Upon excitation of the PS with light of a specific wavelength, the PS can generate different ROS e.g. hydroxyl radical, superoxide radical, and other free radicals (Type I) or singlet oxygen (Type II).[2] These reactive species can inhibit infectious diseases mainly via three pathways: (i) interacting with the

DNA/RNA viruses/bacteria, (ii) denaturing their protein-membrane, and (iii) destroying the host cell membrane.[3] Earlier PSs were designed based on various cyclic tetrapyrrole derivatives e.g. porphyrin, Meso-tetra(hydroxyphenyl)porphyrins (m-THPP), sulfonated derivatives (TPPS4), hematoporphyrin, etc., often referred to as first-generation PSs.[3] Various porphyrin derivatives developed in the late 1980s, e.g. zinc phthalocyanine CGP55847, naphthalocyanine, etc., are regarded as second-generation PSs.[4] Of late, third-generation PSs have been developed, which include PSs decorated onto nanoparticles, liposomes, oil-in-water emulsions, antibody conjugates, and other biological delivery vehicles.[5]

The photoactive inactivation of microorganisms was first reported by Rabb in the early 20th century. Raab detected the inefficiency of acridine-based dyes toward *Paramecium caudatum* in absence of light; however, these dyes showed promising toxic effects in the presence of light.[3] The advanced study on the application of PDT for the treatment of common human diseases caused by viruses/bacteria started way back in 1930. The initially reported treatments were all focused on viral lesions. The first disease treated with clinical PDT was herpes, as reported in 1970.[6] PDT has also been utilized in treating several bacterial infections that are otherwise resistant to existing antibiotics like several gram-positive and gram-negative bacteria, *Pseudomonas aeruginosa*, *Escherichia coli*, etc.[2] Extensive research in this field has established a diverse range of PDT protocols against microorganisms like human papillomatosis virus (HPV), human immune deficiency viruses (HIV), hepatitis viruses (A, B, and C), human T-cell lymphotropic viruses etc.[7]

Since late 2019, the COVID-19 pandemic has hit hard in almost all areas of human society. This pandemic is caused by a new form of coronavirus, which has been found to spread at a very high rate. In the first and second waves of the pandemic, severe bilateral pneumonia, along with other immunological changes, brain death, and stroke due to lack of oxygen supply were reported, especially in patients above 60 or those with comorbidities. The high mortality rates in both these waves can be attributed to the lack of suitable antiviral drugs or vaccines. After relentless efforts

from researchers worldwide, we finally have vaccines at our disposal, which have been proved effective in restricting the infection to a large extent. However, scientists are working toward new cheaper, handier, and safer ways of combating this deadly virus. To this end, various research groups are exploring PDT as an alternative non-invasive treatment modality against COVID-19, keeping in mind the successful photoactive inactivation of different human viruses as mentioned above.

Mechanism of Antimicrobial PDT Against Viruses:

Classical PDT utilizes a PS, a suitable light source, and oxygen, the basic mechanism of PDT involves excitation of the PS from its ground state (PS) to the first singlet excited state ($^1PS^*$), from where it can undergo intersystem crossing (ISC) to reach its triplet excited state ($^3PS^*$) (Figure 1).[2] The PS in its triplet excited state can dissipate its excess energy via two pathways: (i) electron transfer to the substrate (Type I) leading to the formation of ROSs like superoxide, hydroxyl, peroxide radicals, etc. and (ii) energy transfer to ground-state triplet oxygen ($^3O_2$), generating excited singlet oxygen ($^1O_2$) (Type II).[5]
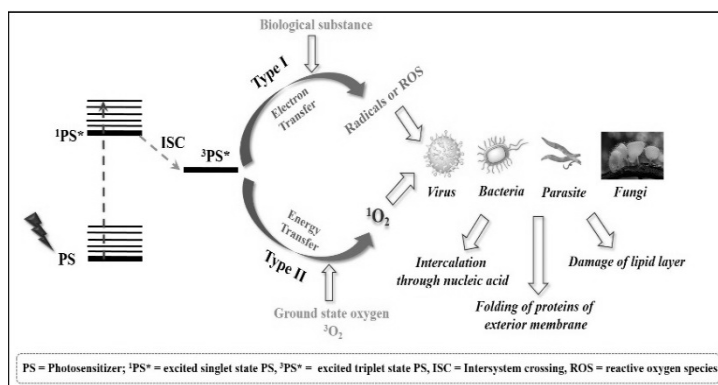
Figure-1: Schematic representation of antimicrobial PDT

The thus-generated radicals or ROSs can react with proteins, amino acids, nucleic acids (DNA/RNA of the virus), lipids, etc., leading to a cascade of Type I reactions, which result in cross-linking and destruction of

biological substances/ microorganisms.[8] Singlet oxygen generated via the Type II mechanism reacts directly with the components of the cytoplasmic membrane, which in turn generates peroxide radicals detrimental to the virus. Since $^1O_2$ can pass through the cytoplasmic membrane, the Type II mechanism can also damage the outer membrane upon reaction with proteins or fatty acids therein.[3]

The coronavirus responsible for COVID-19, i.e. SARS-CoV-2, has been shown to bind with the heme group of hemoglobin. The heme group contains an iron atom, which binds oxygen during blood flow between lungs and tissues. The non-structural proteins of SARS-CoV-2 remove iron from hemoglobin, thus interfering with the oxygen supply from alveoli to capillaries and causing hypoxia.[9a] Following this study, researchers have tried exploring porphyrin-based PSs for inhibition of the COVID-19 virus. In this case, the virus binds to the PS instead of the healthy hemoglobin or the lung tissues. Thereafter, an appropriate light source is used to excite the PS to generate ROSs, thus destroying the SARS-CoV-2 virus attached with it.[9a]

Choice of Photosenstizers (PSs):

An ideal PS must fulfill the following criteria: (i) strong absorbance in the visible/NIR light window (wavelength range of 600–800 nm) for deep tissue penetration, (ii) high triplet excited-state lifetime, and high triplet quantum yield ($\Phi_T \geq 0.5$), (iii) facile ISC, (iv) high singlet oxygen quantum yield, (v) minimum toxicity in absence of light, (vi) better solubility in a biological medium, etc.[3] In addition to these, a PS should satisfy a few more criteria for effective application against viruses, such as (i) intracellular localization, (ii) efficient DNA/RNA binding property, and (iii) selective localization in specific organelles.[3] Amphiphilic PSs are the best choices for antimicrobial PDT. These PSs are sufficiently water-soluble and hydrophobic enough to diffuse through the cell membranes of the bacteria/virus.

Viruses contain a nucleic acid core (e.g. single/double-stranded DNA/RNA) surrounded by a protein/lipid-based exterior.[3] Positively charged PSs, e.g. methylene blue, show better internalization through the outer

membrane of the virus envelope. Another advantage of such cationic PS is their facile intercalation into the negatively charged DNA/RNA. Few PSs like protoporphyrin IX, hematoporphyrins, 5-amino levulinic acid, etc. interact with the unsaturated lipid layer or the proteins present in the outer membrane via radical formation and subsequent cross-linking or via protein folding, leading to suppressed virus action.[9b] Anionic PSs aggregate more easily, leading to reduced singlet oxygen generation; however, such PSs can accumulate in the virus by attaining helical structure.

Following this line of research, many PSs have been well established for the inhibition of different human viruses, e.g. curcumin for HPV/MNV-1, phthalocyanines for HIV, Riboflavin (MERS), Phenothiazine methylene blue for hepatitis C virus (HCV), and Sindibis virus, etc.[3] Based on the successful application of PDT for plenty of human viruses, several PSs have been explored for the treatment of early variants of coronavirus (Table-1).

Table-1: Different PSs used for earlier variants of coronaviruses

PS	Virus Target	Virus Genome Type	Reference
Psoralen Amotosalen	Zika Virus, SARS Corona virus	RNA (enveloped)	10 11
Riboflavin	MERS	RNA (enveloped)	12
Solid-phase Fullerene	Influenza A	RNA (enveloped)	13
Methylene Blue	Dengue Virus	RNA (enveloped)	13
Octacationic octakis (cholinyl) zinc phthalocyanine	Avian influenza A virus (H5N8)	RNA (enveloped)	13
Oligolysine-	Influenza A		13

conjugated zinc(II) Phthalocyanines	virus (H1N1)	RNA (enveloped)	

Application of Antimicrobial PDT for COVID-19:

Considering the fast mutation of the present coronavirus, it is very difficult to develop a particular medication/vaccine, which can be effective against all the different variants. On the other hand, PDT inhibits viral infection by means of short-lived ROSs, thereafter making the treatment a very localized one. Hence, antimicrobial PDT can be a handier treatment modality against SARS-CoV-2. Therefore, many research groups worldwide have been exploring PDT as an alternative mode of treatment.

In December 2020, Weber et al. studied the efficacy of riboflavin-5-phosphate as the PS on 20 COVID-positive patients with symptoms like fever, cold, dry cough, fatigue, breathing problem, headaches, etc. The patients were treated with two riboflavin-5-phosphate capsules along with their meals. Then, riboflavin solution was sprayed into their nostrils. After 15 min, UVA light was shone through the nose, throat, and mouth for 10–20 min. After 5 days, 14 out of 20 patients showed remarkable improvement both in terms of clinical symptoms and viral load calculations.

Loktev et al. reported promising viral inhibition using methylene blue and radachlorin.[3] They treated Vero E6 cells infected with SARS-CoV-2 with 662-nm laser light (of energies 16 and 40 J/cm^2) in the presence of methylene blue and radachlorin separately. The tissue culture results revealed a substantial decrease in infection. The antiviral activities were also studied using MTT-assay; the CC_{50} values of methylene blue (100 g/mL) were found to be almost double that of radachlorin (50 g/mL). The probable reason for these PSs showing effective virus inhibition was thought to be the interference in the interaction between the SARS-CoV-2 spike proteins and the ACE2 receptors.

BX-1, a methylene blue derivative, also showed promising results against SARS-CoV-2 upon irradiation with 630-nm light for just 2 min.

Apart from these, there are many other ongoing studies with different PSs like Rose Bengal, phthalocyanine derivatives, etc.

Conclusion:

To summarize, this article focuses on opening newer avenues for COVID-19 treatment. Herein we discuss the benefits of PDT as an effective treatment modality against COVID-19 owing to its non-invasive nature and site-specificity. Since the mechanism of PDT is independent of the specific genomic nature, it can be applied to different variants of SARS-CoV-2. The conditions for a suitable PS, which can enable the researcher to design novel PSs for better viral inhibition efficacy, is also discussed. There have been reports on the application of antimicrobial PDT to treat COVID-19, and the mechanistic details also need to be elucidated in detail; however, the history of PDT against RNA viruses strongly supports the probability of it being a promising alternative for COVID-19 treatment.

References:

1. (a) Kotra, L. P.; Infect. Dis. 2007, 1–2; (b) Call to Action on Antimicrobial Resistance (AMR), WHO, 2021.
2. Anas, A.; Sobhanan, J.; Sulfiya, K. M.; Jasmin, C.; Sreelakshmi, P. K.; Biju, V. J. Photochem. Photobiol. C. 2021, 49, 100452-100469.
3. Ion, R.-M. Coatings. 2021, 11, 393.
4. Allison, R. R.; Downie, G. H.; Cuenca, R.; Hu, X. H.; Childs, C. J. H.; Sibata, C. H. Photodiagn. Photodyn. Ther. 2004, 1, 27–42.
5. Alvarez, M. G.; Vittar, N. B. R.; Principe, F.; Bergesse, J.; Romanini, M. C.; Romanini, S.; Bertuzzi, M.; Durantini, E. N.; Rivarola, V. Photodiagn. Photodyn. Ther. 2004, 1, 335–344.
6. Kharkwal, G. B.; Sharma, S. K.; Huang, Y. Y.; Dai, T.; Hamblin, M. R. Lasers Surg. Med. 2011, 43, 755–767.
7. (a) Lavie, G.; Mazur, Y.; Lavie, D.; Meruelo, D. Med. Res. Rev. 1995, 15, 111–119; (b) Smetana, Z.; Malik, Z.; Orenstein, A.; Mendelson, E.; Ben-Hur, E. Lasers Surg. Med. 1997, 21, 351–358;
8. Foote, C. S. Oxygen Oxy-Radic. Chem. Biol. 1981, 425–440.
9. (a) Kipshidze, N.; Yeo, N.; Kipshidze, N. Nat. Photonics 2020, 14, 651–652; (b) Baptista, M. S.; Cadet, J.; Di Mascio, P. D.; Ghogare, A. A.; Greer, A.; Hamblin, M. R.; Lorente, C.; Nunez, S. C.; Ribeiro, M. S.;

Thomas, A. H.; Vignoni, M.; Yoshimura, T. M. Photochem. Photobiol. 2017, 93, 912–919.

10. Islam, R.; Parves, M. R.; Paul, A. S.; Uddin, N.; Rahman, M. S.; Mamun, A. A.; Hossain, M. N.; Ali, M. A.; Halim, M. A. A Molecular Modeling J. Biomol. Struct. Dyn. 2020, 1–12;

11. Hudson, J. B.; Delaey, E.; de Witte, P. A. Photochem. Photobiol. 1999, 70, 820–822;

12. Bhapkar, S.; Kumbhar, N.; Gacche, R.; Jagtap, S.; Jadhav, U. Biointerface Research in Applied Chemistry, 2021, 11, 12808-12830;

13. Conrado, P. C.V.; Sakita, K. M.; Arita, G. S.; Galinari, C. B.; Gonçalves, R. S.; Lopes, L. D. G.; Lonardoni, M. V. C.; Teixeira, J. J. V.; Bonfim-Mendonça, P. S.; Kioshima, E. S. Photodiagnosis and Photodynamic Therapy, 2021, 34, 102221-10243.

The Chemistry of Hand Sanitisers and its role as first line of defense against SARS-CoV-2:

✎ *Dr. Suman Samai*

Department of Chemistry, Prabhat Kumar College, Contai, West Bengal-721404, India.

E-mail: suman2iit@gmail.com

Introduction:

The emergence of the COVID-19 (Coronavirus Disease-2019) pandemic has risen to be a significant global public health concern and led to extensive use of hand disinfectants. The recent study reveals that transmission of SARS-CoV-2 is possible in the form of aerosol and fomite, and the virus can remain viable and infectious in aerosols for hours and on surfaces up to days, depending on the inoculum shed.[1] Hence, it is crucial to interrupt the transmission chain of the virus through contact isolation and strict infection control tools.[2] Hand sanitizing products used in the outbreak of the novel coronavirus known as COVID-19 are in great demand. The U.S. Centres for Disease Control and Prevention (CDC) "recommends washing hands with soap and water whenever possible because hand washing reduces the amounts of all types of germs and chemicals on hands. But if soap and water are not available, using a hand sanitizer with at least 60% alcohol can help you avoid getting sick and spreading germs to others."[3] Hand disinfectants are commercially available in various types and forms (Figure-1) such as anti-microbial soaps, water-based or alcohol-based hand sanitizers, most often used in hospital settings. The World Health Organization (WHO) recommends alcohol-based hand sanitizer (ABHS) in line with the proven advantages of their rapid action and a broad spectrum of microbicidal activity offering protection against bacteria and viruses.
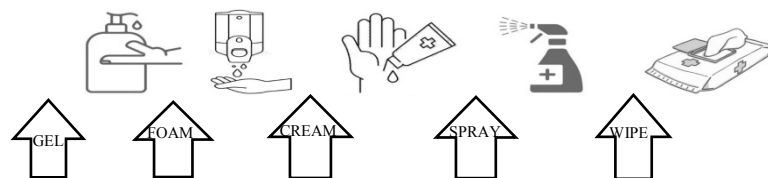
Hand sanitizer-formulation

Figure-1: Various types of hand sanitizer dosage forms

Chemical composition of hand sanitizers:

The use of hand sanitizer is recommended when soap and water are not available for hand washing or when repeated hand washing compromises the natural skin barrier. Studies show that sanitizers with an alcohol concentration between 60–95% are more effective at killing disease causing microorganisms such as the coronavirus than those with a lower alcohol concentration or non-alcohol-based hand sanitizers.[4] To make our hand disinfected several antimicrobial compounds have been utilized in the formulation of hand sanitizer.[5] The alcohols, namely ethanol and isopropanol, are most commonly used for skin disinfection due to their broad activity against bacteria, viruses and fungi.[6] There is another drawback for ethanol and isopropanol. They can dry our skin. To counter this effect, glycerol, a type of alcohol, is added in hand sanitizers. Chemically speaking, glycerol is also an alcohol, but it's not added in solutions/disinfectants to kill germs. Rather, it is added to increase the thickness of the solution. This makes it more potable and easier to use. Some brands also add to copherol, an alcohol rich in Vitamin E and is good for the skin. Colours and fragrances can be added as well.

WHO formulations for hand disinfection:
The WHO has recommended different alcohol-based hand sanitizer formulations which differ only in their alcohol constituent. Recently, the United States Pharmacopeia (USP) Compounding Expert Committee (CMP EC) recommends the three formulations for compounding alcohol-based

hand sanitizers for use during shortages associated with the COVID-19 pandemic and listed in the following table.[7]

Table-3: Formulation composition for compounding alcohol-based hand sanitizer (ABHS) based on USP and WHO recommendations

Components	Formulation 1: Ethanol Antiseptic 80% Topical Solution	Formulation 2: Isopropyl Alcohol Antiseptic 75% Topical Solution	Formulation 3: Isopropyl Alcohol Antiseptic 75% Topical Solution
Ethanol 96%	833.3 mL		
Isopropyl Alcohol 99%		757.6 mL	
Isopropyl Alcohol 91%			824.2 mL
Hydrogen Peroxide 3%	41.7 mL	41.7 mL	41.7 mL
Glycerol 98%	14.5 mL	7.5 mL	7.5 mL
Water *, sufficient quantity to make	1000 mL	1000 mL	1000 mL

*Water may be distilled water, cold boiled potable water, reverse osmosis water, or filtered water.

Chemistry of virucidal action of hand sanitizers:

With the help of plethora of information available in different from the basic structure of SARS-CoV-2 is well known. SARS-CoV-2 is relatively large in size (0.12 μm) and characterized by the presence of highly glycosylated spikes on the protein membrane in a crown-like arrangement, hence the name, Corona (Figure-2). It has a single-stranded positive-sense RNA genome of 29891 nucleotides. The glycosylated spike protein binds to the host angiotensin converting enzyme-2 (ACE-2) protein which servesas a functional receptor for entry into host respiratory cells.
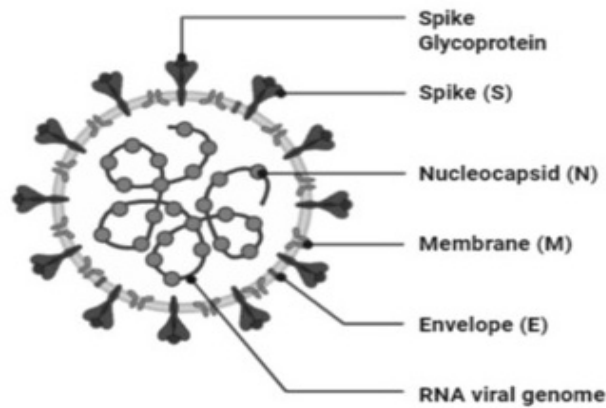
Figure-2: Structure of of SARS-CoV-2

It has been mentioned earlier that the alcohols, namely ethanol and isopropanol, are most commonly used for skin disinfection due to their antimicrobial property.[6] Their mode of action against enveloped viruses is shown in Figure 3. Dissolution of lipid membrane and denaturation of protein are the two key mechanisms of the antimicrobial action of ethanol, which is leading to the disruption of membrane and inhibition of metabolism.[8,9]

Alcohols are amphiphilic compounds, as they possess both hydrophilic and lipophilic (hydrophobic) properties that facilitate their entry through the viral envelope. The outermost membrane of SARS-CoV-2 comprises lipids bound together by an alkane chain of hydrophobic fatty acids. Contact of the virus with an alcohol leads to alteration in its membrane fluidity.[10] The presence of polar oxygen atoms weaken the lipophilic interactions between the non-polar residues, and increase the internal affinity of the membrane for water, thus destabilizing and denaturing the protein structure.
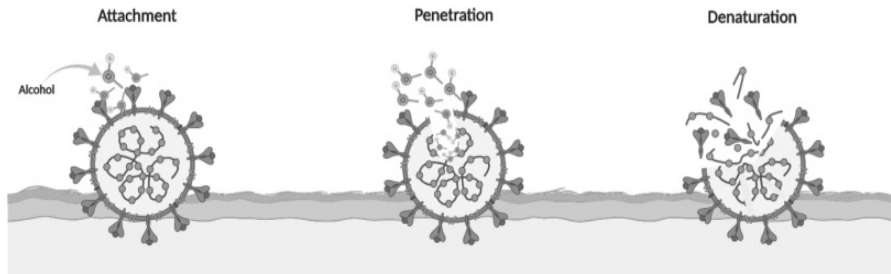
Figure-3: Antiviral mechanism of action of alcohol against enveloped viruses.

The antimicrobial mechanism of alcohol against enveloped viruses is similar to that for bacteria as both have a lipid-rich outer membrane. Non-enveloped viruses are relatively more resistant to this mechanism due to the lack of a lipid membrane.

Factors influencing the effectiveness of sanitizers against SARS-CoV-2:

The virucidal efficacy of hand sanitizers depends on several factors.[11] The key factors which determine the overall efficiency of alcohol based hand sanitizers against SARS-CoV-2 are as follows.

      Formulation
      Volume and contact time
      Excipients
      pH
      Dirt and soil contamination

Detail discussions on these factors are beyond the scope of this article. One can have all these data on several literatures.

Conclusion:

Hand hygiene by washing hands with soap and water or with alcohol-based hand sanitizers are primary preventive measures against the spread of SARS-CoV-2. The use of alcohol based hand sanitizer is becoming more common because of their rapid action and efficiency in killing microorganisms, mainly when handwashing using soap and water is not practical or convenient. It is vital to select alcohol based hand sanitizer with the appropriate amount of alcohol and practice the correct hand hygiene technique when cleaning hands to ensure all the microorganisms are effectively killed.

References:

1. Van Doremalen, N.; Bushmaker, T.; Morris, D. H.; Holbrook, M. G.; Gamble, A.; Williamson, B. N.; Tamin, A.; Harcourt, J. L.; Thornburg, N. J.; Gerber, S. I.; N. Engl. J. Med. 2020, 382, 1564–1567.
2. Thomas, Y.; Boquete-Suter, P.; Koch, D.; Pittet, D.; Kaiser, L.; Clin. Microbiol. Infect. 2014, 20, O58–O64.
3. Centers for Disease Control and Prevention. Available online: https://www.cdc.gov/coronavirus/2019ncov/prepare/prevention.html
4. Dixit, A.; Pandey, P.; Mahajan, R.; Dhasmana, D. C. Res. J. Pharm. Biol. Chem. Sci. 2014, 5, 558–563.
5. WHO Guidelines on Hand Hygiene in Health Care (Advanced Draft) Global Patient Safety Challenge 2005–2006. (2009). Clean Care is Safer Care, 2009. Geneva, Switzerland: WHO Press. Available at https://www.who.int/patientsafety/information_centre/Last_April_versionHH_Guidelines%5B3%5D.pdf.
6. Kampf, G.; Todt, D.; Pfaender, S.; Steinmann, E. J. Hosp. Infect. 2020, 104, 246–251.
7. Compounding Expert Committee. Compounding Alcohol-Based Hand Sanitizer during COVID-19 Pandemic. Available online:https://www.usp.org/sites/default/files/usp/document/about/public-policy/usp-covid19- handrub.pdf
8. Gerberding, J. L.; Fleming, M. W.; Snider, D. E., Jr.; Thacker, S. B.; Ward, J. W.; Hewitt, S. M.; Wilson, R. J.; Heilman, M. A.; Doan, Q. M. Recommendations of the Healthcare Infection Control Practices

Advisory Committee and the HICPAC/SHEA/APIC/IDSA Hand Hygiene Task Force; Centers for Disease Control: Atlanta, GA, USA, 2002; Volume 51.

9. Centers for Disease Control and Prevention. Hand Hygiene in Healthcare Settings; Centers for Disease Control and Prevention: Atlanta, GA, USA, 2019.

10. Ingram LO; Adaptation of membrane lipids to alcohols. Journal of Bacteriology 125, 1976, 670.

11. Singh, D.; Joshi, K.; Samuel, A.; Patra, J. and Mahindroo, N. Epidemiology and Infection 148, e229, 1–9.

CHAPTER

12

Arsenic in the Environment and its Effects on Human Body

✎ *Dr. Arpita Biswas*

Department of Chemistry, Shibpur Dinobundhoo Institution (College), Howrah, West Bengal-711102, India

E-mail: abiswas83@gmail.com

Introduction:

Arsenic is a chemical element of atomic number 33 symbolize as As. The element was discovered by alchemist Albert the Great (Albertus Magnus) in 1250 A. D. It is a brittle steel-grey metalloid i.e. having properties of both metals and non-metal. When heated, Arsenic does not melt, as most solids do but it changes directly into a vapor (gas). This process is known as sublimation. However, under high pressure, arsenic can be forced to melt at about 814°C (1,500°F). Arsenic has a density of 5.72 grams per cubic centimeter. When heated in air, arsenic combines with oxygen to form arsenic oxide (As_2O_3). A blue flame is produced, and arsenic oxide can be identified by its distinctive garlic-like odor. It exists mainly in allotropic forms: Yellow, black and grey; the stable form is a silver-gray, brittle crystalline solid. In its pure form, arsenic is a gray-colored, odorless, and tasteless metal. Arsenic may be inorganic arsenic when combined with elements other than carbon, or organic, when combined with elements other than carbon.

Occurrence in Nature:

Arsenic rarely occurs as a pure element. It is usually found as a compound. The most common ores of arsenic are opiment (As_2S_3), realgar (As_4S_4) and arsenopyrite (FeAsS). These compounds are obtained as a by-product of the mining and purification of silver metal.

1. Natural sources of environmental arsenic: It is found in nature in rocks, soils, groundwater, surface water, air, and some foods. Arsenic is present in more than 200 mineral species, the most common of which is arsenopyrite. It has been estimated that about one-third of the atmospheric flux of arsenic is of natural origin. Volcanic action is the most important natural source of arsenic, followed by low-temperature volatilization. Inorganic arsenic (when combined with elements other than carbon) of geological origin is found in groundwater used as drinking-water in several parts of the world, for example Bangladesh. Organic arsenic compounds (when combined with carbon) such as Arsenobetaine, Arsenocholine, tetramethyl-arsonium salts, Arsenosugars and Arsenic-containing lipids are mainly found in marine organisms although some of these compounds have also been found in terrestrial species.[1,2]

2. Man-made sources of environmental arsenic: Arsenic trioxide is a by-product of metal smelting operations. About 70% of the world production of arsenic is used in timber treatment, 22% in agricultural chemicals, and the remainder in glass, pharmaceuticals and metallic alloys. Mining, metal smelting and burning of fossil fuels are the major industrial processes that contribute to arsenic contamination of air, water and soil. Elemental arsenic is produced by reduction of arsenic trioxide (As_2O_3) with charcoal. As_2O_3 is produced as a by-product of metal smelting operations.[2]

3. Environmental transportation and its distribution: Arsenic is emitted into the atmosphere by high-temperature processes such as coal-fired power generation plants, burning vegetation and volcanism. Natural low-temperature biomethylation and reduction to arsines also releases arsenic into the atmosphere. Arsenic is released into the atmosphere primarily as As_2O_3 and exists mainly adsorbed on particulate matter.[2]

Sources of Exposure:

The primary routes of arsenic exposure into human body are via ingestion and inhalation. Dermal exposure can occur, but is not considered as a primary route of exposure. Main sources of arsenic exposure via ingestion

occur from: Contaminated drinking water, grains cultivated in contaminated soil and also from some arsenic containing food such as shellfish, meat and poultry. Major sources of inhaled arsenic may come from air emission from burning of fossil fuel that contain Arsenic, glass manufacturing operations, pesticide manufacturing facilities, smelters and tobacco smoking. Dermal exposure of arsenic occurs during handling of arsenic containing product such as rat poison, wood preservative etc.[2-6]

Thereshold Limit of As Exposure in Human Body:
The threshold limit of arsenic exposure in human body is 10–20 g and permissible upto 50 g.[2-5]

Effects in Human Body:

1. Absorbtion: Most ingested and inhaled arsenic is well absorbed through the gastrointestinal track and lung into the blood stream. After absorption through lungs and the gastro-intestinal tract, 95 to 99% of the arsenic is located in erythrocytes, bound to the globins of hemoglobin and is then transported to the other parts of the body.

2. Distribution: Arsenic is transported by blood which distributes it to muscles, bones, kidneys, lungs and larger amounts are concentrated in keratin-rich tissues such as skin nails and hair.

3. Metabolism and detoxification: Methylation is considered the main route of arsenic detoxification. Metabolism of inorganic arsenic involves a two electron reduction of pentavalent arsenic to trivalent arsenic, mediated by glutathione, followed by oxidative methylation to form pentavalent organic arsenic. Although a percentage of arsenite is methylated in the liver by enzymatic transfer of the methyl group from SAM (S-adenosyl methionine) to methyl arsenate and dimethyl arsenate producing monomethyl arsenic acid and dimethyl arsenic acid. When methylating capacity of the liver is exceeded, exposure to excess levels of inorganic arsenic results in increased retention of arsenic in tissues. Recently additional detoxification

mechanisms are suggested.[5-7]
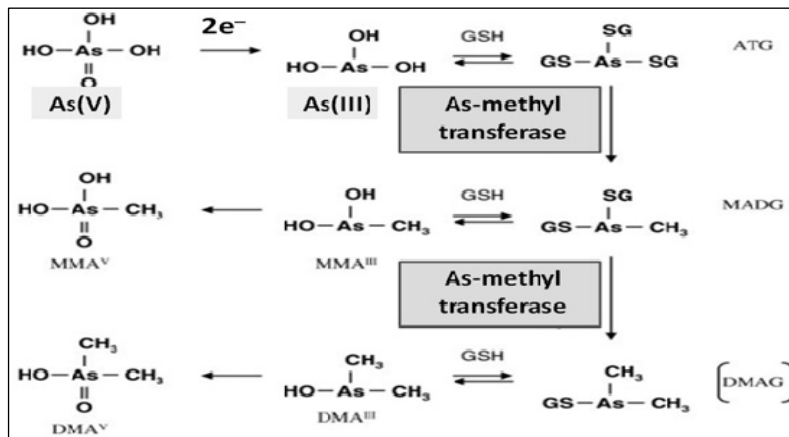
Scheme-1: Metabolism pathway of arsenic by electron transfer and methylation.

4. Excretion: About 70% of the arsenic is excreted mainly through urine. Most arsenic absorbed into the body is converted by the liver to less toxic methylated form that is efficiently excreted in the urine. Some of the inorganic arsenic is excreted primarily via urine as the parent form of the ingested arsenic. After methylation, it is also excreted as monomethyl-arsonous acid (MMA) and dimethyl-arsinous acid (DMA). Humans rapidly excrete most blood arsenic, with 50 to 90% cleared in two to four days. The remainder is cleared more slowly.[5]

Toxicity:

As^{III} is 60 times more toxic than As^V. Organic arsenic is non-toxic whereas inorganic arsenic is toxic. Arsenite (trivalent arsenic) and Arsenate (pentavalent arsenic) have different fates in the human body. Biologically the trivalent arsenite are more reactive than pentavalentarsenate. Majority of arsenic enters into the human body in the trivalent inorganic form As(III) via the phosphate carrier system. It can bind to polyphosphates like adenosine diphosphate after that it is rapidly hydrolised. Small amout of pentavalent inorganic arsenic can cross cell membranes via an energy dependent

transport system, after which it is immediately reduced to trivalent arsenic. Arsenite can bind to thiols such as gluotathione and thiol containing protein.[7]

1. Toxicity of trivalent arsenic:

i) Arsinite react with glicoraldehyde-3-phosphate to form 1-arseno-3-phosphoglycerate which resembles glucose-6-phosphate and thus inhabit the activity of hexokinase thereby further production of acetyl pyruvate.[7,8]
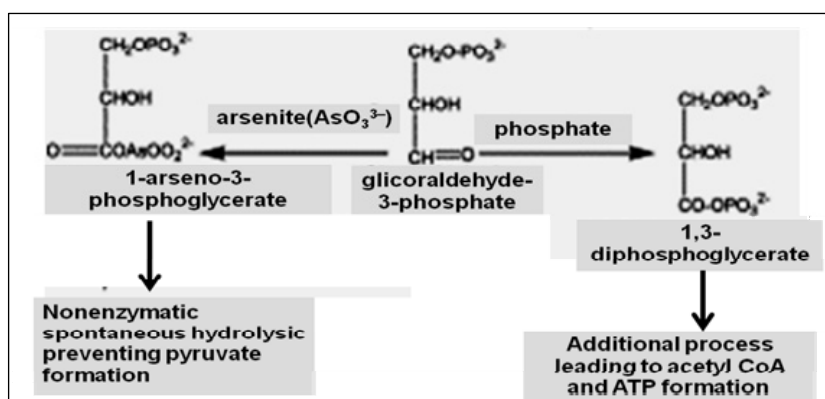
Scheme-2: Formation of 1-arseno-3-phosphoglycerate in presesence of arsenite (AsO$_3^3$).

ii) Inhibits pyruvate dehydrogenation due to the binding of SH groups of dihydrolipoamide, resulting in a reduced conversion of pyruvate to acetyl coenzyme (CoA).[10]
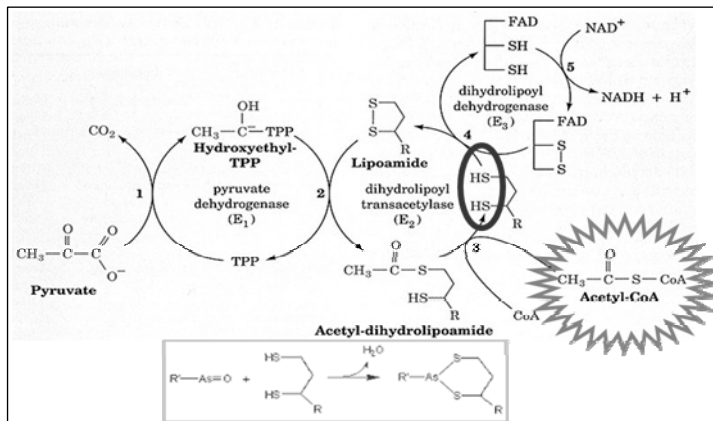
Scheme-3: Binding of SH group of dihydrolipoamide in presence of arsenite (AsO_3^3).

iii) Blocks citric acid cycle activity and interrupt oxidative phosphorilation and production of cellular ATP are decreased.
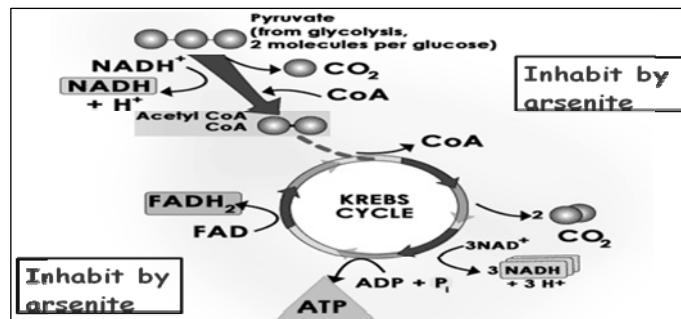
Scheme-4: Krebs cycle that inhibited by Arsenite and decrease production of cellular ATP.

2. Toxicity of pentavalent arsenic:

Toxicity of pentavalent inorganic arsenic is due to its conversion to trivalent arsenic. Uncoupling of oxidative phosphorylation occurs because the normal high energy phosphate bonds are not formed; e.g. in the presence of pentavalent arsenic, adenosine diphosphate (ADP) forms ADP arsenate

instead of ATP with the absence of the high   energy ATP phosphate bonds. Uncoupling of in vivo oxidative phosphorylation is termed as arsenolysis. Mimic phosphate in in-vivo system can replace phosphate in the sodium pump and the anion exchange transport system. Pentavalent arsenic can form ester with glucose and gluconate forming glucose-6-phosphate and 6-phosphogluconate thus inhabit the formation of pyruvate.[7]

ADP + Phosphate + Energy   **ATP**   Enzymatic Hydrolysis
ADP + Phosphate + Useful energy

ADP + Phosphate + Energy   **ATP**   Spontaneous Hydrolysis
ADP + Phosphate + No useful energy
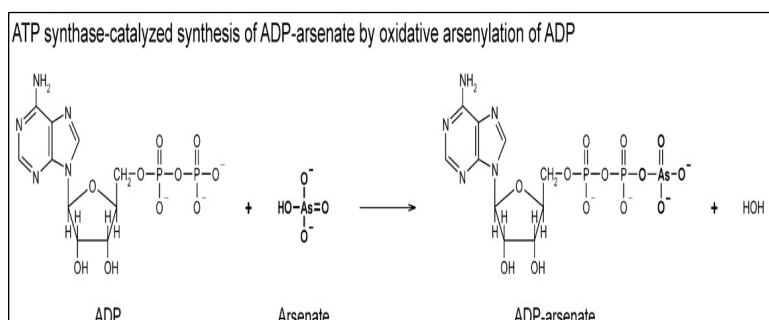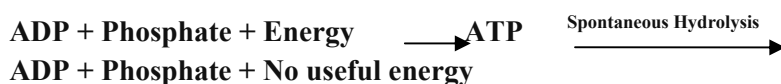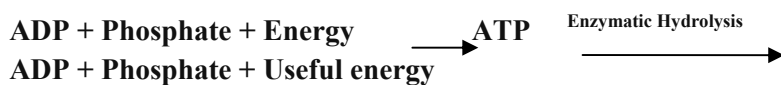
Scheme-5: Arsenolysis of ADP by arsenate.

Symptoms of Arsenic Poisoning:
1. Major effects of acute arsenic poisoning in human body includes
i) darkening of skin (hyperpigmentation) in areas that are not exposed to sunlight.

ii) Excessive formation of scaly skin on the palms and soles.

iii) Transverse white bands of arsenic deposits across the bed of the fingernails (Mee's lines).

iv) Mouth produces excess saliva, loss of hair, breath smells like garlic, excessive sweating and red eye.

v) Gastrointestinal discomfort such as nausea, vomiting and abdominal pain. Headache, drowsiness, distal weakness of small muscles e.g. hands and feet.
vi) Hemolytic anemia, Leukopaenia, Proteinuria.[1, 4-6]

2.   Major effects of chronic arsenic poisoning in human body includes
i) Irritation of skins and mucous membranes, fatigue and loss of energy.
ii) Chronic arsenic poisoning also results kidney degeneration, bone-marrow degeneration, cirrhosis of liver and severe dermatitis.
iii) Long-term complication of chronic arsenic poisoning results Bowen's disease.[2-4, 6]

Treatment:

Chelating agents are organic compounds capable of linking together metal ions to form complex ring like structure called chelates. Chelating agents have been used clinically as antidotes for acute and chronic arsenic poisoning. Chelators not only enhance excretion but also decrease the clinical signs of toxicity by preventing metals from binding to cellular target molecues. Chelators form a complex with the respective toxic ions and these complexes reveal a lower toxicity and more easily eliminated from body. It includes 2,3-dimercaprol (British Anti Lewisite, BAL), sodium 2,3-dimercaptopropane-1-sulfonate (DMPS), meso 2,3-dimercaptosuccinic acid (DMSA).
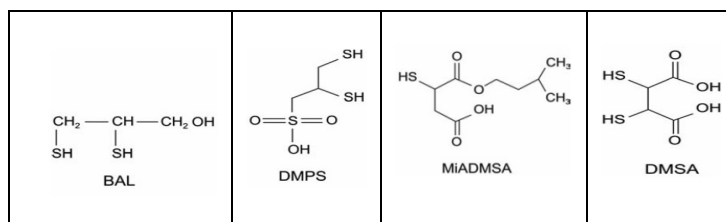
Figure-1: Chemical structures of some common chelating agents used against arsenic poisoning.

Most of the chelating agents however, suffer from serious side effects. Meso 2,3-dimercaptosuccinic acid (DMSA) is found to be one of the least toxic drugs that could be given orally. However hydrophilic and

lipophobic properties of DMSA do not allow it to pass through cell membrane. Recently some mono and diaters of DMSA especially the higher analogous have been developed and tried against cases of experimental arsenic poisoning in invitro and invivo both. MiADMSA is a monoester of DMSA with a straight and C-5 branched chain amyl group thereby increasing the lipophilicity and number of carbon atoms of the compound. Due to its lipophilic nature it can easily cross the cell membrane and chelate arsenic from intracellulary and extracellilarly both. This is the best theraputic part of this chelating agent.

Apart from synthetic chemical chelators, studies have been carried out to explore natural antioxidants against the toxic elements. There is a wide range of antioxidants which can offset the condition of oxidative stress. It includes vitamins, phenolic compounds (flavonoids), carotenoids, hormones (melatonin, estradiol and insulin). In addition, minerals such as selenium, zinc.
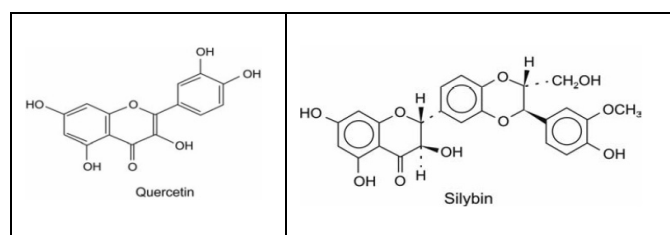
Figure-2: Chemical structure of quercetin and silybin used as anitioxidant against arsenic poisoning

Quercetin is one of the most frequently studied dietary flavonoids and is ubiquitously present in various vegetables, fruits, seeds, nuts, tea and red wine. It has been shown to have very potent antioxidant and cytoprotective effects in preventing endothelial apoptosis caused by oxidants. In addition, quercetin is a more potent antioxidant than other antioxidant nutrients, such as vitamin C, E and β-carotene on molar basis. Silymarin is also a polyphenolic antioxidant flavonoid widely found in vegetables sources. The potential role of oxidative stress in pathogenesis induced by arsenic suggests that antioxidants can be considered as an

alternative approach in mitigating arsenic induced toxicity. Silymarin has been proved to be effective in restorive the diminished level of antioxidants against arsenic induced toxicity in vitro. The possible mechanism underlying the protective properties of silymarin includes prevention of GSH depletion, destruction of free radicals. Chemical structure of quercetin and silymarin are shown in Figure-2.

Researchers have also reported moderate chelating and antioxidant properties of Moringaoleifera, Centellaasiatica and Aloe vera against arsenic during concomitant administration. These naturally occurring herbal products known to possess an effective arsenic removal property, either individually or in combination for the treatment of chronic toxicity.[2,9,10]

Conclusion:

In this chapter I tried to elaborate briefly different sources of environmental arsenic, effects of arsenic in human body, toxicity of trivalent and pentavalent Arsenic, symptoms of Arsenic poisoning and its treatment. Furthermore, activity inhabitation of hexokinase by arsinite, pyruvate dehydrogenation inhabitation due to the binding of SH groups of dihydrolipoamide by arsinite, citric acid cycle activity blocking, oxidative phosphorilation interruption have been illustrated. Apart from arsenic poisoning in human body the treatment of arsenic poisoning by different chelators like BAL, DMPS, MiADMSA, DMSA and antioxidant like quercetin and silybin have been discussed. Thus the basic and essential labors for the reduction of chronic arsenic toxicity are prevention which is always a best way as prevention is better than cure. Therefore, it is recommended to use alternative water source such as rainwater or to remove the arsenic from contaminated water, to reduce arsenic containing chemical in agriculture and to reduce industrial process that contribute to arsenic contamination of air, water and soil.

References:

1. B. A. Fowler, J. B N. Weissberg, Engl. J. Med. 1974, 22, 1171.
2. S. Kapaj, H. Peterson, K. Liber, P. Bhattacharya, J. Env. Sci. and Health, Part A, 2007, 41, 2399.
3. S. J. S. Flora, A. Mehta, R. Gupta, Chem. Biol. Int., 2009,177, 227.
4. J. C. Saha, A. K. Dikshit, M. Bandhopadhyay, K. C. Saha, Crict. Rev. Env. Sci. Tech., 2010, 29, 281.
5. N. Singh, D. Kumar, A. P. Sahu, J. Env. Biol., 2007, 28, 359.
6. S. Chouhan, S. J. S. Flora, Indian J. Expt. Biol., 2010, 48, 666.
7. D.N. G. Mazumder, Indian J. Med. Res., 2008, 128, 436.
8. J. B. Vigo, J. T. Ellzey, Tex. J. Microscopy, 2006, 37, 45.
9. M.F. Hughes, Toxicol. Let., 2002, 133, 1.
10. K. S. M. Abdul, S. S. Jayasinghe, E. P. S. Chamndana, C. Jayasumana, P. M. C. S. Silva, Env. Toxi. Pharmacol., 2015, 40, 828.

CHAPTER

13

Cloudburst: A Natural Disaster over Indian Sub-continent

✎ *Semanti Das*

Department of Geography, Chandrakona Vidyasagar Mahavidyalaya, Paschim Medinipur, W. B.-721201, India

E-mail: semantidas@chandrakonavm.ac.in

Introduction:

Cloudburst is a frightening phenomenon in the Himalayan mountainous region as one of the frequent natural disasters in India. These are reported as frequent natural disaster in the Indian Himalayas for the recent past. According to the India Meteorological Department (IMD), a cloudburst features very heavy rainfall over a localized area at a very high rate of the order of 100 to 1000mm per hour featuring strong wind and lightning. The Cloudburst events have further been classified into two types, one is associated with heavy rainfall in the steep slope mountainous regions of Himalayas identified based on flash floods and damages to properties and casualties, irrespective of the rainfall amount. Another events are associated with rainfall >10 cm/hour as per the definition provided by the India Meteorological Department (IMD).[1] Various researches suggest that they are manifestations of intense vortices on small scale that generate strong convection currents, which lift the moisture laden air with sufficient rapidity to form cumulonimbus clouds. The copious rainfall characteristic is caused by a phenomenon known as Langmuir Precipitation process, in which drops of rain coalesce together at almost lightning speed to create larger and larger sized drops. As they grow more and more in size, they fall quicker and quicker. Change in climate due to Global warming is the major concern for glacial melting that helps to increase the volume of cloud, which ultimately accelerates the process of Langmuir Precipitation. In India, cloudbursts usually occur during the monsoon season over orographically dominant

regions like the Himalayas and the Western Ghats. These can also occur over the plains, but such occurrences are rare.

It is believed that cloudburst occur because of rapid lifting of clouds by the steep orography of the region. This process is called the "Cumulonimbus Convection condition". This lifting is usually dynamic, causes thermodynamic instability resulting in rapid condensation. In Himalayan region the soil moistened by earlier precipitation perhaps acts as an additional source of moisture might also have a role in the frequent cloudbursts in the region.[2] Dimri et al. reported a review[3] that most of the Cloudburst events occurred in the elevation range of 1,000–2,500 meters of the Western Himalaya. They concluded that strong convection associated with orographic forcing over the Himalaya favours the formulation of Cloudburst. According to IMD scientists, the cloudburst in Leh occurred due to an unusual movement of monsoon cloud. Analysis of satellite imageries indicate that the intense convective system developed in the easterly current associated with monsoon conditions over the region. The convective cloud band extending from southwest to northeast developed over Nepal and adjoining India.[4]

In Uttarakhand, Extraterrestrial influence leads to rise in temperature to release the aerosol trapped in the glaciers and atmosphere in Indo China border to initiate the cloudburst in 2013.[5] Himalayan Glaciers have been in a general state of recession since a long time. As per the report "Snow and Glaciers of the Himalayas: Inventory and Monitoring" released by the Ministry of Environment and Forests (MOEF) in 2011, out of 2700 glaciers which are monitored 2184 are retreating, 435 are advancing and 148 glaciers show no change. Existing studies of Himalayan glaciers indicate that many have exhibited an increased receding trend over the past few decades.[2] The main objectives of the present study are i) to assess and review the past cloudburst events and their impacts on inhabitants of the area, ii) to find out possible causes of cloudbursts, on the basis of the previous research.

Materials and Methods:
Relevant research concerning mechanism of cloud burst was identified by searching the literature or article reviews published in different peer review

journals during a period of last two decades for primary research material. Finally, a comprehensive search was made of Internet resources in India and Internationally. The next step was a detailed examination of articles, and at this point studies were excluded if phenomena were insufficiently described. For the studies investigating direct associations between cloud formation and burst, the review includes all peer reviewed longitudinal studies investigating mechanism behind it. Longitudinal studies were seen as a particularly valuable resource as they facilitate the testing of relationships between early events or characteristics and later outcomes, and enable the identification of developmental sequences and pathways, as well as the construction of theoretical models which can then be validated in future research. Data were statistically analyzed using SPSS (PASW Statistics 18.0.0) software. However, due to the limited volume of published studies, quantitative and qualitative studies and their comparisons were not done satisfactorily, but attempts were made to elucidate direct possible mechanism behind their formation wherever possible.

Results and Discussion:
Cloudburst and Thunderstorm:
Cloudburst is formed from mature stage of thunderstorm. Precipitation from the mature storm is intense and composed of large raindrops, literally known as cloudburst (Figure-1**)**.
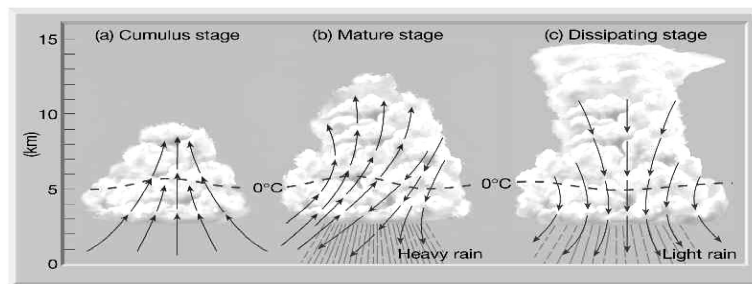
Figure-1: Stages of Thunderstorm Development[6]

The common process that initiate thunderstorm development are-
➢ heating and convection in moist air over warm land surfaces;
➢ passage of cold, moist air over warm water;

➢ forced ascent of conditionally unstable air along zones of convergence or at mountain barriers;

➢ radiational cooling at upper levels;

➢ advection of cold air aloft.

In case of tropical thunderstorm water droplets cannot reach the freezing level, hence they reach the surface as cloudburst formation.

Principal rain bearing meteorological systems that lead to short duration heavy rainfall and which may also cause floods are:

✓ monsoon depressions;

✓ fluctuations in the intensity and location of the monsoon trough over the plains of India;

✓ a mid-troposphere circulation or low pressure off the coasts of India particularly over Gujarat;

✓ off shore vortices;

✓ cumulonimbus convection in condition;

✓ moist thermodynamic instability.

Apart from these, land based lows or depressions during monsoon cyclones and persistence of low pressure areas over adjoining coastal areas may sometimes lead to floods. Hilly areas in Himachal Pradesh, Uttarakhand, he northern areas of West Bengal, Sikkim, Arunachal Pradesh, Manipur, Mizoram, Meghalaya, Nagaland and Tripura and the coastal areas in the states of West Bengal, Orissa, Andhra Pradesh, Tamil Nadu, Karnataka, Kerala, Maharashtra and Gujarat and Union Territories (UT's) of Andaman and Nicobar Islands and Lakshadweep are more prone to such phenomena. Such events have also occurred in the states of Rajasthan, Chattisgarh, Madhya Pradesh and Uttar Pradesh.

Cloudburst and Langmuir precipitation: Since the cloudbursts are associated with cumulonimbus clouds, where the upper part of the cloud exceeds freezing level and precipitation process remains under Bergeron-Fiendeisen's chain reaction domain, the lower part of the same cloud under favorable condition becomes a prey of Collision-Coalescence chain reaction domain.

Collision-Coalescence process is the process that explains the growth of raindrops or precipitation particles. Collision-Coalescence ideas

were put forward by George Simpson and Mason. These ideas were modified by Langmuir. He pointed out that the terminal velocities of falling drops are directly related to their diameters. Drops that have grown on larger condensation nuclei become larger. The larger drops will have a higher terminal velocity than the smaller ones and so collide with them. When the collecting drop (the larger one) is 60 microns in diameter, its collection efficiency is about 50 percent, but it is only about 10 percent at 40 microns and less than 5 percent at 30-microns. The collection efficiency is said to be 100 percent when the drop collects all the droplets in its direct path. Thus, when both the collection efficiency and the fall rate of the droplets and crystals are taken into consideration it is found that coalescence is almost nil until the droplets or crystals exceed 40 microns (Figure-2).
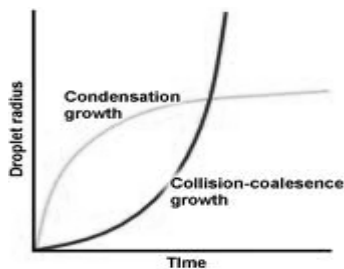
Figure-2: Droplet Growth by Condensation and Coalescence[7]

Once the collecting particles are larger than this, coalescence proceeds so rapidly that raindrops would often be far larger. If they did not break apart once they exceeded a few millimeters in diameter. Even with collision, growth will only occur if the two drops coalesce. This will occur most readily if-

a) the drops are of considerably different sizes, and
b) atmospheric electricity is present to hold the droplets together. If a droplet with a negative charge should collide with a positively charged droplet their electrical attraction will bind them together.

Continued collision, thus leads to coalescence resulting in many large unstable drops which on further disruption produce several large drops and its continued coalescence and further disruption leads to many larger drops.

Case Studies:

There is no particular mechanism stating the formation of cloudburst. Hence mechanisms of recent cloudbursts in the areas of Northern Himalayan regions from India are discussed here as case studies.

Case Study 1: Leh, August 2010:

On August 6, 2010, sudden overnight rains caused flash floods in the town of Leh.

Possible Mechanism: Usually, the western Himalayan region experiences the cloudburst events during the monsoon season in association with the strong monsoon circulation or the interaction of monsoon circulation with the mid-latitude westerly system. The orography of the region plays a dominant role by increasing the convection and hence the intensity of cloudburst. However, Ladakh region is not known to be frequently affected by this type of phenomena. It is a cold desert and average rainfall for the month of August is 15.4 mm only. The highest rainfall ever recorded over Leh during 24 hours period has been 51.3 mm recorded on 22 August, 1933. However in case of Leh cloudburst, the flow from the west or northwest seems to be sufficiently moisture rich following intense convection and flooding in August 2010. The instability trigger seem to have come from the cloud cluster that moved from Nepal region. The cloudburst was highly localised as the nearby meteorological observatory of Indian Air Force (IAF) reported. According to synoptic analysis, the monsoon trough at the mean sea level lay to the south of its normal position on 4th and 5th August. There was a cyclonic circulation in lower levels over west Rajasthan and neighbourhood. A well-marked low pressure area lay over northwest of Bay of Bengal on 5th and over north Orissa and neighborhood on 6th August.[4]

Case Study 2: Kedarnath, Uttarakhand, June, 2013:

Between 16 and 17 June 2013, the hills of Uttarakhand were subjected to intense rainfall-370 millimeters of rainfall was recorded at Dehradun with a 24 hours period, which is exceptionally rare.

Possible Mechanism: The steep orography of Garhwali –Kumaun Himalaya and concentration of monsoon clouds create the situation of cloudburst.

However, there may be some other factors behind this catastrophic event. Climate change manifestation can be seen in the disaster of Kedarnath, Himalaya of India.[6] Himalaya is warming at least twice as fast as the globe. This glacier melt water come in direct contact with clouds due to higher altitude. The temperatures of the glacial lakes are normally below or near the freezing temperature. The saturation vapour pressure over super cooled water remains high so the evaporated water of the lake immediately is being condensed over the cloud and volume of the cloud is increased with time. In 2013, monsoon arrived before the normal time due to extra tropical disturbances which causes high concentrations of clouds in and multiday cloudburst in Kedar Dome and surrounding areas. Due to collusion between two air masses the formation of cumulonimbus cloud generated rapidly.[8]

Case Study 3: Amarnath, Kashmir, July 2015:On July 2015 cloudburst are recurrent in and around Baltal, the base camp for the Amarnath shrine.

Possible Mechanism: Weather scientists say the hilly terrain of the state favours formation of cumulonimbus clouds and the deadly interaction of two different wind patterns leads to shedding of larger droplets of water at a higher rate in a relatively short period. The topography of the state plays a role in making cloudbursts highly localised. Conditions across the Himalayas, including Jammu and Kashmir, are changing and witnessing extreme weather events due to climate change. For the last two years, there has been greater frequency of deadly interaction of moist warm monsoon winds and cool dry western winds called western disturbance, creating a low-pressure area over the state and resulting in extremely heavy rain. According to Sonum Lotus, Director, Indian Meteorological Department, Srinagar, there is no accurate way to predict such an incident like cloudburst.[9]

Normal Precipitation and Cloudburst:
Cloudburst is actually a situation when the inter-molecular forces between the water molecules get very high due to rapid decrease in temperature or excess of electrostatic induction in the clouds causing the lighting to remain inside the cloud only, which causes hyperactive energy inside the cloud. A

chart is given below showing some differences between normal precipitation and cloudburst (Table1).

Table-1: Precipitation Size and Speed

Forms Of Precipitation	Intensity(cm /hour)	Median diameter (millime ters)	Velocity of fall (meters/se cond)	Drops / second /square meter
Drizzle	0.025	0.96	4.1	151
Light rain	1.02	1.24	4.8	280
Moderate rain	0.38	1.6	5.7	495
Heavy rain	1.52	2.05	6.7	495
Excessive rain	4.06	2.4	7.3	818
Cloudburst	10.2	2.85	7.9	1220

Source: Lull, H. W, 1959[10]

From Table 1 it is found out that median diameter of cloudburst is 2.85 millimeters which is equivalent to 2850 microns (as 1mm to 1000 microns). Therefore we can associate coalescence with droplet size in case of cloudburst. A strong positive relationship (R=0.943) was observed between Intensity of Precipitation (cm/hour) and Drops per second per square meter (Table 2). Almost 80% of the variation of Intensity of Precipitation (cm/hour) depends on Drops per second per square meter. The Durbin Watson value (1.711) indicates that positive autocorrelation is detected in the sample.

Table-2: Intensity of Precipitation and Speed after performing Multiple Regression by Stepwise method

Intensity of Precipitation(cm/hour)	Variables taken	Variables included	R	R^2	Sig	Durbin-Watson
	Median diameter (millimeters)	Drops/second/square meter	0.943	0.888	0.005	1.711
	Velocity of fall(meters/second					
	Drops/second/square meter					

Source: computed by author

Conclusion:

The Cloudburst is one of the major natural hazards in the Himalayas, occurring amid extreme hydro-meteorological conditions**.** It is difficult to forecast a mesoscale weather phenomenon like cloudburst. It requires high-resolution numerical models, Doppler Weather Rader (DWR), Automatic Weather Station (AWS), Radiosonde/Rawinsond (RS/RW). High intensity rainfall events in the Himalayan region are often localized which sometimes occur in remote areas because of topographic variations. Cloudburst sometimes even remains unreported due to inaccessibility of the region where they occur. However, the actual mechanism of cloudburst is still remain unknown to scientists. A possible cause of the copious rainfall could be the fusion of westerlies, which triggered Flash Floods. Recent climate change can be predicted as one of the major causes of Cloudburst.

References:

1. Deshpande, N. R.; Kothawale, D. R.; Kumar. V.; Kulkarni, J. R.; International Journal of Climatology. 2018, 1-17. https://doi:10.1002/joc.5560.

2. Jain, S. L.; Jain, A. K.; Sharad, K.; Science Reporter. 2013, 50(8), 12-18.

3. Dimri, A. P.; Chevuturi, A.; Niyogi, D.; Thayyen, R. J.; Ray, K.; Tripathi. S. N.; Pandey, A. K.; Mohanty, U. C.; Earth-Science Reviews. 2017. 168, 1–23.

4. IMD, Cloudburst over Leh (Jammu & Kashmir). 2010, http://www.imd.gov.in/doc/cloud-burst-over-leh (accessed 27 Sept 2012).

5. Mukherjee, S.; Geophysic sand Remote Sensing. 2013, 3, (3), 1-4.

6. Stages of Thunderstorm Development. http://www.geo-graphy.hunter.cuny.edu/~tbw/wc.notes/10.thunderstorms.tornadoes/thunderstorm_stages.htm/(accessed 22 Nov2015).

7. Dynamics & Microphysics of Cool-Season Orographic Storms Comet Met Ed. http://www.meted.ucar.edu/norlat/orographic/media/graphics/rad_time_2 (accessed 22 Nov 2015).

8. Das, P. K.; Journal of Environmental Science, Toxicology and Food Technology. 2013, 7(2), 33-45.

9. Hakhoo, S.; Frequent cloudbursts have state on edge, The Tribune. 2015, http://www.tribuneindia.com/news/jammu-kashmir/frequent-cloudbursts-have-state-on-edge/111633. html (accessed 26 Nov2015).

10. Lull, H. W.; Soil Compaction on Forest and Range Lands, U. S. Dept. of Agriculture, Forestry Service.1959, 768, http://ga.water.usgs.gov/edu/watercycleprecipitation.htm (accessed 2 Oct 2012).

CHAPTER

14

Biomedical application of graphene and graphene based nanocomposites

✎ *Dr. Mitali Dewan*

Department of Chemistry, Shahid Matangini Hazra Govt. General Degree College for Women, Kulberia, Purba Medinipur, West Bengal -721649, India.

E-mail: mitalichem@gmail.com

Introduction:

Graphite, diamond, fullerenes, nanotubes, nanowires, and nanoribbons are carbon-based materials that have been utilized in electronics, optics, optoelectronics, biomedical engineering, tissue engineering, medical implants, medical devices, and sensors. Graphene is a relatively young substance in the carbon family with several unique features. Graphene is a nanomaterial consisting of a single layered planer sheet made up of sp^2 – bonded carbon atoms arranged in a honeycomb crystal lattice. Chemically, mechanically, and thermally, graphene is a very stable material. Other characteristics include a big specific surface area and excellent elasticity.[1] This sort of arrangement in graphene with the strong carbon-carbon bonding in the plane, aromatic structure, presence of free π electrons and reactive sites for surface reactions make it a unique material with exceptional mechanical, physicochemical, thermal, electronic, optical and biomedical properties.[2] Many of its material properties, including as mechanical stiffness, strength, and elasticity, as well as extremely high electrical and thermal conductivity, are unique. Graphene is the strongest and stretchiest material known, with the highest thermal conductivity and inherent mobility, as well as being entirely impervious. Due to its extraordinary features, graphene oxide (GO), reduced grapheme oxide (rGO), graphene nanocrystals, graphene nanosheets, graphene nanotubes, graphene nanocubes, graphene quantum dots, and many others are also intensively explored. Graphene is stronger than many other metals and it is highly

flexible. Graphene stands out as the most potential contender for being a main filling agent for composite applications because to its remarkable thermal, mechanical, optical, and electrical capabilities. Many prominent properties of graphene allow inorganic nanoparticles to aggregate in it and create nanocomposites. For further advantageous properties, graphene nanoparticles are coated with other nanoparticles on their surface. To make nanocomposites, graphene is combined with a variety of different nanoparticles, including metals (Ag, Au, Cu, Zn), non-metals (chitosan, polymers, epoxy), and metal oxides (TiO2, ZnO).

Graphene nanocomposites (GNCs) at very low loading show substantial enhancements in their multifunctional aspects, compared to conventional composites and their materials. This not only makes the material lighter with simple processing, but also makes it stronger for various multifunctional applications.[3] The advantages of GNCs are: i) planar structure, ii) high surface area, iii) enhanced physical properties and iv) cost effectiveness. GNCs are mainly classified as (a) graphene-polymer nanocomposites and (b) graphene inorganic nanocomposites. Details classifications are shown below:
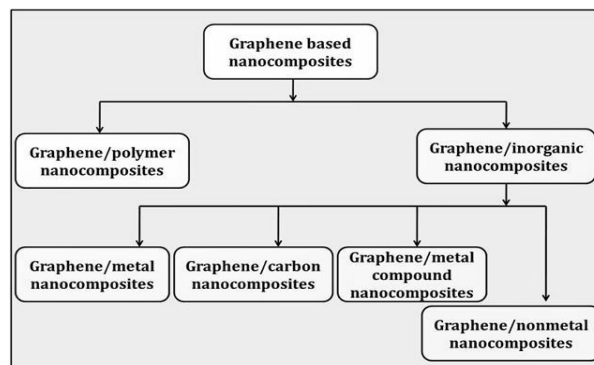
Figure-1: Classification of graphene based nanocomposites

Due to light weight, thin, flexibility, durability and all in one property enable the uses of graphene and graphene based nano materials in the various field of applications. The potential applications of graphene include microelectronics, display screens, electric or photonics circuits, energy

storage devices such as solar cells, fuel cells etc., catalyst, photocatalyst and various medical, biological, industrial processes.
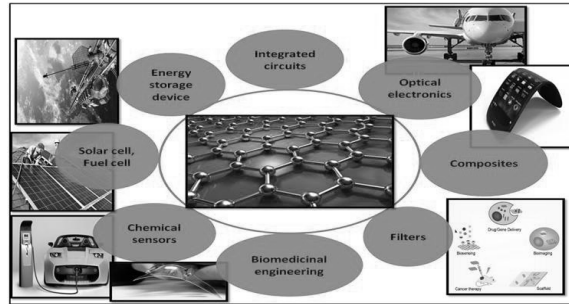
Figure-2: Applications of graphene in different fields

Biomedical applications of graphene:

Graphene has a variety of features that make it attractive for biomedical applications. Antimicrobial, anticancer, biosensing, bioimaging, and drug delivery are just a few of the applications for graphene nanocomposites. Graphene and its nanocomposites have recently received a lot of attention in biomedicine for drug/gene delivery, cancer treatment, tissue engineering, and biosensing.
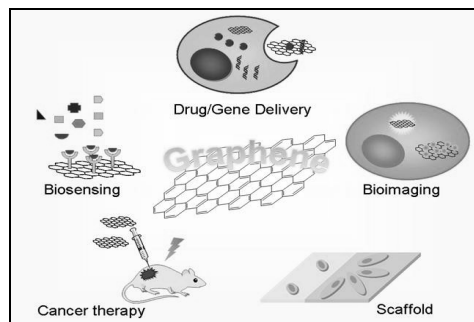
Figure-3: Biomedical application of graphene

Drug delivery

Large surface area, chemical purity and the possibility of easy functionalization render graphine an ideal candidate for drug delivery. In presence of external magnetic field graphene droplets change its structure. This phenomenon unlock the entrance for potential use of carrying drug in the graphene droplets and drug release upon reaching the targeted tissue when the droplets change shape at the magnetic field. Another applicable area might be the disease detection if graphene is found to change shape in presence of certain disease markers such as toxins. Graphene sheets act as potential drug carriers because both sides of graphene sheets are available for drug binding. Graphene oxide contains a large surface area, negative surface charge and enriched oxygen-containing groups which make it suitable for potential drug delivery systems. Graphene/graphene oxide can form complex with drug molecules at the surface through strong π-π stacking, which leads them to form stable complex avoiding chemical conjugation. Many functional groups (-COOH, -OH etc.) present on the surface of graphene oxide allow the positively charged drugs and polymers to interact and form complex.[4]
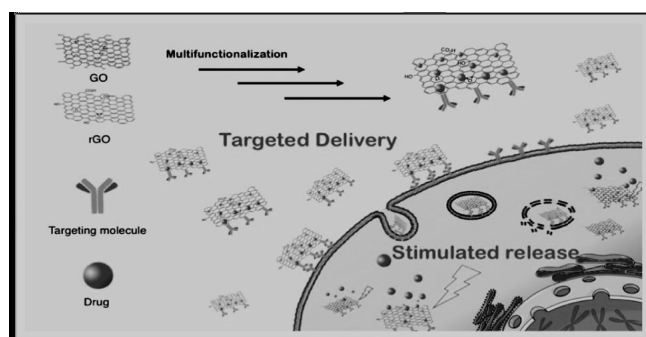
Figure-4: Applications of GO and RGO in drug delivery

Cancer therapy

 Based on their high absorption near-IR region (NIR), graphene and its derivatives have been used for several biomedical applications including anticancer therapy. Recently, it has been reported that the phototherapeutic effect of GO derivatives originates from the induction of the oxidative stress, mitochondrial depolarization and caspase activation that results in apoptotic

and necrotic cell death. Due to its large surface area and unique conjugated structure, the graphene oxide and reduced graphene oxide are used for the in vivo treatment of cancer.[5]
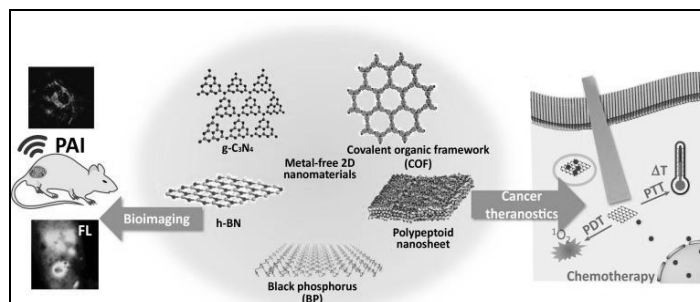
Figure-5: Graphene-like metal free 2D nanosheets for cancer imaging and theranostics[5]

Antibacterial potentiality

In recent times, graphene and graphene based nanomaterials have appeared as talented antibacterial materials. Chemically modified graphene such as graphene oxide (GO) and its reduced form could inhibit the growth of several clinically relevant pathogens which is mainly due to the favourable combination of physical structure and chemical functionality. Leading contact with such a nanostructure, membrane stress encouraged by the sharp edges of graphene nanosheets cause considerable physical damage to cell membrane and successive loss of bacterial membrane reliability and leakage of intracellular material. In comparison to other nano-materials, smaller size (<10nm) of rGO demonstrate higher antibacterial activity, due to the flattering combination of high surface area and mobility across cell membrane.[6]
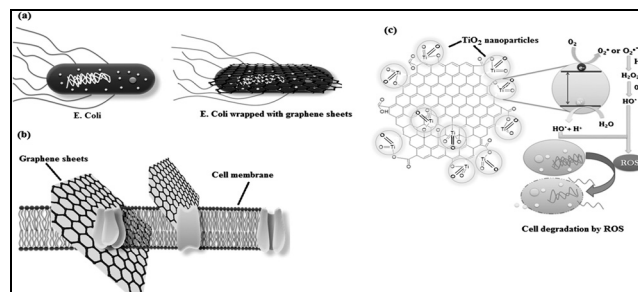
Figure-6: Photo inactivation of *E. coli* cell by metal oxide/graphene composite.[7]

Graphene in Gene Therapy

Gene therapy is a relatively recent strategy to treating diseases including cystic fibrosis, Parkinson's disease, and cancer that are caused by genetic defects. Following the European Commission's approval in 2012, Glybera became the first gene therapy medicine to be licenced for clinical use in either Europe or the United States. Gene therapy includes transferring therapeutic DNA into the patient's cells and using DNA as a medicine to cure illness. A gene vector that shields DNA from nuclease degradation and promotes cellular absorption of DNA with high transfection efficiency is important for successful gene therapy. In gene delivery, graphene functionalized with cationic polymers like polyethylenimine (PEI) has been used. Because of its strong electrostatic attractions with negatively charged phosphates of RNA and DNA, PEI has been intensively researched as a non-viral gene carrier. It also makes chemical modification simple, allowing for improved transfection efficiency, cell selectivity, and cytotoxicity reduction. Due to non-covalent interactions with the interface of PEG–GO, amino-terminated PEGylated GO has also been effectively employed to transport large Proteinpayloads   .
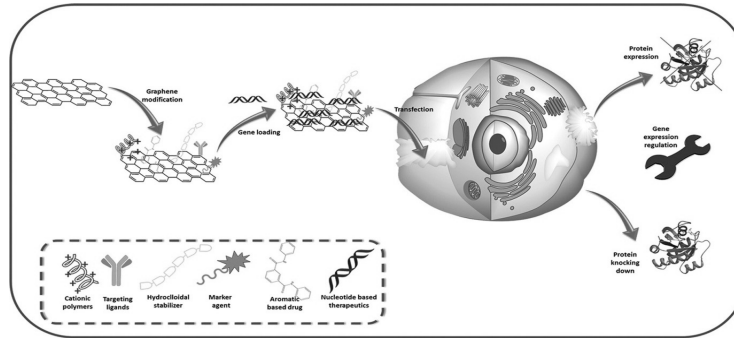
Figure-7: Graphene-based Nano-Carrier modifications for gene delivery applications[8]

Graphene in Biosensing

Biosensors may be used to detect or sense biomolecules, which is significant for health, environmental, and security purposes. A bio-molecule serves as the recognition element in biosensors. The transducer, which turns chemical information into a quantifiable signal, is a critical component of the sensing platform. Because of its conductivity shifting qualities as a function of the level of surface adsorption, large specific area, and low Johnson noise, graphene has recently emerged as a promising contender for biomolecule sensing. Single-stranded DNA nucleotide bases bind strongly to the graphene surface by - stacking, which is considerably weakened following DNA hybridization to create double-stranded helped creation of nanoprobes for DNA analysis. Wang et al.[9] reported effective transport of oligonucleotides (including aptamers) into living cells using a grapheme oxide nanosheet (GO-nS) for in situ bio-molecule probing. Graphene or graphene-based nano-composites have a large specific surface area and strong electron mobility, making them a viable material for modifying electrodes in eletrochemical sensing of diverse bio-molecules such as glucose, DNA, and proteins. Graphene's zero-band gap semiconductor feature makes it a suitable choice for field effect transistor (FET)-based biosensor manufacturing. The utilisation of carbon nanotube-graphene hybrid materials for biosensing is now the subject of current research.
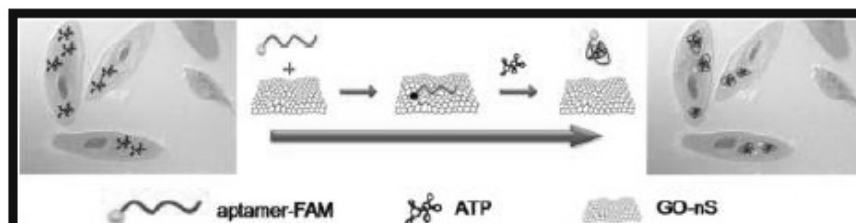
Figure-8: Schematic illustration of *in situ* molecular probing in living cells by using aptamer/GO-nS nanocomplex.[9]

Graphene in Regenerative Medicine:

Regenerative medicine involves the process of tissue engineering of previously irreparable tissues or organs. Cells, signaling molecules, and natural or artificial scaffolds are the three major aspects of tissue engineering systems. The tissue-reforming reaction is catalyzed by early interaction between regeneration cells or tissues and nanostructures. Recent research has shown that graphene-family nanomaterials, such as graphene, GO, and rGO, promote the adhesion and proliferation of mammalian cells such as human mesenchymal stem cells (hMSCs), human osteoblasts, fibroblasts, and adenocarcinoma cells. Hybrid nanoparticles of graphene sheets decorated with strontium metallic nanoparticles for bone tissue engineering has recently been reported [10]. Composites prepared using reduced graphene oxide (RGO_Sr) hybrid nanoparticles that elute strontium ions can be utilized to made multifunctional scaffolds having good mechanical and osteoinductive characteristics.
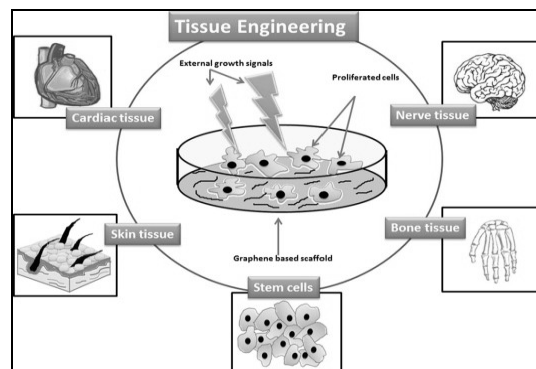
Figure-9: Application of Graphine based scaffold in tissue engineering

Conclusion:

In summary, the graphene nanoparticles and graphene-based nanocomposites are involved in many applications in the biomedical field. Graphene is highly effective because of its exceptional properties such as high specific surface area, good physiochemical property, mechanical and electrical stability. The graphene nanoparticles and graphene-based nanocomposite have been exploited like carbon nanotubes for small molecule drug delivery, gene delivery, cancer chemotherapy, phototherapy, biosensing and regenerative medicine.

Reference:

1. S. H Hsieh, W. J Chen, T. H Yeh, Appl. Surf. Sc., 2015, 358, 63–69.
2. J. H Chen, C. Jang, S. Xiao, M. Ishigami and M. S Fuhrer, Nature Nanotech. 2008, 3, 206-209.
3. K. I Winey and R. A Vaia, MRS Bulletin, 2007, 32, 314–319,
4. L. M. Zhang, J. G. Xia, Q. H. Zhao, L. W. Liu, Z. J. Zhang, Small, 2010, 6, 537-544
5. Y. Luo, Z. Li, C. Zhu, X. Cai, L. Qu, D. Du, Y. Lin, Trends Biotechnol. 2018, 36, (11), 1145-1156.
6. S. Eduok, C. Hendry, R. Ferguson, B. Martin, R. Villa, B. Jefferson, F. Coulon, FEMS, Microbiol. Ecol. 91 (2015).
7. R. K. Upadhyay, N. Soin, S. Sinha Roy, RSC Adv., 2014, 4, 3823.

8. R.Imani,F. Mohabatpour, F. Mostafavi, Carbon , 2018,140, 569-591.

9. Y Wang, Z. H Li, D.H Hu, C.T Lin, J.H Li, Y.H Lin. J. Am. Chem. Soc. 2010. 132: 9274– 9276.

10. S. Kumar, K. Chatterjee, Nanoscale, 2015, 7(5), 2023-33.

CHAPTER

15

Comparative Study of Various Biometric Techniques

✎ *Anindya Mondal*

Department of Computer Science, Chandrakona Vidyasagar Mahavidyalaya,
Paschim Medinipur, W. B.-721201, India

E-mail: anindya.cs@gmail.com

Introduction:

The word biometric came from two words - 'bio' and 'metric'. 'Bio' means something related to life and metric means measure. In different biometric techniques we consider some of characteristics or feature of life. A person can be identified based on measuring unique physiological and behavioral characteristics using some automated system. Some of these characteristics are iris, fingerprint, voice, signature, ear, face, DNA and few others. These characteristics are used in biometric techniques for identification because these are unique for every person.
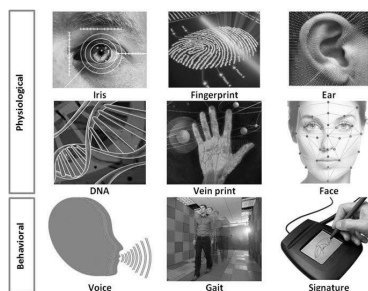
Figure-1: Different biometric Characteristics

Figure-2: Identification & Verification

Biometric techniques are applied for providing security in some real life situation by allowing only authorized person to access some resources. Authorization technique requires two important procedures- i) Identification

of a person ii) verification of a person. Finding a specific person among many people based on some matching is called identification. Validation of a claim by any person about his identity that he is claiming is called verification.So, Identification is N: 1 matching and verification is 1:1 matching.

Motivation and objective:

In the initial portion of this chapter, how biometric system works has been described in general. Later on, working principal of fingerprint biometric has been explained thoroughly. Today several biometric techniques like fingerprint, iris, face, voice etc. are commercially available in the marketplace and few more like gait[4] are under research. Among all such biometric systems which one should be used is solely depending on the requirement of the application area and cost of biometric system. In this regard several characteristics of biometric system have been considered and score of each biometric technique in all the characteristics enable us to choose proper biometric technique effectively according to a specific application.

How Biometric technique Works:

Before identification or verification we must enter the biometric data in the database of related /eligible person and this process is called enrolment. Biometric data are stored as template that contains features.
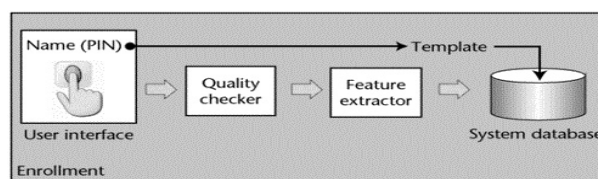
Figure-3: Enrolment procedure

Feature can be matrix of numbers generated from raw biometric data. It is a piece of information about the content of any raw biometric data, for example image of fingertip for fingerprint biometric technique. Typically fingerprint image contain certain unique pattern of things are known as feature. Features may be specific structures in the biometric image such as

points, edges or objects. Finger print image contain features like ridges and valleys, ridge ends some point or a ridge bifurcated into two ridges relative to the image and these feature is used to identify a person uniquely.
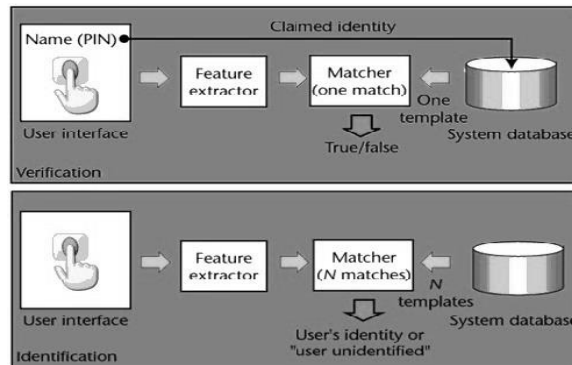
Figure-4: Verification procedure (Top) and Identification procedure (Bottom)

Feature extraction and matching phases are most vital among all phases in biometric identification. Three different fingerprint biometric feature extraction and matching techniqueare described in [5][6][7].

- ➢ Minutiae-based technique: Identification of minutiae points with their relative position on finger is performed. It requires less cost and computational time. It is capable of handling rotations in fingerprint image. As a result user need not require perfect orientation of his fingerprint.

- ➢ Correlation-based technique: The Correlation based technique uses pixel values of the two images during matching. It actually uses gray scale information of fingerprint image. The technique considers theuser's fingerprint template and the pixel values of the template are then correlated with the pixel values of all the images in the template database. It is less accurate than the minutiae-based technique although more efficient for low quality fingerprint images.

➢ Pattern based matching: It compares the basic fingerprint patterns between claimant and stored fingerprint templates. Gabor filter are applied toextract the feature vectors from binary image of fingerprint. The feature vectors generatefeature maps. And this feature map is matched with the feature map of fingerprint image stored in the database. Euclidean distance is generally used in such matching.

Discussion:

Fingerprint Biometric- An example

Some feature is present in finger print of every person that is unique. So fingerprint features can be used to identify or verify a person uniquely. Ridge endings and Ridge bifurcation with their position in some fingerprint is used as feature. These unique features are known as minutiae.
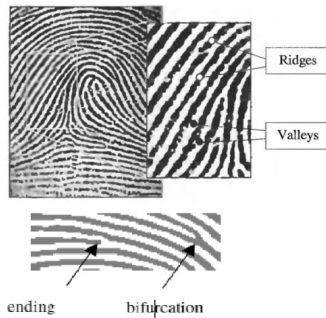
Figure-5: Ridge endings Scanner and Ridge bifurcation

Figure-6: Fingerprint

Fingerprint biometric technique includes the following procedure.

➢ Image acquisition procedure takes raw fingerprint image from fingertip of any person using some specific scanner.

➢ Image enhancement procedure is used to increase the clarity of the fingerprint image captured through image acquisition procedure. Various image sharpening filters like Gabor filter[1] is used for the

purpose. Sharpening procedure helps to find out feature more effectively.

➢ Feature extraction procedure finds out the location of ridge ending & bifurcation in the finger print and makes a template.

Figure-7: Result of image sharpening   **Figure-8:** located ridge endings & bifurcations

➢ Storing template procedure is used to store new template during the enrolment and also during the time of verification.

➢ Matching processes finds the similarity between input template and previously stored template in the database. After matching it gives matching score. Different matching algorithms like Minutiae based fingerprint matching algorithm[2] or adaptive filter method[3] using Gabor filter are extensively used. Some advanced technique has been documented in Jain et al.[10]
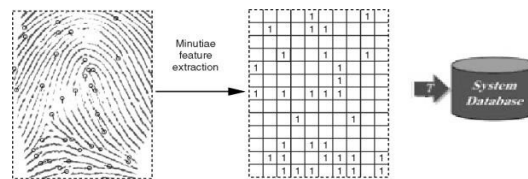
Figure-9: Storing template into the database

➢ Decision making procedure compare match score with a threshold value. If the match score is equal to or greater than the threshold value then accept the claim otherwise reject.

Application of Gabor filter:
The ridge structure in a fingerprint image can be considered as an oriented texture patterns having an orientation in a local neighbourhood and prominent spatial frequency. The orientation is the result of flow pattern exists in ridges and frequency caused by inter ridge-spacing. A unique representation of fingerprint can be possible by knowing the orientation and frequency of ridges in local region of fingerprint image.

At first a core point is defined at the north most point of inner-most ridgeline. In some cases practices, the core point placed at the centre ofnorth most loop type singularity. A circular region around the core point is considered and tessellated into several sectors. Theintensies of pixelin each sector are normalized to a constant variance and mean. A set of sixteen Gabor filters are applied on the circular region and produce a set of sixteenfiltered images. Using the set of Gabor filteris a very popular technique to capture useful information in specific band pass channel. One such application of Gabor filter mentioned in [8].

The absolute average deviation for asector produces quantity that actually represents the ridge structure and is usedas a feature. Accumulating all such feature computed from each of the sector of all filtered image forms the feature vector. During matching, Euclidean distance betweenthe two corresponding feature vectors is computed.

Gabor filter is an example of adaptive filter whose behaviour changes based onstatistical characteristics of the image inside the filter region.

$$G(x, y ; f, \theta) = \exp\left\{\frac{-1}{2}\left[\frac{x'^2}{\delta_{x'}^2} + \frac{y'^2}{\delta_{y'}^2}\right]\right\}\cos(2\pi f x') \quad (1)$$

$$x' = x \sin\theta + y \cos\theta \quad (2)$$

$$y' = x \cos\theta - y \sin\theta \quad (3)$$

Where f is the frequency of the sinusoidal plane wave along the direction θ from the x-axis, and δ_x and δ_y are the space constants of the Gaussian envelope along x and y axes, respectively.

The frequency f is the average ridgefrequency (1/K), where K is the average inter ridge distance. The average inter ridge distance is depend on spatial resolution of fingerprint image.

Selecting threshold value:

Reference threshold or simply threshold value is a value that can decide the authenticity of a person. Authenticity means whether the person is genuine or intruder. As the measurement of biometric features is statistical in nature, statistical calculation of various parameters like reference threshold, FAR (False AcceptanceRate), FRR (False Rejection Rate) are essential for biometric system.
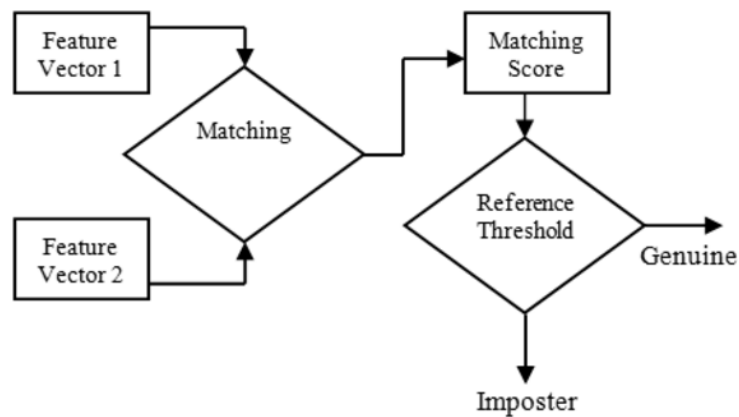
Figure 9: Matching of two feature vectors

FAR is the rate at which a non-authorized person is identified as genuine. On the other hand FRR is the rate of a genuine person getting rejected by some biometric system.

$$FAR = \frac{Wrongly\ accepted\ individuals}{Total\ number\ of\ wrong\ matching}$$

$$FRR = \frac{Wrongly\ rejected\ individuals}{Total\ number\ of\ correct\ matching}$$

Selecting improper value of reference threshold can lead to two kinds of possible errors:

➤ False matches (false acceptance)

➤ False non-matches (false rejection)

Choosing reference threshold is a trial and error method aiming maximum accuracy. In practice reference threshold can be selected efficiently based on accuracy of the system given by

$$Accuracy(\%) = \left(100 - \left(FAR(\%) + FRR(\%)\right)/2\right)$$

This equation may vary depending on requirement of specific application. One of the popular works on selecting reference threshold has been described in Malik et al.[11]

Characteristics of Biometrics:
Evaluation of different biometric techniques can be done by using some characteristics discussed below. There are numerous pros and cons of different biometric techniques that must be considered.

➤ Universality characteristic ensures that the biometric technique is applicable to every person. For example fingerprint biometric technique is applicable to every person.

➤ Uniqueness is a characteristic of biometric technique that cares about the feature present in biometric must be different for any two people; fingerprint of any two persons are different.

➤ Permanence is other important characteristics that confirm that feature of any biometric data should not change with time for a specific person; fingerprint generally does not change with time.
➤ Collectability characteristic concern about how much easy is the data acquisition process for a biometric technique; Collectability of DNA is low.

➢ Performance is measured mainly based on accuracy rate and speed in recognition.

➢ Acceptability is measures how much acceptable for any person who like to give his biometric data in acquisition process. So, large population must like to accept the biometric technique. For example DNA biometric has low acceptability.

➢ Circumvention of any biometric data is measured high if the data can be easily imitated. Low circumvention is considered to be good.

Comparison of Various Biometric Techniques
Here we compare different biometric techniques based on the score for every characteristics mentioned above. Score is given in three values, High, Medium and Low.

Table-1: Comparing different biometric techniques based on characteristics.

Biometric Techniques / Characteristics	Finger	Face	Iris	Hand	Retina	DNA	Signature
Universality	High	High	High	Mid	High	High	Low
Uniqueness	High	Low	High	Mid	High	High	Low
Permanence	High	Mid	High	Mid	Mid	High	High
Collectability	Mid	High	Mid	High	Low	Low	High
Performance	High	Low	High	Mid	High	High	Low
Acceptability	High	High	Low	Mid	Low	Low	High
Circumvention	Mid	High	Low	Mid	Low	Low	High

Conclusion:

Today Biometric is a rapidly growing technology and it has numerous application areas like forensics to identify criminals, security of different public places, for preventing unauthorised access to ATMs, smart phones, desktop computers and computer networks.. Today we see that the fingerprint biometric become the most used technique among all the popular biometric techniques due to its overall good efficiency in all the characteristics. It is also true that no biometric system is absolute efficient for all the characteristics. To cover all the characteristics with absolute efficiencywe must combine two or more biometric techniques known as multimodal biometric. For instance iris & finger print both are used in combination for a multimodal biometric technique.

References:

1. H. H. Ahmed, "Fingerprint Image Enhancement based on Threshold Fast Discrete Curvelet Transform (FDCT) and Gabor Filters," vol. 110, no. 3, 2015.
2. Vaishali Pawar, Mukesh Zaveri; 10th International Conference on Natural Computation , IEEE 2014.
3. Munir, M. U., Javed, M. Y., "Fingerprint Matching using Gabor Filters," 2005.
4. Imed Bouchrika "A Survey of Using Biometrics for Smart Visual Surveillance: Gait Recognition", 2018.
5. Cappelli, R., Maio, D., Maltoni, D., Wayman, J.L., Jain, A.K., 2006. Performance evaluation of fingerprint verification systems. IEEE Trans. Pattern Anal.Machine Intell. 28, 3–18.
6. D.Maltoni, D.Maio, A.K.Jain and S.Prabhakar, "Handbook of fingerprint recognition", Springer, New York, 2003.
7. Jain, A., Hong, L., Bolle, R., 1997. On-line fingerprint verification. IEEE Transactions on Pattern Analysis and Machine Intelligence 19, 302–314.
8. Munir, U., Javed, M., 2004. Fingerprint Matching using Gabor Filters. National Conference on Emerging Technologies.
9. Abdulrahman, S., Alhayani, B., 2021. A comprehensive survey on the biometric systems based on physiological and behavioural characteristics.
10. Jain, A.K., Prabhakar, S., Hong, L., 1999. A multichannel approach to fingerprint classification. IEEE Transactions on Pattern Analysis and Machine Intelligence 21, 348–359.
11. Malik, J., Girdhar, D., Dahiya, R., Sainarayanan, G., 2014. Reference Threshold Calculation for Biometric Authentication.International Journal of Image, Graphics andSignal Processing 6, 46–53.

CHAPTER

16

A rules based Modified Grey Wolf Optimization algorithm for the Traveling Salesman Problem

✆ *Indadul Khan*

Department of Computer Science, Chandrakona Vidyasagar Mahavidyalaya, Paschim Medinipur, W. B.-721201, India

E-mail: indadulkhan@gmail.com

Introduction:

The Traveling Salesman Problem (TSP) is one of the standard combinatorial discrete optimization problems. It is a well-known NP-hard problem, can't be solved exactly using any polynomial time algorithm. The problem consists of a set of N vertices (nodes/ cities) where the distance (travelling cost/travelling time, etc.) between any two vertices is known. A salesman starts from a vertex, visits all the vertices exactly once, and returns to the starting vertex in such a way that the total distance travelled is a minimum. So, the goal of the problem is to find the shortest possible tour through the set of vertices in such a manner that every vertex is visited exactly once except for the starting vertex. In the study, a modified grey wolf optimization algorithm is proposed for solving TSP. Five different solution update rulesare proposed to update quality of the solution. Proposed method is tested with a set of benchmark test problems from TSPLIB and it is observed that the efficiency of the algorithm is adequate with respect to the accuracy and the consistency for solving standard TSPs.

1. The classical TSP:

A TSP can be represented by a complete weighted graph $G = (V,E,W)$, where $V = \{1, 2, ...N\}$ is the set of vertices (nodes), $E = \{e_{ij}: i, j \in V \text{ and } i \neq j\}$ is the set of edges, and $W = \{d_{ij}: i, j \in V \text{ and } i \neq j\}$ is the weight matrix. Here, each node represents a city and each edge, e_{ij}, represents the path between the associated cities, i.e., the path between the city i and the city j, and the weight d_{ij} associated with the edge e_{ij} represents the distance between the end

vertices (cities) of the edge, i.e., the distance between the city i and the city j. A salesman starts from a city and likes to travel all the cities exactly once and returned to the starting city covering the least distance (using least cost/time). Goal of the problem is to find out the optimum path for the salesman. Let d_{jk} be the distance between j-th city and k-th city. So, the problem can be mathematically formulated.[1]

$$\left.\begin{aligned} \text{Determine } & x_{jk}, \forall j, k \in V \& j \neq k \text{ to} \\ \text{Minimize } & Z = \sum_{j=1}^{N} \sum_{k=1}^{N} x_{jk} d_{jk} \\ \text{subject to } & \sum_{j=1}^{N} x_{jk} = 1, \ \forall k \in V \\ & \sum_{k=1}^{N} x_{jk} = 1, \ \forall j \in V \end{aligned}\right\} \quad (1)$$

where $x_{jk} = 1$ if the salesman travels from city-j to city-k, otherwise $x_{jk} = 0$.

Let $(x_1, x_2 \ldots, x_N, x_1)$ be a complete tour of a salesman, where $x_j \in V, \forall j \in V$ and all x_j's are distinct, i.e., $(x_1, x_2 \ldots, x_N, x_1)$ is the sequence of cities in which the salesman travels the cities. Then the above problem reduces to [38],

$$\left.\begin{aligned} \text{Determine a complete tour } & (x_1, x_2, \ldots \ldots \ldots x_N, x_1) \\ \text{to minimize } Z = & \sum_{j=1}^{N-1} d_{x_j x_{j+1}} + d_{x_N x_1} \end{aligned}\right\} \quad (2)$$

2. Graphical representation of TSP:

Consider a graph with four nodes A, B, C, D, and each node is associated with a cost. The cost between A, B is 20 and A, C is 42, respectively. A salesman starts the journey from the node (A) and returns to the starting node (A), there are 6 combination paths that will be constructed. The combinations are given below with the cost.
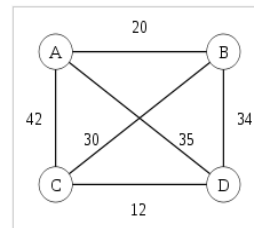
Path-1: A-B-D-C-A   Cost: 20+34+12+42 =108
Path-2: A-B-C-D-A   Cost: 20+30+12+35 =97
Path-3: A-C-B-D-A   Cost: 42+30+34+35 =141
Path-4: A-C-D-B-A   Cost: 42+12+34+20 =108
Path-5: A-D-B-C-A   Cost: 35+34+30+42 =141
Path-6: A-D-C-B-A   Cost: 35+12+30+20 =97

The goal of the problem is to find the minimum cost path. Among these combinations, path-2 and path-6 is considered due to the minimum cost of path length. Here, select any one path randomly because both paths have the same cost.

3. Variant of TSPs:

The classical TSP has been modified by the several researchers during the past few decades to make it applicable efficiently to deal with a wide range of real-world problems and hence various types of TSPs are available in the literature. These includes- Symmetric TSP (STSP), Asymmetric TSP (ASTSP), Multiple TSP (MTSP), TSP with time windows (TSPTW), Solid TSP (SOTSP), Profit maximization TSP, etc. The basic definitions of some of the variants of the TSPs are presented below.

Symmetric TSP: In the classical TSP (discussed in section 2), when $d_{ij} = d_{ji}$, i.e., the travelling distance from the city-i to the city-j is equal to the travelling distance between the city-j and the city-i then the problem is called a STSP, as in this case the distance matrix involved in the problem is symmetric.

Asymmetric TSP: In the classical TSP (discussed in section 2), when $d_{ij} \neq d_{ji}$, i.e., the travelling distance from the city-i to the city-j is not equal to the travelling distance between the city-j and the city-i for at least one pair of cities (i, j) then the problem is called an ASTSP, as in this case the distance matrix involved in the problem is not symmetric.

Multiple TSP: In a MTSP, more than one salesmen are involved in visiting the cities and one city is considered as the depot. Except the depot, a city is visited by only one salesman. Goal of the problem is to find out the tour schedule of each of the salesmen so that the total distance travelled by the salesmen is a minimum.

Solid TSP: A SOTSP is a variant of the basic TSP in which there are more than one available transportation mode for the travelling between any two cities. Cost/distance of travel between any two cities using different types of transport is different. So the cost matrix involved in the problem is three

dimensional. Due to this reason the problem is named as solid TSP. The salesman can choice different types of vehicle to travel between different pair of cities, so that the total tour cost of the Hamiltonian circuit is a minimum.

TSP with time windows: TSPTW is a special type of the TSPs, where, the salesman has to find a minimum cost Hamiltonian circuit though the cities, where, each city should be visited in a fixed time frame specified for the city.

Profit maximization TSP: Profit maximization TSP is a special type of the TSPs, where, the salesman spend some time at each city to sell his product. Profit at a point increases with the stay time. The goal of the salesman is to determine the Hamiltonian circuit through the cities as well as the stay time at each city under a specified time constraint.

4. Some application areas of the TSP

The TSPs have been effectively utilized to solve real-world challenges in different domains, such as mathematics, computer science, operations research, genetics, engineering, electronics, etc. Some application areas of the TSPs in the different domains are listed below.

The TSPs are used to solve problems relating to the transportation, the networkrouting, and the logistics etc.

The TSPs are applied in the fields of electronic manufacturing, component placement problems, robotic arm tour problems, etc.

The TSPs are used to solve the Machine Scheduling Problems, the Cellular Manufacturing Problems, the Warehouse Order-picking Problems etc.

Another application area of the TSPs is the Printed Circuit Board Problem (PCB) in the field of electronic engineering.

The Vehicle Routing Problem (VRP) is another real-life application area of the TSPs.

The School Bus Routing Problem is a well-known application area of the TSPs.

The Mission Planning Problem is another famous application area of the TSPs.

5. Time complexity of any exhaustive search algorithm of the TSP:

The TSP is a well-known NP-hard combinatorial optimization problem. A TSP having N cities can be represented by a graph with N nodes. A salesman starts from a city, visits all the cities exactly once, and returns to the starting city covering the minimum distance. Let us consider a TSP having N cities. Then there are N! permutations of the distinct cities and since there is a path between every pair of cities, there are N! Hamiltonian circuits through the cities. So the salesman has to select the minimum cost path among these N! options. Hence, the worst case time complexity of any classical algorithm of a TSP involving N cities is O(N!).

6. Solution Approaches with Literature Reviews:

The TSP is a well-known NP-hard combinatorial optimization problem and hence can't be solved using any polynomial-time algorithm.[2] The researchers have been developed various algorithms for the TSPs and its variants during the past few decades. The Irish and British mathematician W.R. Hamilton and T. P. Kirkman were the first proposer of the mathematical formulation of the TSP in 1800s. The general form of the TSP including the problem definition was initially proposed by K. Menger in Vienna at Harvard University in 1900s.[3] The concept of the TSP as a combinatorial optimization problem was began with the work of Dantzig, Fulkerson, and Johnson[1] in 1954.

Generally, there are two approaches to solve a TSP: the exact methods (classical approaches) and the heuristic methods. An exact method requires very large amount of time for any moderate size problem and hence the heuristic methods are typically used to solve the TSPs. The exact methods include cutting plane, LP relaxation, branch and bound, branch and cut, etc. Only very small-size TSPs can be solved by the exact methods in a reasonable time window. On the other hand, several TSPs have been solved using heuristics or metaheuristicbased techniques such as Ant Colony Optimization (ACO), local search, hybrid algorithm, Genetic Algorithm (GA), Particle Swarm Optimization (PSO), Artificial Bee Colony (ABC), etc.

There are several well-established heuristics/ metaheuristics, hybridization of the different heuristics for the TSPs, available in the literature. Tsai et al. presented a metaheuristicapproach called ACOMAC algorithm for solving the TSPs in 2004. Wang et al.[4] used the concepts of the swap operation (SO) and the swap sequence (SS), and redefined some operators of the PSO on the basis of them to solve the classical TSPs in 2007 and etc.

Raising some limitations of the above studies on the development of the heuristics for the TSPs, Khan et al.[5] presented a hybrid algorithm based on ACO-PSO-K-Opt for solving the symmetric well as the Asymmetric TSPs in an effective manner in 2017. Khan et al.[6] presenteda modified PSO algorithm using multiple velocity updating rules for solving the TSPswith the precise and imprecise cost matrices in 2018. Khan et al.[7] also proposed a SS based ABC algorithm by introducing the multiple solution updating rules for the TSPs in 2019. Khan et al.[8] proposed another hybrid algorithm, PSO-GA, for the TSPs in different environments in 2019.

Recently, in 2021, combining the features of Rider Optimization and Spotted Hyena Optimization Algorithm, Krishna et al.[9] proposed a hybrid algorithm for the TSPs; Gunduz et al.[10] proposed a discrete Jaya algorithm for solving the TSPs; and Panwar et al.[11] have presented a heuristic, named, Discrete Grey Wolf Optimizer (DGWO) for the STSPs.

7. Benchmark instances of the TSP:

There is a library of benchmark test problems on the TSPs in the literature, named TSP library (TSPLIB).[12] This library of test problems is maintained at the University of Heidelberg by Professor Gerhard Reinelt.[13] This library consists of the data sets of the different size classical TSPs as well as the respective optimal tour costs along with the corresponding Hamiltonian circuits. Normally, the performance of any newly designed algorithm for the TSPs is tested using different size instances from this library.

8. The Grey Wolf Optimization algorithm for TSP:

Mimicking the hunting and social behaviour of a grey wolf pack, the GWO heuristic was initiatedby Mirjalili et al.[14] in 2014 for the single objective continuous optimization problems. In a pack of grey wolves, four types of

wolves are found: Alpha (α), Beta (β), Delta (δ) and Omega (ω) type. These wolves have maintained the behaviour of a social hierarchy of leadership. According to this hierarchical structure, the α wolf belongs to the top position of the structure, then successively β, δ and ω wolves take their position. This classification is made by the strength/fitness of the wolves. Here, α, β and δ wolves are leaders and ω wolves are followers.[14]

8.1 Modification of the Grey Wolf Optimization algorithm for the TSP:

Mirjalili et al.[14] proposed GWO algorithm for the single objective continuous optimization problems but here, a modified GWO algorithm is proposed for solving well-know TSP. Multiple solution update rules are introduced to solve the TSP. These rules are made using concept of swap operation SO and swap sequence (SS).[7] The details description of the SS and SO, please see ref-7.

8.1.1. Initialization:- Initially, N number of solution are generated randomly. Each solution is assigned to each wolf in the population. Determine the fitness of each solution. The min-cost solutionis assigned to the Alpha (α) wolf, then second min-cost solution is assigned to the Beta (β) wolf and third min-cost solution is assigned to the Delta (δ) wolf and remaining wolves are consider as Omega (ω) wolf.

8.1.2. Solution update approach:- Here, it is assumed that the wolf pack contains N wolves. Five different rules are proposed here toupdate the positions of the wolves. In the rules, α, β, δ represents the positions of Alpha, Beta and Deltawolves. $x_i$is the position of the i-th wolf in the pack and x_r represents the position of randomly selected wolf from the wolf pack.

$D_i = ((c_1 \odot (\alpha \ominus x_i) \oplus (c_2 \odot (\beta \ominus x_i) \oplus (c_3 \odot (\delta \ominus x_i)).$ (3)

$D_i = ((c_1 \odot (\alpha \ominus x_r) \oplus (c_2 \odot (\beta \ominus x_i) \oplus (c_3 \odot (x_r \ominus \delta)).$ (4)

$D_i = ((c_1 \odot (\alpha \ominus x_i) \oplus (c_2 \odot (\beta \ominus x_r) \oplus (c_3 \odot (\delta \ominus x_i)).$ (5)

$D_i = ((c_1 \odot (\alpha \ominus x_i) \oplus (c_2 \odot (\beta \ominus x_r) \oplus (c_3 \odot (\delta \ominus x_r)).$ (6)

$D_i = ((c_1 \odot (\alpha \ominus x_r) \oplus (c_2 \odot (\beta \ominus x_r) \oplus (c_3 \odot (\delta \ominus x_i)).$ (7)

$x_{new} = x_i \Delta D_i.$ (8)

where x_{new} is the new solution determined by applying equation (8) and one perturbation amount, D_i, which is selected according to the fitness of the

rules using Roulette-Wheel (RW) selection technique. Here, c_1, c_2 and c_3 are uniformly distributed over [0,1]. Here, $c_1 \odot (\alpha \ominus x_i)$ means all swap operators in swap sequence $(\alpha \ominus x_i)$ should be maintained with the probability c_1. The symbol Δ represents swap operation.

8.1.3. Rule selection technique: In every cycle of the algorithm rule selection mechanism is required. In this study, each rule is associated with a counter (named

success-counter) having initial value 1. The probability of selecting i-th rule, ρ_i, is measured by the following equation 9.

$$\rho_i = \frac{c_i}{\sum_{j=1}^{n_{eq}} c_i}, \quad i = 1, 2, \dots n_{eq} \tag{9}$$

Where ρ_i is
the probability of selection of the i-th rule. The n_{eq} is the number of rules in the rule set. Here, n_{eq} is 5. The c_i is the success-counter value corresponding to the i-th rule. Here, RW-Selection technique is used for selecting a rule. By applying the selected rule, any ω wolf tries to update the quality of its position and if improvement is found then the success-counter value of the rule is increased by one and this process is continued throughout the algorithm.

8.1.4. Proposed Modified Grew wolf Optimization algorithm for TSP
Step-1: Initialization:
    a.   Randomly generate N number solution.
    b.   Determine the fitness of each solution.
    c.   Select α, β, δ wolf from wolf pack.

Step-2: Solution update:
    a.   **For** each wolf x_i in population (N)
Determine a new solution (x_{new}) of x_i wolf using equation (8).
If $(x_{new} < x_i)$

$x_i = x_{new.}$

End IF.

End For

  b.   Select new **α, β, δ** wolf from current solution set.
Step-3: Terminating condition:
     If (Terminating condition not meet)
Go to Step-2.
Step-4: Final result:
          Return the best solution (α).

9. Experimental Result: The performance of the proposed algorithm is tested using differentsize standard TSPs from TSPLIB. From each problem algorithm is testedby running the program 10 times for different seeds of random numbergenerator and the best solution obtained, the average value of thesolutions, standard deviation (SD) value of the solutions and percentage of relative error (Error (%)) according to the optimal solution arecalculated. The percentage of relative **Error** (%) is calculated using the following equation 10.

$$\mathbf{Error}(\%) = \frac{average\ solution - optimal\ solution}{optimal\ solution} \times 100 \qquad (10)$$

Table-1 represents the results of the proposed algorithm of different sizes of TSP instances. The Best cost column represents the best cost obtained by the proposed algorithm. The Optimal cost column represents the optimal value corresponding to the TSP instance from TSPLIB. The statistical information of test problems are used to measure the performance of proposed algorithm. Here, four different types of statistical information is used. It is observed that from table-1, Each problem has been obtained optimal result except eil 51 instance. It is conclude that from the observation the performance of the proposed algorithm is better.

Table-1: The Result obtained by the proposed algorithm for some STSP from TSPLIB

	Problem from TSPLIB	Optimal cost of the problem	**Best cost obtained**	Worst cost obtained	Statistical information of test problems			
					Mean cost of the solutions	Median value of the solution	Standard deviation (SD) of the solutions	Percentage of Error (Error(%))
	gr17	2085	**2085**	2085	2085.00	2085	0.00	0.00
	bays29	2020	**2020**	2020	2020.00	2020	0.00	0.00
	swiss42	1273	**1273**	1273	21273.00	1273	0.00	0.00
S	eil51	426	427	428	427.01	427	0.46	0.07
	berlin52	7542	**7542**	7542	7542.00	7542	0.00	0.00
T	st70	675	**675**	678	675.77	675	1.17	0.18
	eil76	538	**538**	540	538.15	538	0.60	0.02
S	rat99	1211	**1211**	1213	1211.50	1211	0.67	0.041
	kroA100	21282	**21282**	21305	21287.19	21284	8.10	0.02
P	eil101	629	**629**	635	630.59	629	2.37	0.25

Conclusion:

TSP is one of the standard combinatorial discrete optimization problems. It is a well-known NP-hard problem, can't be solved exactly using any polynomial time algorithm. Since the 1800s, several researchers have been proposed various approaches for solving TSP in reasonable time windows. It has various application areas in the different fields of science and technology. Due to this reason, researchers are focused their study on the new application areas of TSP. In the study, a modified grey wolf optimization algorithm is proposed for solving TSP. Five different solution update rules are proposed to update quality of the solution. Proposed method is tested with a set of benchmark test problems from TSPLIB and it is observed that the efficiency of the algorithm is adequate with respect to the accuracy and the consistency for solving standard TSPs.

Reference:

1. Dantzig, G.; Fulkerson, R.; Johnson, S.; Journal of the operations research society of America, 1954, 2, 393.
2. Lawler, E. L.; Wiley-Interscience Series in Discrete Mathematics, 1985.
3. Menger, K.; Das boten problem. Ergebnisseeines mathematics henkolloquiums, 1932, 2, 11.

4. Shi, X. H.; Liang, Y. C.; Lee, H. P.; Lu, C.; Wang, Q.; Information processing letters, 2007, 103, 169.
5. Khan, I.; Maiti, M. K.; Maiti, M.; In International conference on mathematics and computing, Springer, 2017, pages 103–119.
6. Khan, I.; Pal, S.; Maiti, M. K.; In 2018 4th International Conference on Recent Advances in Information Technology (RAIT), 2018, pages 1–8.
7. Khan, I.; Maiti, M. K.; Swarm and evolutionary computation, 2019, 44, 428.
8. Khan, I.; Pal, S.; Maiti, M. K.; International Journal of Uncertainty, Fuzziness and Knowledge-Based Systems, 2019, 27, 693.
9. Krishna, M. M.; Panda, N.; and Majhi, S. K.; Expert Systems with Applications, 2021, page 115353.
10. Gunduz, M.; Aslan, M.; Applied Soft Computing, 2021, 105, 107275.
11. Panwar, K.; Deep, K.; Applied Soft Computing, 2021, 105, 107298.
12. Reinelt. Tsplib http://comopt.ifi.uniheidelberg.de/software/ tsplib95/.
13. Reinelt, G.; ORSA journal on computing, 1991, 3, 376.
14. Mirjalili, S.; Mirjalili, S. M.; Lewis A; Grey wolf optimizer. Advances in engineering software, 2014, 69, 46.

NOTES